Understanding the Sources and Transformations of Ice Nucleating Particles and Trace Reactive Gases in Biomass-Burning Emissions

Submitted in partial fulfillment of the requirements for the degree of

Doctor of Philosophy in Chemistry

Lydia G. Jahl

Carnegie Mellon University

Pittsburgh, PA

September 2020

Acknowledgments

One of the main reasons I chose to attend CMU for my graduate studies was to be a member of the Center for Atmospheric Particle Studies (CAPS). I have enjoyed taking classes with, conversing with, and receiving feedback from all the PIs – Peter Adams, Neil Donahue, Coty Jen, Spyros Pandis, Albert Presto, Allen Robinson, and Ryan Sullivan. I have enjoyed learning from, talking to, conducting experiments with, and teaching all past and present CAPS students, especially Wayne, Penglin, Ellis, Antonis, Elina, Ningxin, Bob, Georges, Rishabh, Kerrigan, Katia, Naser, Dana, Spiro, Mingyi, Sandra, Brandon, and Luke.

Within CAPS, I am of course partial to the Sullivan research group. I have enjoyed working with each and every one of the past and present group members, and I applaud Ryan for his ability to cultivate such a collaborative and close group dynamic. Thanks to Adam Ahern for teaching me about the AMS and chamber experiments and for being so welcoming. Thanks to Hassan Beydoun for the intellectual and fun conversations about any topic. Thanks to Kyle Gorkowski for being the boss of the start-up office and for answering all my questions about the aerosol optical tweezers, even though none of my efforts there made it into my final dissertation. Thanks to Michael Polen for passing down his knowledge of ice nucleation and biomass burning; I had a great time road-tripping to North Carolina with him to collect grasses despite getting attacked by bugs, sharp leaves, and mud! Thanks to Qing Ye for teaching me about the AMS and for being a strong role model as a female scientist. Thanks to Hallie Boyer for teaching me about the AOT and how to navigate grad school. Thanks to Leif Jahn for participating in many collaborative experiments with me and for sharing our initials and New Jersey. Thanks to Tom Brubaker for sharing all our PhD time and for all of the ice nucleation analysis crucial to much of my work. Thanks to Bailey Bowers for helping to keep me sane and always being willing to help with anything! Thanks to Luke Monroe for making our field campaign bearable and pulling us out of the mud, literally. Thanks to Riley Weatherholt and William Fahy for being such motivated and

Abstract

The ability of a very small fraction of particulate matter to act as ice nucleating particles and initiate cloud glaciation has important impacts on cloud microphysics, precipitation, radiative forcing, and climate change. In recent years, the Sullivan group has investigated biomass-burning aerosol as a source of ice nucleating particles. My contributions towards measuring the aerosol chemical composition using aerosol mass spectrometry throughout biomass-burning experiments has improved our understanding of how atmospheric chemical aging influences the ice-nucleation activity of biomass-burning aerosol. We discovered that as biomass-burning aerosol ages, organic matter on the particle surfaces can evaporate or dissolve to reveal preexisting mineral-based ice-active sites, increasing the overall ability of biomass-burning aerosol to nucleate ice as it is undergoes transport and aging throughout the atmosphere. Some aging mechanisms, such as ozonolysis, result in the production of secondary organic aerosol which can have the opposite effect and result in no change or even a decrease in the ice-nucleation activity. While previous literature exists regarding how the ice activity of some types of ice nucleating particles change with atmospheric aging, no other work has investigated biomass-burning aerosol to the extent that my research has. My work introduces a new framework for the evolution of ice nucleating particles from biomass burning where the aerosol becomes more ice active as the smoke plume dilutes with transport. This results in a larger contribution to the ice nucleating particle budget, the resulting cloud microphysics, and climate forcing induced by wildfires than is currently considered.

My second main project was studying the unexplored multi-phase chlorine chemistry that we hypothesized occurs within biomass-burning smoke. In previous work by the Sullivan group, we were the first to identify the production of two important molecules in biomass-burning plumes: N_2O_5, a nocturnal reservoir for NO_x; and $ClNO_2$, which has important impacts on NO_x cycling, ozone formation, and atmospheric radical budgets. I then lead aerosol flow tube kinetics

experiments to determine the reactive uptake probability of N_2O_5 on biomass-burning aerosol as well as the product yield of $ClNO_2$. These two parameters have previously been determined on ambient aerosol and simplified aerosol proxies, but my collaborative experiments with researchers from the University of Washington were the first to determine these kinetic parameters on authentic biomass-burning aerosol. We discovered that among the aerosol generated from four different biomass fuels, the reactive uptake coefficients of N_2O_5 were relatively similar and N_2O_5 uptake lead to high concentrations of $ClNO_2$ in only one of the two fuels that had high aerosol chloride content. Additional experiments at higher relative humidity revealed that the N_2O_5 uptake coefficient only significantly increased in the deliquesced aerosol of high-chloride fuels. Our novel experiments provided the new understanding that the availability of aqueous chloride – often limited by particle morphology and low relative humidity – controls N_2O_5 reactivity on biomass-burning aerosol.

Understanding and being able to predict ice nucleating particle concentrations and sources in the ambient atmosphere rather than just from specific sources such as biomass burning is important for advancing the accuracy of cloud and climate models, and for a general understanding of what types of particles contribute to cloud glaciation in different regions. I was a participant in the Aerosol-Ice Formation Closure Pilot Study, which took place at the Department of Energy's Southern Great Plains (SGP) Atmospheric Radiation Measurement facility in Oklahoma. The purpose of this closure study was to collect data on ambient aerosol size distributions and chemical compositions to input into ice nucleation parameterizations, so that the predicted ice nucleating particle concentrations derived from these models could be compared to the measured ice nucleating particle concentrations. This provides the first evaluation of recent INP parameterizations using ambient aerosol and helps to identify gaps in our more fundamental understanding regarding the sources and behavior of atmospheric ice nucleants. I contributed by operating two instruments that measure aerosol size distributions, collecting ambient aerosol on

filters for subsequent offline ice-nucleation analysis, and operating an aerosol mass spectrometer to measure the chemical composition of submicron particulate matter. These data will be used by collaborators to evaluate and optimize various ice nucleation parameterizations and the inclusion of our measured aerosol composition has the potential to greatly improve these models. However, my more direct contribution is an in-depth analysis of the aerosol mass spectrometry data collected at the facility as there is a lack of high-resolution aerosol mass spectrometry data collected at continental background sites such as SGP. Aerosol concentrations throughout the month of October were quite low and were dominated by mixed, oxidized organic and inorganic aerosol. Comparisons to the existing low-resolution aerosol mass spectrometer at the facility revealed that substantial differences between the measured aerosol composition on some days, demonstrating the importance of deploying research-grade instrumentation into the field. Single-particle mass spectrometry data collected by another group member revealed that many distinct particle types were present, and that mineral-containing particles were ubiquitous. Most particles were still mixtures of broader classes such as organic aerosol, inorganic aerosol, and minerals. We will continue this analysis and collaboration with modelers for a deeper understanding of how the chemical composition of aerosol particles can help predict the ice nucleating ability of ambient aerosol.

Aerosol particles are constantly exposed to oxidants, sunlight, water vapor, and other gases and particles throughout their atmospheric lifetime, and my research has demonstrated how atmospheric transformations affect key aerosol properties. In both remote, clean areas of the atmosphere as well as regions influenced by intense biomass-burning smoke, changes on the molecular level can lead to large impacts on air quality and climate change, which is why atmospheric chemistry research is crucial to the future of our planet.

Table of Contents

List of Figures

Figure 2-3. Transmission electron microscopy (TEM) images of fresh BBA. **A-B)** are from ponderosa pine needles and **C)** is from sawgrass BBA collected on substrates indicating the presence of organic aerosol coatings around mineral-containing particles. Particle **A** is a fractal soot particle agglomerated with an iron-based mineral in the region indicated by the box. Particle **B** has a mixed core in region 1 composed of KCl, minerals, and carbonaceous material, with

Figure A2-4. Frozen fraction temperature spectra for BBA from two wood fuels. Ice nucleation analysis was performed by a traditional droplet-on-substrate technique; method details are described by Polen et al. (2016, 2018). BBA from birch wood **(A)** and fatwood **(B)** was subjected to ·OH photooxidation without additional NO_x, and no increase in INA was observed. Average background freezing temperature spectrum for filtered water shown as gray line; all BBA sample data for birch and fatwood lay within the water background freezing spectrum. Based off of previous work, EDX revealed less mineral formation in BBA produced from woods compared to tall grasses, with slightly more minerals present in birch BBA compared to fatwood BBA (Jahn et al., 2020). The combustion of these woods also produced the most black carbon (BC) in the aerosol compared to other fuels studied – birch BBA was 65% BC by mass and fatwood was 86% BC as measured by the SP-AMS. The reasoning behind the lack of increase in INA with aging observed here is consistent with our previous discussion. For wood fuels, there are few mineral-based ice-active sites present in even the fresh BBA, so any evaporation of organic carbon coatings – that revealed the mineral-based ice-active sites in BBA produced from grass combustion – made no difference in the INA of aged BBA produced from the combustion of these

List of Tables

List of Abbreviations

ACSM   aerosol chemical speciation monitor

AMS   aerosol mass spectrometer

AOT   aerosol optical tweezers

ARM   atmospheric radiation measurement (part of US Department of Energy)

BB   biomass burning

BBOA   biomass-burning organic aerosol

BC   black carbon

BBA   biomass-burning aerosol

CCN   cloud condensation nuclei

CFDC   continuous flow diffusion chamber

CIMS   chemical ionization mass spectrometer

DRH   deliquescence relative humidity

EDX   energy dispersive X-ray spectroscopy

HYSPLIT   HYbrid Single-Particle Lagrangian Integrated Tracker

IN   ice nuclei

INA   ice-nucleation activity

INP   Ice nucleating particle

LAAPTOF   laser ablation aerosol time of flight (mass spectrometer)

MOUDI   microorifice uniform deposit impactor

NO_x nitrogen oxide gases ($NO_x = NO + NO_2$)

n_s ice-active site density (per surface area of droplet)

OA   organic aerosol

ON   organonitrate

OOA	oxidized organic aerosol
OPC	optical particle counter
PM	particulate matter
$PM_{2.5}$	particulate matter 2.5 µm in diameter and under
PToF	particle time of flight
RH	relative humidity
S_a	surface area
SEM	scanning electron microscopy
SGP	Southern Great Plains (atmospheric observatory location)
SMPS	scanning mobility particle sizer
SOA	secondary organic aerosol
SP-AMS	soot particle – aerosol mass spectrometer
TD	thermodenuder
TEM	transmission electron microscopy
UV	ultraviolet (light)
VOC	volatile organic compound
$\gamma(N_2O_5)$	reactive uptake coefficient of dinitrogen pentoxide
$\varphi(ClNO_2)$	product yield of nitryl chloride

1 Introduction

1.1 Importance of studying atmospheric aerosol particles

Aerosol particles are small liquid, solid, or mixed-phase particles that are suspended in air. Atmospheric aerosol particles originate from biogenic (natural) sources or anthropogenic (human-caused) sources, and they are important because of their substantial effects on clouds, climate, and on air quality, which in turn affects human health and sustainability (Fuzzi et al., 2015). Some of the clearest and most deleterious environmental effects on human health are caused by particulate matter (PM), causing respiratory problems, heart attacks, and various cancers, all of which take years off of life expectancy in the United States just due to inhalation of PM (Bell et al., 2013; Davidson et al., 2005; Pope et al., 2009). Aerosol particles can directly impact the climate by either reflecting or absorbing solar radiation, resulting in cooling or heating, respectively. Furthermore, these particles can indirectly affect the climate by changing cloud microphysical properties, which then affect how much solar radiation is reflected or absorbed by the clouds, when and where clouds form, and how clouds precipitate. The complex nature of these interactions is what causes the Intergovernmental Panel on Climate Change (IPCC) to consider aerosols as the factor with the largest uncertainty in determining the magnitude of radiative forcing and climate change (IPCC, 2014).

Aerosol properties change as the particles are transported throughout the atmosphere. While larger particles gravitationally settle within a few hours, smaller particles can persist for up to several weeks and travel across continents. Throughout these lifetimes, aerosol particles are exposed to UV radiation, water vapor, oxidants, and other gases and particles, all of which cause the aerosol to change or "age." One major transformation pathway is the mass transfer of different aerosol components based off of their volatility distribution, allowing for the evaporation of some particle mass or the condensation of additional mass into new or existing particles (Donahue et

al., 2009; Robinson et al., 2007). Particles always experience some degree of oxidation from common oxidants that exist throughout the atmosphere, including ozone, hydroxyl radicals, nitrate radicals, and halogen radicals (Chapleski et al., 2016). Oxidation usually functionalizes molecules and lowers their volatility, but it can also fragment bonds and increase their volatility (Chuang and Donahue, 2016). Aerosol particles also can uptake water vapor or react heterogeneously with other gases, depending on particle composition (Faust and Abbatt, 2019). Oxidation, uptake, and other chemical reactions depend on the phase state and morphology of each aerosol particle (e.g. a combustion soot particle coated in a viscous, tarry organic material will not uptake water as readily as sea-spray aerosol) (Abbatt et al., 2012; Gorkowski et al., 2020; Zaveri et al., 2020). These aging mechanisms also depend on the amount of UV light that the aerosol is exposed to, especially since different oxidants are present during the day and night.

The research described in this dissertation was conducted with the overarching goal of improving the understanding of these changing aerosol particle properties relevant to complex atmospheric chemical systems to advance our knowledge of how human activities are altering atmospheric chemistry, air quality, clouds, and the climate. This new understanding can also advance policies and mitigation techniques to effectively decrease the negative impacts of aerosol particles on the climate and human health.

1.2   Biomass-burning aerosol

One common type of atmospheric aerosol is biomass-burning aerosol (BBA), which is emitted naturally during the burning of plant material in forest fires or can be initiated by human activity, including prescribed burns, accidental fires, or for fuel usage in developing nations. Biomass burning (BB) is a complex process that occurs globally, releasing large amounts of gaseous and aerosol pollutants. The BBA particles exhibit a wide range of sizes, mixing states, chemical compositions, and other properties (Reid et al., 2005). BBA represents a large fraction of global particulate matter: it contributes 78% of the total carbonaceous aerosol burden and 2700

Gg of black carbon per year – 36% of total black carbon emissions (Bond et al., 2013; Reddy and Boucher, 2004). These emissions can directly affect the Earth's solar radiation balance, as black carbon strongly absorbs light and has an estimated climate forcing of +1.1 W m^{-2} since the pre-industrial age, with the 90% uncertainty bounds ranging from +0.17 to +2.1 W m^{-2} (Bond et al., 2013). BBA can also indirectly affect the solar radiation balance by affecting cloud properties, either by acting as cloud condensation nuclei (CCN) or ice nucleating particles (INP), described in section 1.2.1 (Engelhart et al., 2012; Petters et al., 2009a; Seinfeld et al., 2016). In addition to affecting the climate system, BBA affects visibility, atmospheric chemistry and air quality, and is also particularly damaging to human health (Tuet et al., 2019). As the climate continues to warm and droughts become more prevalent, wildfires are increasing in their severity and frequency and there is evidence to suggest they will continue to worsen, further increasing the importance of studying all properties of BBA to understand their atmospheric processing and effects (McClure and Jaffe, 2018; O'Dell et al., 2019; Stevens-Rumann et al., 2018).

1.2.1   Ice nucleating properties of biomass-burning aerosol

One property of biomass-burning aerosol that has only recently been discovered is that it can contain ice nucleating particles (INPs) (Petters et al., 2009b). While these unique particles are present in the atmosphere only at very low concentrations – about 10 in a million particles – they can still have important effects on cloud microphysics and climate (DeMott et al., 2010). If a supercooled cloud droplet contains an ice nucleating particle, the particle can induce heterogeneous ice nucleation, causing the droplet to freeze (glaciate). Cloud glaciation is extremely important because of the effects it has on initiating precipitation, influencing atmospheric chemical reactions, altering cloud lifetime and size, and influencing the radiative forcing of a cloud system (DeMott et al., 2010). Figure 1-1 summarizes how having fewer or more ice nuclei (IN) present at different altitudes affects the ability of clouds to cool or warm the atmosphere below. There are four modes by which ice crystals can form in the atmosphere. The

3

first mode is *homogeneous freezing* which does not involve an INP: if a cloud droplet is cold enough, it can freeze homogeneously when the water cools to below ~ −35 ˚C. The other *heterogeneous* ice nucleation mechanisms require INPs and can initiate freezing at warmer temperatures than the homogeneous freezing temperature limit. These mechanisms are: *deposition freezing*, when water vapor deposits on the surface of an INP and freezes immediately; *contact freezing*, when an INP collides with a supercooled liquid droplet which then freezes immediately; and *immersion freezing*, when an INP is present in the liquid water droplet which then freezes when the droplet cools to a low enough temperature (Murray et al., 2012). Immersion freezing is thought to be the most prevalent freezing mode in atmospheric heterogeneous ice nucleation, and is therefore the freezing mode studied throughout this dissertation (Vali, 2014).
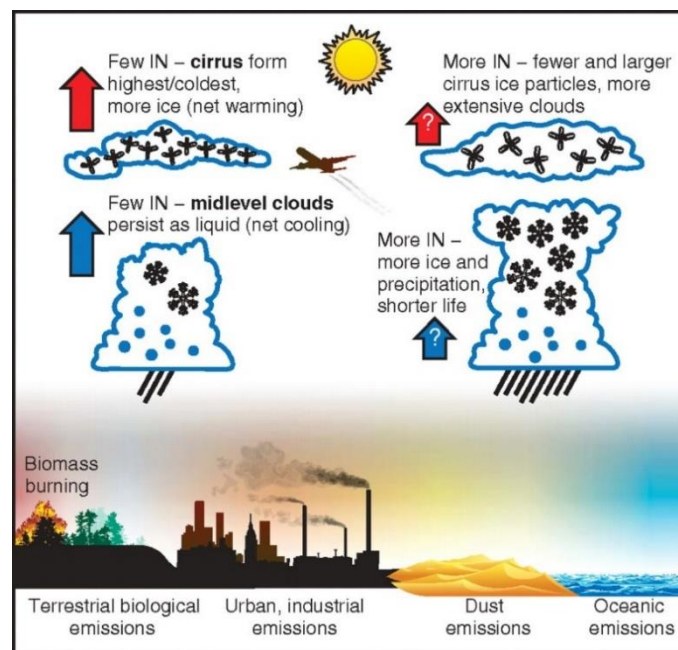
Figure 1-1. Diagram showing different sources of ice nucleants (IN), and how fewer or more IN in either midlevel or cirrus clouds would affect radiative cooling and warming. Reproduced from DeMott et al. (2010). More IN in midlevel clouds is thought to lead to more precipitation and shorter cloud lifetime, thereby reducing the cooling effect that these clouds usually have. More IN in higher cirrus clouds may compete with homogeneous freezing and result in fewer ice particles with shorter cloud lifetimes, thereby reducing the warming effect that cirrus clouds usually create.

In addition to biomass-burning aerosol, many other natural sources of INPs exist in the environment, including mineral dust, bioaerosols, ash, and soot, which are found all throughout the atmosphere, see Figure 1-2 (Kanji et al., 2017). Biological particles and mineral dusts tend to be more effective ice nucleants than BBA, but because these particle types can be present in different locations, it is still crucial to study every source of INP. This is especially true for biomass burning, given the large episodic injections of aerosol and INPs produced during major wildfires. Ten years ago, it was thought that all types of INPs required certain properties such as insolubility, a relatively large particle size, the ability for water to chemically bond to the INP's surface, and a crystallographic face (Murray et al., 2012). However since then, studies have indicated that some soluble salts can promote freezing, particles with amorphous structures have been found to be ice-active, and not all particles of a specific type (e.g. mineral, combustion soot, etc.) can effectively nucleate ice (Murray et al., 2012). Because of this, we cannot rely simply on these physical characteristics of particles or broad particle types to determine whether they nucleate ice in the atmosphere. Instead, we must experimentally determine how efficient different individual aerosol materials are at nucleating ice.
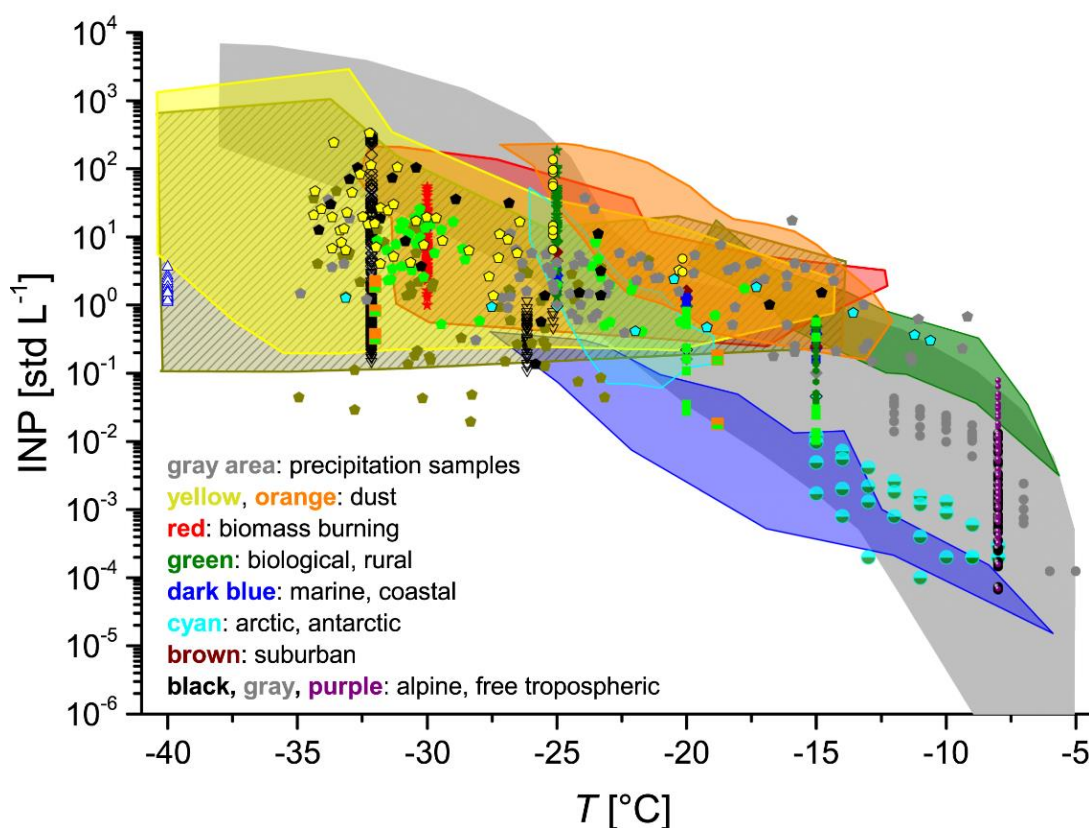
Figure 1-2. A representation of the concentration of INPs per liter of air at different temperatures from field studies across the globe. Figure is reproduced from Kanji et al., 2017, © American Meteorological Society, used with permission. Biological INPs are the most effective at nucleating ice as they have the highest INP concentration at the warmest temperatures. Dusts and biomass-burning aerosol nucleate ice at a colder and wide range of temperatures and are present at high concentrations.

There have not been many studies on the ice nucleating properties of biomass-burning aerosol, and the results have varied and generally found no strong correlations between ice-nucleation activity (INA) and bulk aerosol properties (Chou et al., 2013; DeMott et al., 2009; Korhonen et al., 2020; Levin et al., 2016; McCluskey et al., 2014; Petters et al., 2009b; Prenni et al., 2012; Twohy et al., 2010). High INA of BBA has been attributed to the black carbon formed during biomass combustion and to mineral dust from soil and bottom ash that can loft during intense fires (Kanji et al., 2017; Levin et al., 2016; McCluskey et al., 2014; Wagner et al., 2018). While lofted minerals and ashes may be important sources of INPs, more and more recent

research suggests that black carbon does not have strong INA at temperatures relevant to mixed-phase clouds (Kanji et al., 2020; Vergara-Temprado et al., 2018) . Furthermore, recent research in the Sullivan group demonstrated that mineral-based INPs are actually formed during the combustion process and are responsible for much of the ice activity in certain types of biomass fuel, see Figure 1-3 (Jahn et al., 2020).
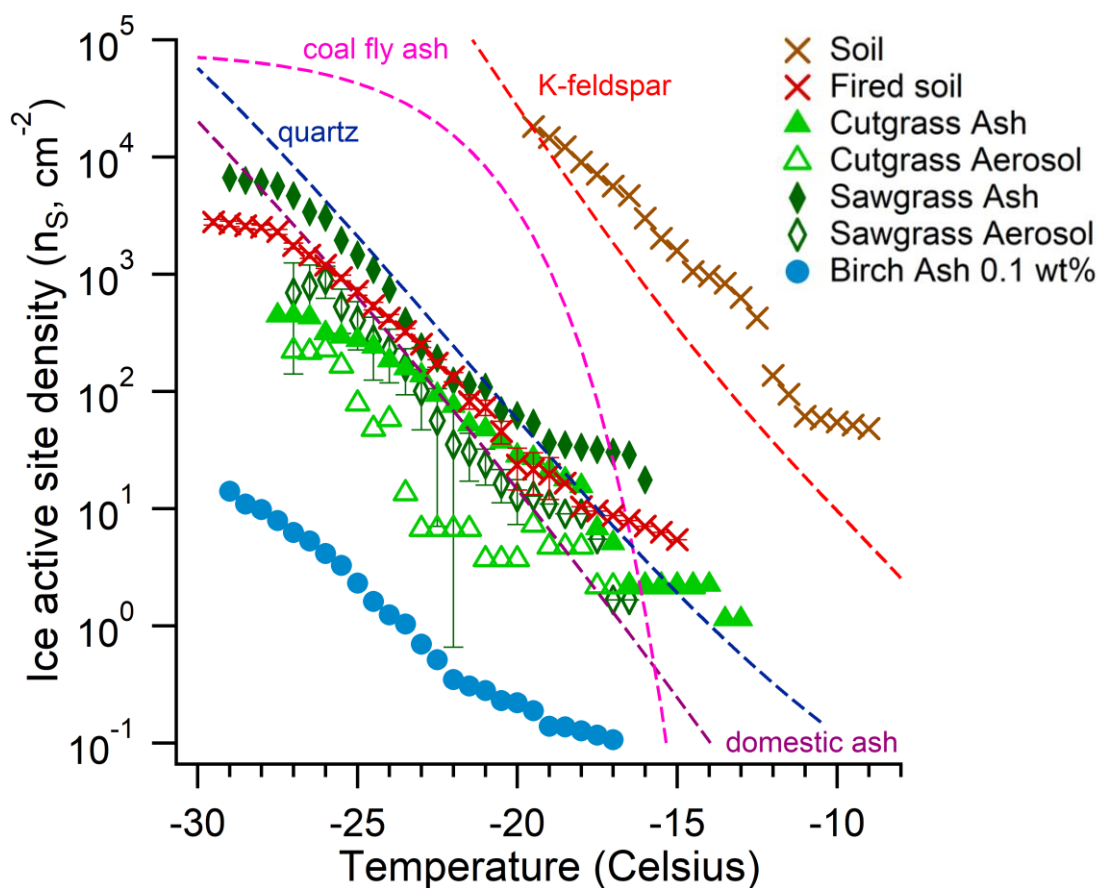
Figure 1-3. Ice-active surface site density (n_s) spectra of biomass-burning bottom ash (closed symbols) and aerosol (open symbols). Those samples produced from combustion of tall grasses (cutgrass and sawgrass) have higher INA than those produced from woods (birch) and are comparable to parameterizations of quartz minerals and domestic ash. Modified from Jahn et al. with additional details therein (Jahn et al., 2020).

1.2.2   Multi-phase chlorine chemistry in biomass-burning aerosol

Much of the research on biomass-burning emissions focuses on its carbonaceous components and release of greenhouse gases, but chlorine and nitrogen oxides (NO_x) also play an important role in different chemical reactions that occur within biomass-burning plumes. Chloride salts such as ammonium chloride and potassium chloride can make up to 50% of emitted $PM_{2.5}$ mass in BBA and one-third of global HCl gas emissions into the troposphere is from biomass burning (Keene et al., 1999; Levin et al., 2010). A renewed interest in chloride emissions from biomass burning (BB) and its effects on atmospheric chemistry started when high concentrations of nitryl chloride ($ClNO_2$) were measured in locations far from sea spray aerosol (Thornton et al., 2010). $ClNO_2$ forms when dinitrogen pentoxide (N_2O_5), a reservoir for NO_x during the night, is uptaken into aerosol particles containing chloride, see Figure 1-4 for the mechanism (Bertram and Thornton, 2009). These observations therefore meant that a source of particulate chloride other than the NaCl in sea spray aerosol needed to be considered. $ClNO_2$ has been detected in air masses that also carry other tracers for BB, but until recently there was no direct evidence that either N_2O_5 or $ClNO_2$ were formed in biomass-burning plumes (Tereszchuk et al., 2011; Tham et al., 2016). Understanding the sources, concentrations, and chemical reactions of these two molecules is extremely important as N_2O_5 uptake into particles affects NO_x cycling and $ClNO_2$ photolysis produces the chlorine radical, a potent oxidant (Li et al., 2020; Mcduffie et al., 2019; Riedel et al., 2014).
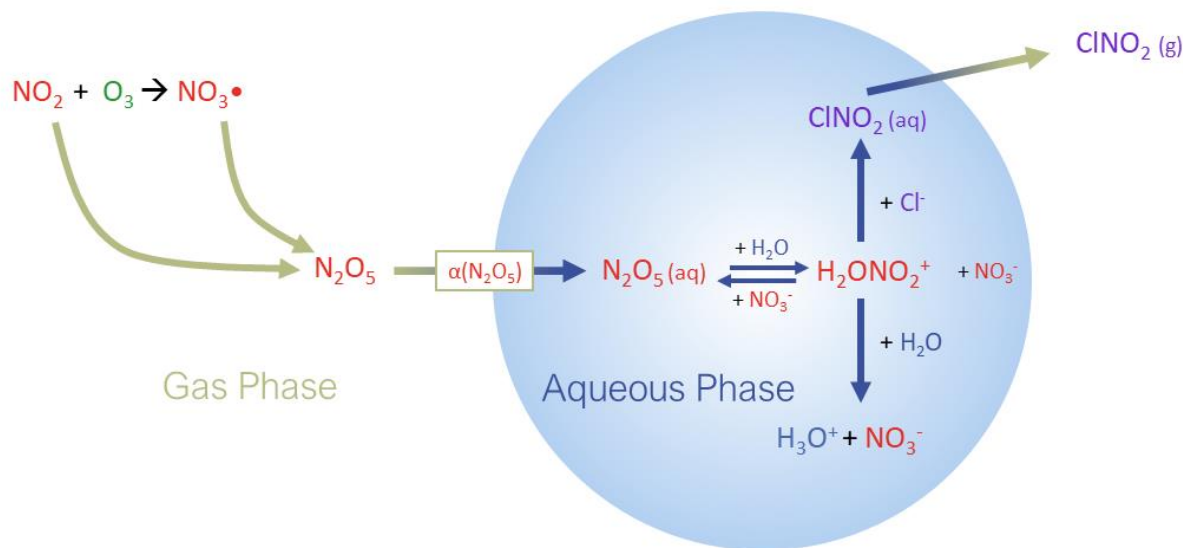
Figure 1-4. Schematic showing the multi-phase reaction of N_2O_5 with an aqueous salt droplet and subsequent production of $ClNO_2$. Figure based on Bertram & Thornton (2009).

The first experiments that demonstrated the formation of N_2O_5 and $ClNO_2$ in biomass-burning plumes were conducted by the Sullivan group in the Air Quality Lab at Carnegie Mellon University (Ahern et al., 2018). After injecting BBA from different biomass fuels into a smog chamber, small amounts of ozone were injected, immediately initiating the formation of N_2O_5 as well as the formation of $ClNO_2$ shortly thereafter, see Figure 1-5. For biomass fuels that contained higher fractions of particulate chloride, such as sawgrass and cutgrass, higher concentrations of $ClNO_2$ were observed. While these experiments were an important contribution to multi-phase chlorine chemistry knowledge, the use of large smog chambers does not allow for accurate calculations of the N_2O_5 reactive uptake coefficient, $\gamma(N_2O_5)$, or $ClNO_2$ yield, $\varphi(ClNO_2)$, motivating the flow tube kinetics experiments described in Chapter 3.
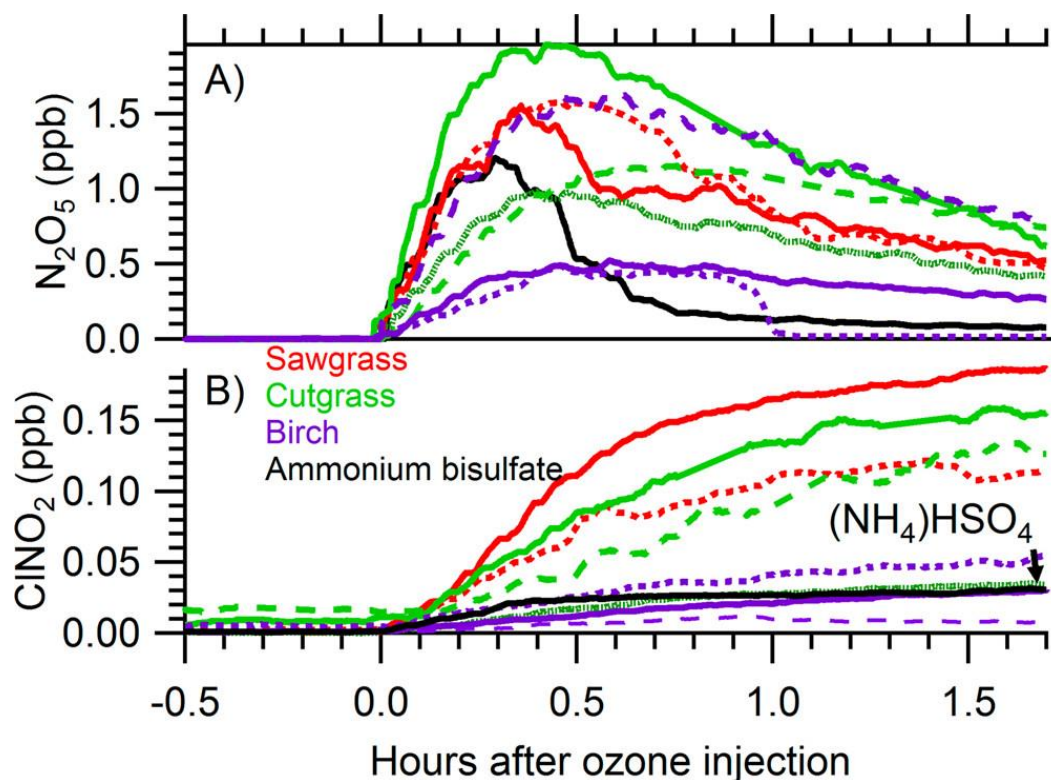
Figure 1-5. Production of A) N$_2$O$_5$(g) and B) ClNO$_2$(g) as measured by an iodide-adduct CIMS. Different colors correspond to different biomass fuels, black is an ammonium bisulfate control experiment, and replicate experiments of the same biomass fuel type are shown by different line styles. Reprinted with permission from *Environ. Sci. Technol.* 2018, 52, 2, 550-559. © 2018 American Chemical Society (Ahern et al., 2018).

1.3 Methods of aerosol characterization

1.3.1 Ice-nucleation activity

Several techniques currently exist for measuring ice nucleating particles and assessing their ice-nucleation activity (INA). The most common on-line analysis method is the continuous flow diffusion chamber (CFDC) (Rogers et al., 2001). The CFDC consists of an impactor to remove large particles that would be optically counted as ice crystals, two concentric ice-coated cylinders or plates set at different temperatures, with the aerosol flow in-between the plates. The aerosol is exposed to supersaturated conditions such that all particles activate into cloud droplets,

followed by a droplet evaporation region, and lastly an optical particle counter. The first two-thirds of each cylinder are coated in ice to provide the source of water vapor at ice supersaturated conditions. If a droplet contains a particle that is ice-active at the processing temperature, the droplet will freeze and the resulting ice crystal continues to grow. The last one-third of the cylinder is cold but below water saturation, causing any unfrozen water droplets to evaporate in this region while the ice crystals remain. As these crystals reach the end of the ice chamber, they are counted with an optical particle counter (OPC). The OPC considers particles larger than 3 µm as ice crystals, a valid assumption given that an impactor at the entrance of the CFDC eliminates particles greater than 2 µm and any water droplets not containing INPs would have evaporated before reaching the OPC. Similar commercial instruments based off the same principle are used such as the SPectrometer for Ice Nuclei (SPIN), commercially available by Droplet Measurement Technologies, and a CFDC made by Handix Scientific. While these techniques allow for portable, real-time measurements of INP concentrations, they often have high background INP count levels and cannot provide measurements across a wide range of temperatures. They are also large, heavy instruments due to their extensive refrigeration needs and are therefore not appropriate for all possible uses.

Offline measurements of INPs and their INA are based on cold plate systems with slight design variations but following the same general operating principles. Suspensions of aerosol particles are divided into individual droplets that are placed atop a slide on a cold stage that decreases in temperature at a controlled rate. Optical microscopes record videos of the droplets for post-analysis; the change in grayscale value signifies when (and therefore at what temperature) each droplet freezes. The slides are treated with hydrophobic solutions such as AquaSil Siliconizing Fluid or organosilanes in order to limit droplet freezing that may occur due to the contact with the slide or cold plate (Wright and Petters, 2013). Droplets are often surrounded by an immiscible oil to protect the droplets from being contaminated by the air and to limit droplet–

droplet interactions. This type of technique is often easier to use than online instruments and can measure the ice-activity of previously collected samples on a temperature continuum down to nearly homogeneous freezing temperatures, depending on the purity of the water used to suspend the aerosol sample, the substrate used, and how each droplet is separated from the others (Polen et al., 2018).

The type of INP measurement approach used in this dissertation is a cold stage technique combined with a novel microfluidic device recently developed in the Sullivan group. Particles collected on filters during biomass burning experiments were extracted into water experimentally tested to have the lowest level of background freezing (Polen et al., 2018). Microdroplets with a diameter around 150 μm and a volume of 6 nL were then generated from this suspension of particles using a store-and-create approach (Brubaker et al., 2020). The microfluidic chip containing about 600 droplets each isolated in its own microwell was then placed on a cold plate. The temperature was decreased at 1 °C per minute, with droplet freezing automatically detected using a Matlab script based on a change in the grayscale value of each droplet (Brubaker et al., 2020). The major advantage afforded by this novel technique is a low background freezing signal (shown in Figure 1-6) that begins below –32 °C, which is especially helpful when analyzing the ice nucleation properties of weak ice nucleants such as some BBA. The high droplet number statistics and superior reproducibility produces high-resolution droplet freezing temperature spectra that enable the detection of changes in INA, such as caused by chemical alteration of the ice nucleants in BBA, as is explored in Chapter 2.
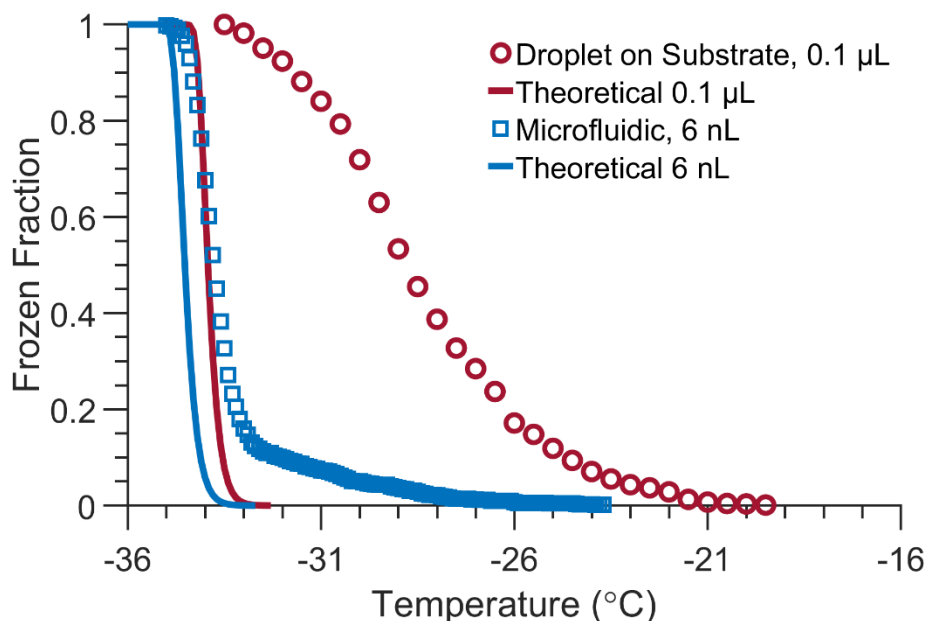
Figure 1-6. Droplet freezing (frozen fraction) temperature spectra of filtered water droplets obtained using a traditional droplet-on-substrate technique (Polen et al., 2018) versus a custom store-and-create microfluidic device (Brubaker et al., 2020). Figure is based on Brubaker et al., 2020, and is used with permission.

1.3.2   Aerosol mass spectrometry

The primary instrument used for characterization of aerosol particle chemical composition throughout this dissertation is the aerosol mass spectrometer (AMS), developed by Aerodyne Research Inc. (DeCarlo et al., 2006). An aerosol particle stream is focused through a critical orifice into an aerodynamic lens that transmits and focuses submicron aerosol, with 100% transmission efficiency for particles 150–700 nm in vacuum aerodynamic diameter (Liu et al., 2007). The particles then reach the particle time-of-flight region, where their vacuum aerodynamic diameter is determined by measuring the particles' flight times. Upon impacting a heated vaporizer held at 600 ˚C, organic carbon and non-refractory inorganic components vaporize and are subsequently ionized by a 70 eV electron source (DeCarlo et al., 2006). The high-resolution AMS uses orthogonal acceleration and reflectrons to increase the ion resolution of the time-of-flight mass

13

analyzer. A soot-particle module can be added to the AMS (called a soot-particle aerosol mass spectrometer, SP-AMS), in which a 1064 nm intracavity Nd:YAG laser intercepts the particle beam before the standard vaporizer, enabling the vaporization (and thus detection) of refractory components such as the black carbon (soot) present in biomass-burning aerosol (Onasch et al., 2012).

1.3.3   Other instrumentation

Another particle mass spectrometer complementary to the AMS is the laser ablation aerosol time-of-flight mass spectrometer (LAAPTOF, AeroMegt GmbH). The LAAPTOF samples particles up to ~2 μm in vacuum aerodynamic diameter and calculates their size based on their flight time between two continuous-wave 405 nm lasers (Shen et al., 2018). When each sampled particle scatters the light of the second laser, a UV 193 nm excimer laser is triggered, which simultaneously vaporizes and ionizes the particle (Ahern et al., 2016). This high-energy laser ablation enables measurements of particle components undetectable by the AMS, including mineral dusts, which are an important class of ice nucleating particle (Sullivan and Prather, 2005). The mass analyzer is low-resolution but bipolar, capable of measuring both positive and negative ions. The two polarities contain different but complementary information regarding particle composition that can be used to determine the source of and atmospheric processing the particle has experienced.

Analysis of atmospheric gases is often conducted by a high-resolution chemical ionization mass spectrometer (CIMS). This soft ionization scheme is highly selective and sensitive, allowing for targeted measurements of specific gaseous molecules at high time-resolution (Sullivan and Prather, 2005). Within this dissertation, iodide-adduct ionization was used as it is selective towards nitrogen oxides, some halogenated species, and some oxygenated volatile organic compounds, and its large mass-to-charge ratio and soft clustering allows for easy identification of of $N_2O_5(g)$ and $ClNO_2(g)$ (Lee et al., 2014, 2018). The iodide ion is generated by flowing nitrogen

over a permeation tube filled with methyl iodide across a radioactive source then is mixed with the sample flow so that the iodide ion clusters with the target molecules (e.g. $N_2O_5I^-$ and $ClNO_2I^-$) (Lee et al., 2014).

1.4   Thesis overview

The following section will outline each chapter of the dissertation. In chapter 2, I discuss experiments that investigate how the ice-nucleation activity of biomass-burning aerosol changes following simulated atmospheric aging of the aerosol. The sheer total mass of emitted BBA as well as its potential effects on the climate system necessitate this research, which is an expansion upon the experiments conducted by previous Sullivan group members and myself that shows that many different biomass fuels emit mineral-based INPs during combustion (Jahn et al., 2020). Biomass-burning aerosol evolves as it is transported throughout the atmosphere and prior literature suggests that the INA of different types of INPs can change via different aging processes. Therefore, the assumption that the INA of fresh BBA is identical to that of aged aerosol is inaccurate and warranted focused exploration. The research and experiments described in Chapter 2 provide a new understanding of how atmospheric aging affects the ice nucleation properties of BBA. Chapter 2 is under review for *Science Advances*.

In chapter 3, I present novel aerosol heterogeneous kinetics experiments that explore multi-phase chlorine chemistry occurring in authentic biomass-burning aerosol. Prior chamber experiments that I was involved with were the first to directly show that two atmospheric trace gases, N_2O_5 and $ClNO_2$, are produced in biomass-burning smoke plumes. To better understand how these molecules affect NO_x cycling and atmospheric radical oxidant budgets, I conducted the first experiments for determining the reactive uptake coefficient of dinitrogen pentoxide, $\gamma(N_2O_5)$, and the $ClNO_2$ yield, $\varphi(ClNO_2)$ with collaborators from the University of Washington. These are the first aerosol kinetics experiments conducted on authentic biomass-burning aerosol sub-sampled from biomass combustion emissions. The work presented in Chapter 3 is based on our

collaborative publication in the Royal Society of Chemistry journal *Environmental Science: Processes & Impacts*, as well as additional experimental work that I led and is being prepared for submission. The new work examines the effect of exposing the BBA to high relative humidity conditions to test the hypothesis that chloride salt deliquescence limits reactive uptake of $N_2O_5(g)$.

In chapter 4, I present aerosol mass spectrometry data that I collected during the Aerosol-Ice Formation Closure Pilot Study at the DOE ARM Southern Great Plains field station in Lamont, Oklahoma. The purpose of this collaborative pilot study was to measure aerosol properties including size distribution and chemical composition that are input into models that predict the concentration and properties of ice nucleating particles in the United States. The models can then be evaluated by comparing model outputs to the INP concentrations measured during the campaign. This type of closure study has never been conducted for ice nucleating particles, and the inclusion of the Sullivan Group's two mass spectrometers also provides key aerosol composition data that is often not included in ice nucleation models and has the potential to significantly improve the accuracy of cloud and climate models. Additionally, the detailed analysis made available by the high-resolution AMS is important for understanding the aerosol properties that cannot usually be determined by the instruments that are in continuous use at this permanent continental background field site such as oxidation state and composition-based size distributions. The high-resolution chemical composition can also be compared to low-resolution chemical composition collected by ARM to determine whether or not a high-resolution AMS is necessary for accurate measurements at background field sites. Chapter 4 will be combined with additional single-particle mass spectrometry data collected by another group member using the LAAPTOF and then submitted for publication.

In chapter 5, I conclude by summarizing my scientific contributions presented in this dissertation as well as suggest related future work. Throughout my five years at CMU, the Sullivan group has made tremendous contributions to the field of ice nucleation. But, as our work is the

first to identify newly-formed minerals as the ice-active components in biomass-burning aerosol that can change with atmospheric aging, further exploration of this topic is needed especially for incorporation into climate models. Similarly, we were also the first to study N_2O_5 and $ClNO_2$ heterogeneous chemistry in authentic biomass-burning aerosol, so replication of and expansion upon our work is warranted. The aerosol optical tweezers system in the Sullivan group would also be an excellent method for studying N_2O_5 uptake in individual aerosol droplets with different compositions and morphologies.

1.5 References

Abbatt, J. P. D., Lee, A. K. Y. and Thornton, J. A.: Quantifying trace gas uptake to tropospheric aerosol: Recent advances and remaining challenges, Chem. Soc. Rev., 41(19), 6555–6581, doi:10.1039/c2cs35052a, 2012.

Ahern, A. T., Subramanian, R., Saliba, G., Lipsky, E. M., Donahue, N. M. and Sullivan, R. C.: Effect of secondary organic aerosol coating thickness on the real-time detection and characterization of biomass-burning soot by two particle mass spectrometers, Atmos. Meas. Tech, 9, 6117–6137, doi:10.5194/amt-9-6117-2016, 2016.

Ahern, A. T., Goldberger, L., Jahl, L., Thornton, J. and Sullivan, R. C.: Production of N2O5 and ClNO2 through Nocturnal Processing of Biomass-Burning Aerosol, Environ. Sci. Technol., 52(2), 550–559, doi:10.1021/acs.est.7b04386, 2018.

Bell, M. L., Zanobetti, A. and Dominici, F.: Evidence on Vulnerability and Susceptibility to Health Risks Associated With Short-Term Exposure to Particulate Matter: A Systematic Review and Meta-Analysis, Am. J. Epidemiol., 178(6), 865–876, doi:10.1093/aje/kwt090, 2013.

Bertram, T. H. and Thornton, J. A.: Toward a general parameterization of N2O5 reactivity on aqueous particles: the competing effects of particle liquid water, nitrate and chloride, Atmos. Chem. Phys., 9, 8351–8363, 2009.

Bond, T. C., Doherty, S. J., Fahey, D. W., Forster, P. M., Berntsen, T., DeAngelo, B. J., Flanner, M. G., Ghan, S., Kärcher, B., Koch, D., Kinne, S., Kondo, Y., Quinn, P. K., Sarofim, M. C., Schultz, M. G., Schulz, M., Venkataraman, C., Zhang, H., Zhang, S., Bellouin, N., Guttikunda, S. K., Hopke, P. K., Jacobson, M. Z., Kaiser, J. W., Klimont, Z., Lohmann, U., Schwarz, J. P., Shindell, D., Storelvmo, T., Warren, S. G. and Zender, C. S.: Bounding the role of black carbon in the climate system: A scientific assessment, J. Geophys. Res. Atmos., 118(11), 5380–5552, doi:10.1002/jgrd.50171, 2013.

Brubaker, T., Polen, M., Cheng, P., Ekambaram, V., Somers, J., Anna, S. L. and Sullivan, R. C.: Development and characterization of a "store and create" microfluidic device to determine the heterogeneous freezing properties of ice nucleating particles, Aerosol Sci. Technol., 54(1), 79–

93, doi:10.1080/02786826.2019.1679349, 2020.

Chapleski, R. C., Zhang, Y., Troya, D. and Morris, J. R.: Heterogeneous chemistry and reaction dynamics of the atmospheric oxidants, O3, NO3, and OH, on organic surfaces, Chem. Soc. Rev., 45(13), 3731–3746, doi:10.1039/c5cs00375j, 2016.

Chou, C., Kanji, Z. A., Stetzer, O., Tritscher, T., Chirico, R., Heringa, M. F., Weingartner, E., Prévôt, A. S. H., Baltensperger, U. and Lohmann, U.: Effect of photochemical ageing on the ice nucleation properties of diesel and wood burning particles, Atmos. Chem. Phys., 13(2), 761–772, doi:10.5194/acp-13-761-2013, 2013.

Chuang, W. K. and Donahue, N. M.: A two-dimensional volatility basis set-Part 3: Prognostic modeling and NO x dependence, Atmos. Chem. Phys, 16, 123–134, doi:10.5194/acp-16-123-2016, 2016.

Davidson, C. I., Phalen, R. F. and Solomon, P. A.: Airborne Particulate Matter and Human Health: A Review, Aerosol Sci. Technol., 39(8), 737–749, doi:10.1080/02786820500191348, 2005.

DeCarlo, P. F., Kimmel, J. R., Trimborn, A., Northway, M. J., Jayne, J. T., Aiken, A. C., Gonin, M., Fuhrer, K., Horvath, T., Docherty, K. S., Worsnop, D. R. and Jimenez, J. L.: Field-deployable, high-resolution, time-of-flight aerosol mass spectrometer, Anal. Chem., 78(24), 8281–8289, doi:10.1021/ac061249n, 2006.

DeMott, P. J., Petters, M. D., Prenni, A. J., Carrico, C. M., Kreidenweis, S. M., Collett, J. L. and Moosmüller, H.: Ice nucleation behavior of biomass combustion particles at cirrus temperatures, J. Geophys. Res. Atmos., 114(16), D16205, doi:10.1029/2009JD012036, 2009.

DeMott, P. J., Prenni, A. J., Liu, X., Kreidenweis, S. M., Petters, M. D., Twohy, C. H., Richardson, M. S., Eidhammer, T. and Rogers, D. C.: Predicting global atmospheric ice nuclei distributions and their impacts on climate, Proc. Natl. Acad. Sci., 107(25), 11217–11222, doi:10.1073/pnas.0910818107, 2010.

Donahue, N. M., Robinson, A. L. and Pandis, S. N.: Atmospheric organic particulate matter: From smoke to secondary organic aerosol, Atmos. Environ., 43(1), 94–106, doi:10.1016/j.atmosenv.2008.09.055, 2009.

Engelhart, G. J., Hennigan, C. J., Miracolo, M. A., Robinson, A. L. and Pandis, S. N.: Cloud condensation nuclei activity of fresh primary and aged biomass burning aerosol, Atmos. Chem. Phys., 12(15), 7285–7293, doi:10.5194/acp-12-7285-2012, 2012.

Faust, J. A. and Abbatt, J. P. D.: Organic Surfactants Protect Dissolved Aerosol Components against Heterogeneous Oxidation, J. Phys. Chem. A, 123(10), 2114–2124, doi:10.1021/acs.jpca.9b00167, 2019.

Fuzzi, S., Baltensperger, U., Carslaw, K., Decesari, S., Denier Van Der Gon, H., Facchini, M. C., Fowler, D., Koren, I., Langford, B., Lohmann, U., Nemitz, E., Pandis, S. N., Riipinen, I., Rudich, Y., Schaap, M., Slowik, J. G., Spracklen, D. V., Vignati, E., Wild, M., Williams, M. and Gilardoni, S.: Particulate matter, air quality and climate: Lessons learned and future needs, Atmos. Chem. Phys., doi:10.5194/acp-15-8217-2015, 2015.

Gorkowski, K., Donahue, N. M. and Sullivan, R. C.: Aerosol Optical Tweezers Constrain the Morphology Evolution of Liquid-Liquid Phase-Separated Atmospheric Particles, Chem, 6(1), 204–220, doi:10.1016/j.chempr.2019.10.018, 2020.

IPCC: Climate Change 2014: Synthesis Report. Contribution of Working Groups I, II and III to the Fifth Assessment Report of the Intergovernmental Panel on Climate Change, Geneva,

Switzerland., 2014.

Jahn, L., Polen, M., Jahl, L. G., Brubaker, T., Somers, J. and Sullivan, R. C.: Biomass combustion produces ice-active minerals in biomass-burning aerosol and bottom ash, Proc. Natl. Acad. Sci., doi/10.1073/pnas.1922128117, 2020.

Kanji, Z. A., Ladino, L. A., Wex, H., Boose, Y., Burkert-Kohn, M., Cziczo, D. J. and Krämer, M.: Overview of Ice Nucleating Particles, Meteorol. Monogr., 58, 1.1-1.33, doi:10.1175/amsmonographs-d-16-0006.1, 2017.

Kanji, Z. A., Welti, A., Corbin, J. C. and Mensah, A. A.: Black Carbon Particles Do Not Matter for Immersion Mode Ice Nucleation, Geophys. Res. Lett., 47(11), 1–9, doi:10.1029/2019GL086764, 2020.

Keene, W. C., Khalil, M. A. K., Erickson, D. J., McCulloch, A., Graedel, T. E., Lobert, J. M., Aucott, M. L., Gong, S. L., Harper, D. B., Kleiman, G., Midgley, P., Moore, R. M., Seuzaret, C., Sturges, W. T., Benkovitz, C. M., Koropalov, V., Barrie, L. A. and Li, Y. F.: Composite global emissions of reactive chlorine from anthropogenic and natural sources: Reactive Chlorine Emissions Inventory, J. Geophys. Res. Atmos., 104(D7), 8429–8440, doi:10.1029/1998JD100084, 1999.

Korhonen, K., Bjerring Kristensen, T., Falk, J., Lindgren, R., Andersen, C., Carvalho, R. L., Malmborg, V., Eriksson, A., Boman, C., Pagels, J., Svenningsson, B., Komppula, M., Lehtinen, K. E. J. and Virtanen, A.: Ice-nucleating ability of particulate emissions from solid-biomass-fired cookstoves: an experimental study, Atmos. Chem. Phys, 20, 4951–4968, doi:10.5194/acp-20-4951-2020, 2020.

Lee, B. H., Lopez-Hilfiker, F. D., Mohr, C., Kurtén, T., Worsnop, D. R. and Thornton, J. A.: An Iodide-Adduct High-Resolution Time-of-Flight Chemical-Ionization Mass Spectrometer: Application to Atmospheric Inorganic and Organic Compounds, Environ. Sci. Technol., 48(11), 6309–6317, doi:10.1021/es500362a, 2014.

Lee, B. H., Lopez-Hilfiker, F. D., Schroder, J. C., Campuzano-Jost, P., Jimenez, J. L., McDuffie, E. E., Fibiger, D. L., Veres, P. R., Brown, S. S., Campos, T. L., Weinheimer, A. J., Flocke, F. F., Norris, G., O'Mara, K., Green, J. R., Fiddler, M. N., Bililign, S., Shah, V., Jaeglé, L. and Thornton, J. A.: Airborne Observations of Reactive Inorganic Chlorine and Bromine Species in the Exhaust of Coal-Fired Power Plants, J. Geophys. Res. Atmos., 123(19), 11,225-11,237, doi:10.1029/2018JD029284, 2018.

Levin, E. J. T., McMeeking, G. R., Carrico, C. M., Mack, L. E., Kreidenweis, S. M., Wold, C. E., Moosmüller, H., Arnott, W. P., Hao, W. M., Collett, J. L. and Malm, W. C.: Biomass burning smoke aerosol properties measured during Fire Laboratory at Missoula Experiments (FLAME), J. Geophys. Res., 115(D18), D18210, doi:10.1029/2009JD013601, 2010.

Levin, E. J. T., McMeeking, G. R., DeMott, P. J., McCluskey, C. S., Carrico, C. M., Nakao, S., Jayarathne, T., Stone, E. A., Stockwell, C. E., Yokelson, R. J. and Kreidenweis, S. M.: Ice-nucleating particle emissions from biomass combustion and the potential importance of soot aerosol, J. Geophys. Res. Atmos., 121(10), 5888–5903, doi:10.1002/2016JD024879, 2016.

Li, Q., Badia, A., Wang, T., Sarwar, G., Fu, X., Zhang, L., Zhang, Q., Fung, J., Cuevas, C. A., Wang, S., Zhou, B. and Saiz-Lopez, A.: Potential Effect of Halogens on Atmospheric Oxidation and Air Quality in China, J. Geophys. Res. Atmos., 125(9), doi:10.1029/2019JD032058, 2020.

Liu, P. S. K., Deng, R., Smith, K. a., Williams, L. R., Jayne, J. T., Canagaratna, M. R., Moore, K., Onasch, T. B., Worsnop, D. R. and Deshler, T.: Transmission Efficiency of an Aerodynamic Focusing Lens System: Comparison of Model Calculations and Laboratory Measurements for the

Aerodyne Aerosol Mass Spectrometer, Aerosol Sci. Technol., 41(8), 721–733, doi:10.1080/02786820701422278, 2007.

McClure, C. D. and Jaffe, D. A.: US particulate matter air quality improves except in wildfire-prone areas, Proc. Natl. Acad. Sci. U. S. A., 115(31), 7901–7906, doi:10.1073/pnas.1804353115, 2018.

McCluskey, C. S., DeMott, P. J., Prenni, A. J., Levin, E. J. T., McMeeking, G. R., Sullivan, A. P., Hill, T. C. J., Nakao, S., Carrico, C. M. and Kreidenweis, S. M.: Characteristics of atmospheric ice nucleating particles associated with biomass burning in the US: Prescribed burns and wildfires, J. Geophys. Res. Atmos., 119(17), 10458–10470, doi:10.1002/2014JD021980, 2014.

Mcduffie, E. E., Womack, C. C., Fibiger, D. L., Dube, W. P., Franchin, A., Middlebrook, A. M., Goldberger, L., Lee, B. H., Thornton, J. A., Moravek, A., Murphy, J. G., Baasandorj, M. and Brown, S. S.: On the contribution of nocturnal heterogeneous reactive nitrogen chemistry to particulate matter formation during wintertime pollution events in Northern Utah, Atmos. Chem. Phys, 19, 9287–9308, doi:10.5194/acp-19-9287-2019, 2019.

Murray, B. J., O'Sullivan, D., Atkinson, J. D. and Webb, M. E.: Ice nucleation by particles immersed in supercooled cloud droplets, Chem. Soc. Rev., 41(19), 6519, doi:10.1039/c2cs35200a, 2012.

O'Dell, K., Ford, B., Fischer, E. V and Pierce, J. R.: Contribution of Wildland-Fire Smoke to US PM 2.5 and Its Influence on Recent Trends, Environ. Sci. Technol., 53(4), 1797–1804, doi:10.1021/acs.est.8b05430, 2019.

Onasch, T. B., Trimborn, A., Fortner, E. C., Jayne, J. T., Kok, G. L., Williams, L. R., Davidovits, P., Worsnop, D. R., Hare, C., Olfert, J., Kimmel, J. R., Sueper, D., Coe, H., Allan, J., Cross, E., Ng, S., Liscinsky, D., Mcmanus, B. and Gonzalez, L.: Soot Particle Aerosol Mass Spectrometer: Development, Validation, and Initial Application, Aerosol Sci. Technol., 46, 804–817, doi:10.1080/02786826.2012.663948, 2012.

Petters, M. D., Carrico, C. M., Kreidenweis, S. M., Prenni, A. J., DeMott, P. J., Collett, J. L. and Moosmüller, H.: Cloud condensation nucleation activity of biomass burning aerosol, J. Geophys. Res., 114(D22), D22205, doi:10.1029/2009JD012353, 2009a.

Petters, M. D., Parsons, M. T., Prenni, A. J., DeMott, P. J., Kreidenweis, S. M., Carrico, C. M., Sullivan, A. P., McMeeking, G. R., Levin, E. J. T., Wold, C. E., Collett, J. L. and Moosmüller, H.: Ice nuclei emissions from biomass burning, J. Geophys. Res., 114(D7), D07209, doi:10.1029/2008JD011532, 2009b.

Polen, M., Brubaker, T., Somers, J. and Sullivan, R. C.: Cleaning up our water: Reducing interferences from nonhomogeneous freezing of "pure" water in droplet freezing assays of ice-nucleating particles, Atmos. Meas. Tech., 11(9), 5315–5334, doi:10.5194/amt-11-5315-2018, 2018.

Pope, C. A., Ezzati, M. and Dockery, D. W.: Fine-particulate air pollution and life expectancy in the United States., N. Engl. J. Med., 360(4), 376–386, doi:10.1056/NEJMsa0805646, 2009.

Prenni, A. J., Demott, P. J., Sullivan, A. P., Sullivan, R. C., Kreidenweis, S. M. and Rogers, D. C.: Biomass burning as a potential source for atmospheric ice nuclei: Western wildfires and prescribed burns, Geophys. Res. Lett., 39(11), n/a-n/a, doi:10.1029/2012GL051915, 2012.

Reddy, M. S. and Boucher, O.: A study of the global cycle of carbonaceous aerosols in the LMDZT general circulation model, J. Geophys. Res., 109(D14), D14202, doi:10.1029/2003JD004048, 2004.

Reid, J. S., Koppmann, R., Eck, T. F. and Eleuterio, D. P.: A review of biomass burning emissions part II: Intensive physical properties of biomass burning particles, Atmos. Chem. Phys., 5(3), 799–825, doi:10.5194/acp-5-799-2005, 2005.

Riedel, T. P., Wolfe, G. M., Danas, K. T., Gilman, J. B., Kuster, W. C., Bon, D. M., Vlasenko, A., Williams, E. J., Lerner, B. M., Veres, P. R., Roberts, J. M., Holloway, J. S., Lefer, B., Brown, S. S. and Thornton, J. A.: An MCM modeling study of nitryl chloride (ClNO2) impacts on oxidation, ozone production and nitrogen oxide partitioning in polluted continental outflow, Atmos. Chem. Phys., 14(8), 3789–3800, doi:10.5194/acp-14-3789-2014, 2014.

Robinson, A. L., Donahue, N. M., Shrivastava, M. K., Weitkamp, E. A., Sage, A. M., Grieshop, A. P., Lane, T. E., Pierce, J. R. and Pandis, S. N.: Rethinking organic aerosols: Semivolatile emissions and photochemical aging, Science., 315(5816), 1259–1262, doi:10.1126/science.1133061, 2007.

Rogers, D. C., DeMott, P. J., Kreidenweis, S. M. and Chen, Y.: A continuous-flow diffusion chamber for airborne measurements of ice nuclei, J. Atmos. Ocean. Technol., 18(5), 725–741, doi:10.1175/1520-0426(2001)018<0725:ACFDCF>2.0.CO;2, 2001.

Seinfeld, J. H., Bretherton, C., Carslaw, K. S., Coe, H., DeMott, P. J., Dunlea, E. J., Feingold, G., Ghan, S., Guenther, A. B., Kahn, R., Kraucunas, I., Kreidenweis, S. M., Molina, M. J., Nenes, A., Penner, J. E., Prather, K. A., Ramanathan, V., Ramaswamy, V., Rasch, P. J., Ravishankara, A. R., Rosenfeld, D., Stephens, G. and Wood, R.: Improving our fundamental understanding of the role of aerosol-cloud interactions in the climate system, Proc. Natl. Acad. Sci. U. S. A., 113(21), 5781–5790, doi:10.1073/pnas.1514043113, 2016.

Shen, X., Ramisetty, R., Mohr, C., Huang, W., Leisner, T. and Saathoff, H.: Laser ablation aerosol particle time-of-flight mass spectrometer (LAAPTOF): performance, reference spectra and classification of atmospheric samples, Atmos. Meas. Tech, 11, 2325–2343, doi:10.5194/amt-11-2325-2018, 2018.

Stevens-Rumann, C. S., Kemp, K. B., Higuera, P. E., Harvey, B. J., Rother, M. T., Donato, D. C., Morgan, P. and Veblen, T. T.: Evidence for declining forest resilience to wildfires under climate change, edited by F. Lloret, Ecol. Lett., 21(2), 243–252, doi:10.1111/ele.12889, 2018.

Sullivan, R. C. and Prather, K. A.: Recent Advances in Our Understanding of Atmospheric Chemistry and Climate Made Possible by On-Line Aerosol Analysis Instrumentation Recent Advances in Our Understanding of Atmospheric Chemistry and Climate Made Possible by On-Line Aerosol Analysis Instrum, Anal. Chem., 77(12), 3861–3886, doi:10.1021/ac050716i, 2005.

Tereszchuk, K. A., González Abad, G., Clerbaux, C., Hurtmans, D., Coheur, P.-F. and Bernath, P. F.: ACE-FTS measurements of trace species in the characterization of biomass burning plumes, Atmos. Chem. Phys. Atmos. Chem. Phys., 11, 12169–12179, doi:10.5194/acp-11-12169-2011, 2011.

Tham, Y. J., Wang, Z., Li, Q., Yun, H., Wang, W., Wang, X., Xue, L., Lu, K., Ma, N., Bohn, B., Li, X., Kecorius, S., Größ, J., Shao, M., Wiedensohler, A., Zhang, Y. and Wang, T.: Significant concentrations of nitryl chloride sustained in the morning: investigations of the causes and impacts on ozone production in a polluted region of northern China, Atmos. Chem. Phys, 16, 14959–14977, doi:10.5194/acp-16-14959-2016, 2016.

Thornton, J. A., Kercher, J. P., Riedel, T. P., Wagner, N. L., Cozic, J., Holloway, J. S., Dubé, W. P., Wolfe, G. M., Quinn, P. K., Middlebrook, A. M., Alexander, B. and Brown, S. S.: A large atomic chlorine source inferred from mid-continental reactive nitrogen chemistry, Nature, 464(7286),

271–274, doi:10.1038/nature08905, 2010.

Tuet, W. Y., Liu, F., De Oliveira Alves, N., Fok, S., Artaxo, P., Vasconcellos, P., Champion, J. A. and Ng, N. L.: Chemical Oxidative Potential and Cellular Oxidative Stress from Open Biomass Burning Aerosol, Environ. Sci. Technol. Lett., 6(3), 126–132, doi:10.1021/acs.estlett.9b00060, 2019.

Twohy, C. H., DeMott, P. J., Pratt, K. A., Subramanian, R., Kok, G. L., Murphy, S. M., Lersch, T., Heymsfield, A. J., Wang, Z., Prather, K. A. and Seinfeld, J. H.: Relationships of Biomass-Burning Aerosols to Ice in Orographic Wave Clouds Relationships of Biomass-Burning Aerosols to Ice in Orographic Wave Clouds, J. Atmos. Sci., 67, 2437–2450, 2010.

Vali, G.: Interpretation of freezing nucleation experiments: Singular and stochastic; Sites and surfaces, Atmos. Chem. Phys., 14(11), 5271–5294, doi:10.5194/acp-14-5271-2014, 2014.

Vergara-Temprado, J., Holden, M. A., Orton, T. R., O'Sullivan, D., Umo, N. S., Browse, J., Reddington, C., Baeza-Romero, M. T., Jones, J. M., Lea-Langton, A., Williams, A., Carslaw, K. S. and Murray, B. J.: Is Black Carbon an Unimportant Ice-Nucleating Particle in Mixed-Phase Clouds?, J. Geophys. Res. Atmos., 123(8), 4273–4283, doi:10.1002/2017JD027831, 2018.

Wagner, R., Jähn, M. and Schepanski, K.: Wildfires as a source of airborne mineral dust-revisiting a conceptual model using large-eddy simulation (LES), Atmos. Chem. Phys, 18, 11863–11884, doi:10.5194/acp-18-11863-2018, 2018.

Wright, T. P. and Petters, M. D.: The role of time in heterogeneous freezing nucleation, J. Geophys. Res. Atmos., 118(9), 3731–3743, doi:10.1002/jgrd.503652013, 2013.

Zaveri, R. A., Shilling, J. E., Zelenyuk, A., Zawadowicz, M. A., Suski, K., China, S., Bell, D. M., Veghte, D. and Laskin, A.: Particle-Phase Diffusion Modulates Partitioning of Semivolatile Organic Compounds to Aged Secondary Organic Aerosol, Environ. Sci. Technol., doi:10.1021/acs.est.9b05514, 2020.

2 Atmospheric Aging Enhances the Ice Nucleation Ability of Biomass-Burning Aerosol

2.1 Abstract

Ice nucleating particles (INPs) in biomass-burning aerosol (BBA) that affect cloud glaciation, microphysics, precipitation, and radiative forcing were recently found to be driven by the production of mineral phases. BBA experiences extensive chemical aging as the smoke plume dilutes and we explored how this alters the ice activity of the smoke using simulated atmospheric aging of authentic BBA in a chamber reactor. Surprisingly, atmospheric aging enhanced the ice activity for most types of fuels and aging schemes. The removal of organic carbon particle coatings that conceal the mineral-based ice-active sites by evaporation or oxidation then dissolution can increase the ice activity by greater than an order of magnitude. This represents a new model for the evolution of INPs from biomass burning where BBA becomes more ice active as it dilutes and ages, making a larger contribution to the INP budget, resulting cloud microphysics, and climate forcing than is currently considered.

2.2 Introduction

Biomass burning occurs globally year-round, releasing complex mixtures of organic and inorganic gaseous and particulate components, minerals, ash, and elemental carbon (soot) to the atmosphere, often in major episodic wildfire events that greatly perturb the Earth-cloud-climate system (Fromm et al., 2019). This burning of plant material occurs naturally in forest fires or can be initiated by prescribed burns or by accidental human activity. With the growth of drought-stricken regions, wildfires are expected to increase in extent and severity and occur in regions not

historically prone such as the southeastern United States (McClure and Jaffe, 2018; O'Dell et al., 2019; Stevens-Rumann et al., 2018; Williams et al., 2019). Biomass-burning aerosol (BBA) represents a large fraction of global particulate matter, contributing three-quarters of the total carbonaceous aerosol burden and over one-third of total black carbon emissions (Bond et al., 2013; Reddy and Boucher, 2004). BBA composition is complex, including organic carbon, elemental carbon, tarballs, minerals, ash, and inorganic salt phases, and this composition determines the aerosol properties and their effects on the atmosphere and climate systems (Adachi et al., 2019; Li et al., 2003; Reid et al., 2005; Sedlacek et al., 2018; Silva et al., 1999; Vassilev et al., 2013).

BBA can directly influence the Earth's radiative balance through the light absorbing properties of the black and brown carbon present, and the light scattering effects of the aerosol. Indirectly, BBA can affect cloud formation and precipitation through its ability to act as cloud condensation nuclei (CCN) (Engelhart et al., 2012; Lathem et al., 2013; Petters et al., 2009a) or ice nucleating particles (INPs). Cloud glaciation – which requires INPs to catalyze heterogeneous ice nucleation at temperatures warmer than –35 °C – affects the structure, lifetime, precipitation, and radiative properties of clouds. Accurate modeling of the Earth–climate system therefore requires achieving a much more complete understanding of heterogeneous ice nucleation and the sources and properties of different types of INPs (DeMott et al., 2010; Fan et al., 2016; Seinfeld et al., 2016). Considering the sheer mass of BBA emitted globally and the potential impacts of INPs on many atmospheric processes, the intersection of these two topics requires greater attention.

The fraction of BBA particles that are INP and their ice-nucleating abilities and freezing temperatures greatly vary depending on the type of fuel and combustion conditions (Chou et al., 2013; DeMott et al., 2009; Levin et al., 2016; McCluskey et al., 2014; Petters et al., 2009b; Prenni et al., 2012). The first direct evidence of INPs released during biomass-burning events was only

reported about ten years ago, wherein INPs were detected in the smoke of 9 out of 21 biomass fuels tested in laboratory studies (Petters et al., 2009b). The authors estimated that BBA is an important source of ice nucleating particles that leads to atmospheric INP concentrations that can significantly alter cloud properties on a regional scale. Further experiments detected INPs in the smoke of 13 out of 22 fuels tested, with the highest concentrations found during intense flaming combustion (Levin et al., 2016). Prenni et al. sampled ambient air downwind of prescribed burns and wildfires and detected high number concentrations of INPs during flaming-phase combustion (Prenni et al., 2012). In other field measurements INP concentrations were elevated during biomass-burning events, but the authors noted that soil lofted due to the intense fires may have contributed to the measured INPs (McCluskey et al., 2014). Most recently in Jahn et al. we demonstrated that new crystalline mineral phases produced during biomass combustion (i.e. not from lofted soil) are present in both the aerosol and remaining bottom ash. We concluded these minerals are the major source of ice nucleants in BBA, inducing immersion freezing at temperatures up to –13 °C, well above the temperatures at which graphitic soot particles can nucleate ice (Jahn et al., 2020). This suggests that the common assumption that the lofting of already existing dust and soil particles or the presence of ice-active carbonaceous soot particles are the major sources of INPs often found in BBA is inaccurate or incomplete.

The vast majority of studies of INPs from biomass burning have only examined freshly emitted aerosol particles or smoke intercepted of unknown atmospheric age. Yet, studies on the atmospheric processing of mineral-based INPs have revealed significant changes in ice-nucleation activity (INA) in some cases (Kulkarni et al., 2014; Möhler et al., 2008; Sullivan et al., 2010b, 2010a), suggesting that atmospheric processing may change the mineral-based INPs emitted in BBA. Although we recently established that carbonaceous soot cannot explain the ice nucleation we observe in a variety of nascent BBA from different fuels, it has been established that oxidative aging of graphitic soot surfaces can promote ice-nucleation activity (Mahrt et al.,

2018). These previous aging studies on single-component systems likely do not apply to BBA because of its complex heterogeneous composition, and only a few studies have examined authentic aged BBA. The photochemical aging of wood BBA in a chamber reactor was shown to have no effect on its INA, although the INA of this particular unaged BBA was quite low to begin with, only inducing immersion freezing at –35 °C (Chou et al., 2013). Conversely, wildfire smoke aerosol that travelled 1600 km had the highest ice-active particle number fraction out of all fires in one field study, suggesting that atmospherically aged BBA does retain its ice-nucleating ability or perhaps even experiences an enhancement in INA (Prenni et al., 2012). Taken together these findings suggest that there are strong yet unconstrained possibilities for alteration of the ice-nucleating ability of the mostly mineral-based INPs in BBA through atmospheric aging processes.

We have essentially no understanding of the susceptibility of these largely mineral-based biomass-burning INPs to atmospheric chemical aging processes or to what extent aging might alter these critical properties required for modeling the interactions of BBA with cloud systems and the hydrological cycle. Aerosol particles have atmospheric lifetimes of a week or more and the composition and properties of BBA change rapidly as the smoke plume dilutes and mixes with external reactants and oxidants. We therefore sought to investigate how the ice-nucleating ability of BBA is altered during atmospheric transport such as through evaporation and (photo)oxidation mechanisms by performing controlled simulated aging of BBA produced from the combustion of authentic fuels. We found that evaporation though dilution and exposure to oxidants often results in an increase in the INA of BBA, suggesting that biomass-burning plumes likely have more extensive effects on cloud microphysical properties and climate over larger spatial extents as the smoke is transported through the atmosphere than previously recognized.

2.3 Results

Authentic biomass fuels collected within the United States were burned, and the emissions from this open combustion were injected into a large Teflon smog chamber reactor (see Figure

A2-1 for an experimental schematic). The fuels selected are representative of those commonly burned in the western and southeastern United States during wildfires and prescribed burns. The size distribution and chemical composition of the resulting aerosol particles were analyzed online, and particles were also collected on various substrates for subsequent offline analysis. A "fresh" aerosol filter sample was collected from the chamber for two hours shortly after smoke injection and then extracted to assess the immersion freezing ice-nucleation activity (INA) using a novel microfluidic device (Brubaker et al., 2020). Then the simulated aging was initiated, and a separate "aged" filter sample was collected for the last two hours of the experiment. Four types of aging were conducted: 1) no external perturbation or oxidants added ('time aging'); 2) hydroxyl radical ($\cdot$OH) oxidation with added nitrogen oxides (NO_x); 3) removal of organic aerosol (OA) and other semi-volatile components using a thermodenuder prior to injection into the chamber, followed by $\cdot$OH oxidation; 4) injection of ozone with no UV photolysis (dark ozonolysis).

2.3.1 Enhancement of ice activity following time aging and evaporation of organic aerosol

The immersion-mode INA of the 'time aged' BBA collected between four to six hours after it remained in the chamber following injection and dilution of the emissions was notably increased for sawgrass and cutgrass BBA compared to BBA collected during the first two hours of each experiment (Figure 2-1A). These time aging experiments were conducted with no external oxidants added or other perturbations to compare to the stronger forced perturbations used in subsequent experiments; the BBA experiences appreciable evaporation just by dilution of the nascent smoke into the chamber. This increase in INA induced by several hours of holding the aerosol in the Teflon chamber is surprising given that any oxidants present in the nascent BBA would be quickly depleted – the elemental O:C (a measure of the OA oxidation state) for time aging experiments increased on the order of 30%, while other more aggressive aging regimes increased the OA oxidation state by > 90%. The increase in INA (n_s) here is larger than observed when external perturbation and/or oxidants were applied, as presented below.

Aerosol composition measurements indicate substantial evaporative loss of organic aerosol, seen through the decrease in the organic aerosol-to-black carbon (a conserved tracer) mass ratio (OA:BC) by up to 20% (Fig. 2-2A). BBA is well known to contain OA of intermediate to low volatility (their saturation vapor pressure) that can experience significant evaporation through smoke plume dilution (Hodshire et al., 2019a; Robinson et al., 2007), and vapor wall losses in Teflon chambers promote evaporation in laboratory experiments. The organic aerosol is heterogeneously distributed throughout the complex BBA and is often non-uniformly mixed in individual submicron particles that also contain soot, inorganic salts, and/or mineral phases (Jahn et al., 2020). The evaporation of semi-volatile OA observed here would reveal more of the ice-active surface sites already present in the BBA, allowing them to interact directly with water and nucleate ice that cannot occur when the sites are concealed. This explains the large increase in ice activity observed in the aged BBA and the sharp increase in the ice-active site density (n_s) over a narrow temperature range, which indicates the ice nucleants in both fresh and aged BBA have similar properties. BBA produced by the combustion of ponderosa pine needles contains many fewer Si-containing mineral particles compared to the grass fuels, which could explain why an increase in INA was not observed for this fuel type (Jahn et al., 2020).

2.3.2 Enhancement of ice activity through photooxidative aging

Consistent increases in INA following hydroxyl radical ($\cdot$OH) aging under high NO$_x$ conditions were demonstrated across most temperatures for all fuel types (Figure 2-1B), although the changes were smaller than in our time aging experiments with no added oxidants. Similar to the time aging experiments, the ponderosa pine needle BBA had the smallest increase in INA, only increasing at temperatures below –29.5 °C. The hydroxyl radical is an important and powerful atmospheric oxidant and was generated by UV photolysis of nitrous acid (HONO) injected into the chamber. The increase in INA could be due to oxidation of graphitic soot particle surfaces, oxidation of mineral surfaces, or possibly due to changes in the organic aerosol components that

are prone to ·OH oxidation. BBA that is dominated by black carbon and does not contain many mineral species as identified by TEM/EDX particle analysis tends to have low INA that does not increase with photooxidation. This is presumably because there are limited mineral-based ice-active sites to uncover; see Fig. A2-4 in the Appendix for further explanation.
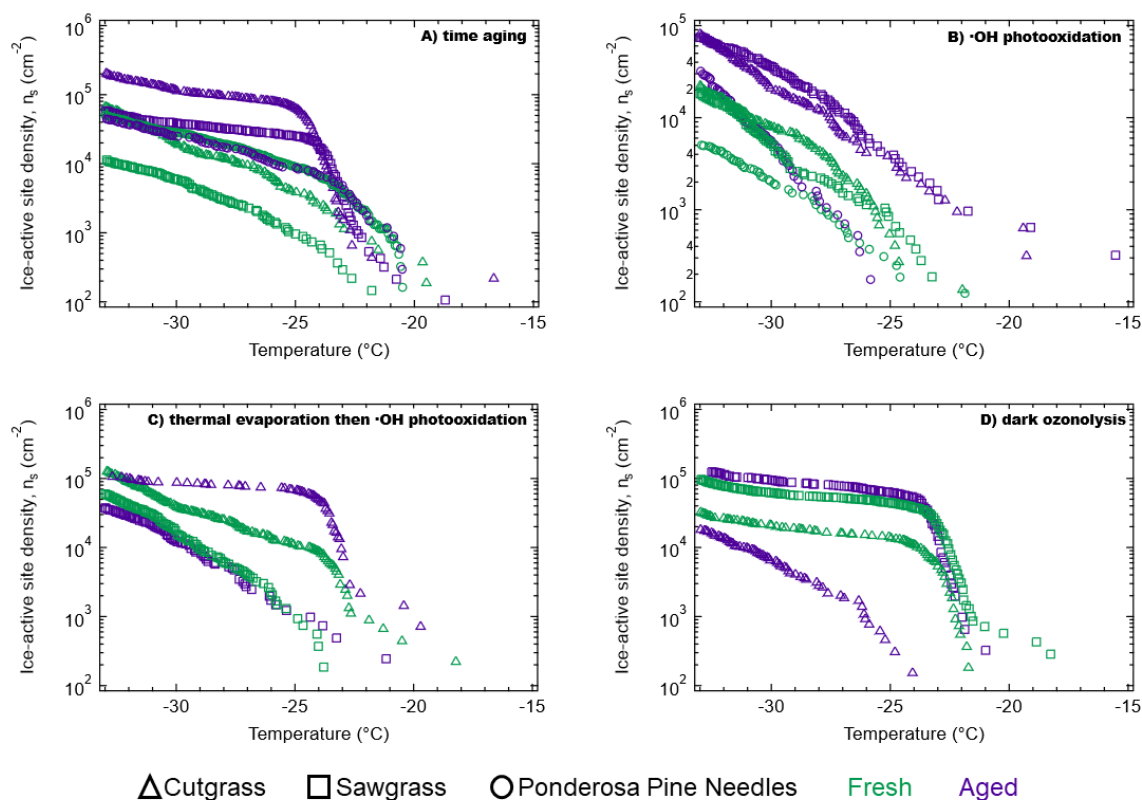
Figure 2-1. Ice-active surface site density (n_s) plotted versus freezing temperature. Each panel shows one type of aging of biomass-burning aerosol produced from combustion of cutgrass, sawgrass, or ponderosa pine. Fresh samples (prior to external perturbation or time aging) are shown in green and aged samples following several hours of chamber aging are shown in purple. **A)** time aging experiments revealed substantial increases in INA along with evaporation of organic carbon aerosol; **B)** hydroxyl radical photooxidative aging caused slight increases in INA (additional experiments shown in Fig. A2-2); **C)** thermal evaporation of the BBA followed by hydroxyl radical photooxidation revealed mixed effects on INA; and **D)** ozonolysis without photochemistry resulted in no observed changes or a prominent decrease in INA in one case, along with substantial increases in the organic aerosol mass loading. A subset of these experiments shown with 95% confidence intervals is provided in Figure A2-3 in the Appendix.

29

In order to understand how changes to the OA components could explain the observed increases in INA, we compared the volatility of fresh and aged biomass-burning OA by measuring the mass fraction remaining following thermal desorption at different temperatures up to 200 ºC (Appendix, Fig. A2-5) (Cain and Pandis, 2017). The aged aerosol consistently lost less OA mass than the fresh aerosol at every desorption temperature, indicating that aged BBA is less volatile than the fresh aerosol, similar to previous findings (Hennigan et al., 2011; Lim et al., 2019). This supports what was also observed in time-aging experiments where the more volatile OA present at the beginning of the experiments evaporated, uncovering ice-active surface sites and increasing the INA of aged BBA samples. Thermodenuder analysis also showed that the carbon oxidation state of the remaining organic aerosol components increased as indicated by an increased oxygen-to-carbon mass ratio following aging, corresponding to their decreased volatility (Fig. 2-2B). Since oxidation can also increase volatility through the organic carbon backbone fragmentation channel, the less-volatile OA observed here is the result of components that gained more oxygenated functional groups while avoiding fragmentation (Kroll et al., 2011).

Oxidation of organic carbon molecules tends to increase hydrophilicity and water solubility, such that the removal of OA from ice-active sites may be promoted by dissolution following oxidative aging. This mechanism would be highly relevant for immersion-mode freezing in mixed-phased clouds – the dominant heterogeneous ice nucleation mechanism that we studied here where the INP is immersed in a cloud droplet prior to nucleating ice. Liquid droplets containing these INPs may exist long enough prior to experiencing freezing conditions such that the more viscous, low-volatility organic compounds also dissolve and reveal ice-active sites in addition to the prompt removal of the more water-soluble oxidized organic carbon.
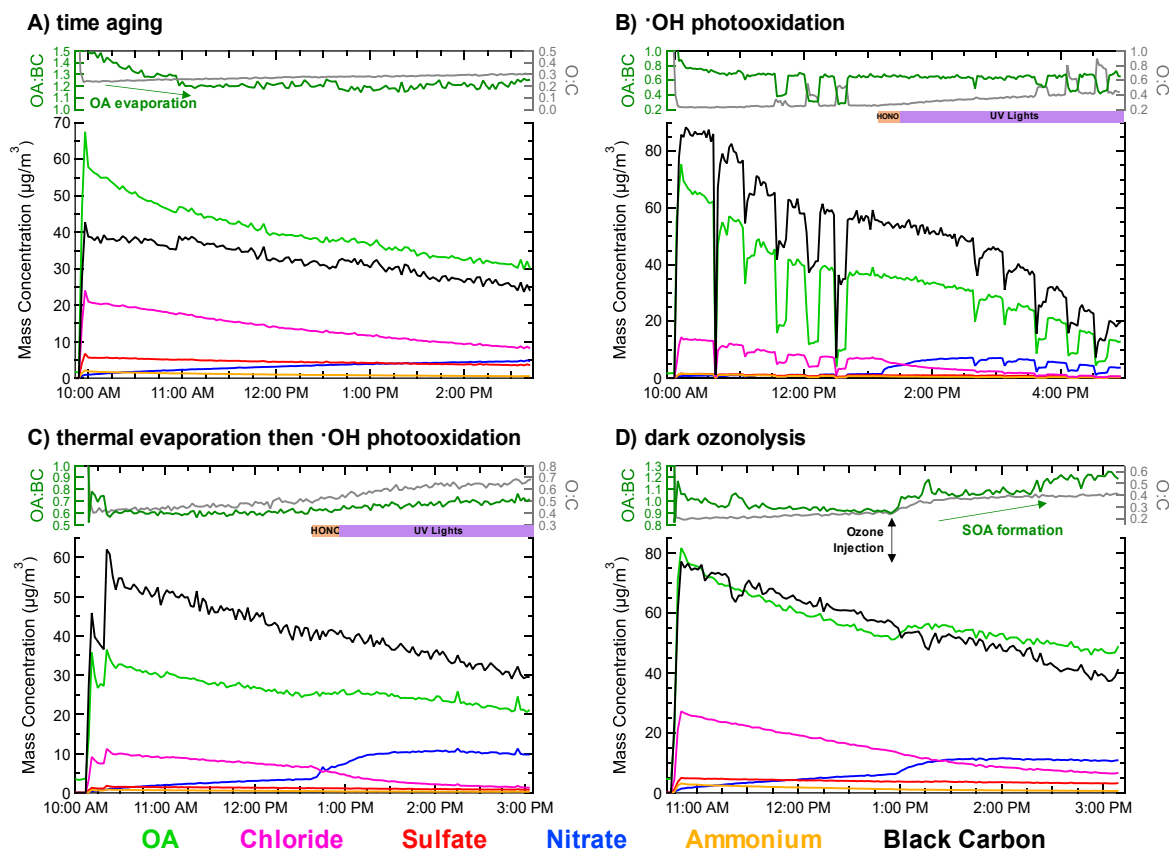
Figure 2-2. Exemplary evolution of submicron aerosol chemical composition in the four types of simulated atmospheric aging explored. Each panel shows SP-AMS chemical composition measured for one type of aging. Mass concentration (trace color corresponds to chemical component) in SP-mode is plotted in the lower portion; the organic aerosol:black carbon ratio – a measure of the gain or loss of OA versus the conserved BC tracer that only undergoes chamber wall loss – is plotted on the upper left axis. A measure of OA oxidation state, the O:C atomic ratio from EI-mode measurements, is plotted on the upper right axis. OA:BC and O:C are unreliable during the first few minutes of experiment while the chamber is filling. **A)** Cutgrass time aging experiment with considerable evaporation of organic aerosol observed in the OA:BC ratio. **B)** Sawgrass photooxidation experiment; HONO injection is shown by the orange bar and UV illumination by the purple bar. Sudden decreasing mass concentration and increasing O:C occurred when the aerosol particles were passed through a heated thermodenuder before entering the SP-AMS. **C)** Sawgrass experiment where the BBA was subjected to thermal desorption at 250 °C before injection into chamber. HONO injection is shown by the orange bar and UV illumination by the purple bar. **D)** Cutgrass dark ozonolysis experiment, with 350 ppb of ozone injected at the labeled time. The formation of SOA is indicated through the increase in OA:BC following ozone injection.

31

2.3.3 Alteration of ice activity from photooxidation following thermal evaporation of semi-volatile aerosol components

No consistent trend in INA was observed following the photooxidation of BBA that had first been subjected to thermal desorption (Figure 2-1C). In these experiments, most OA was removed by passing the biomass emissions through a thermodenuder heated to 250 °C prior to injection into the smog chamber. A smaller amount of organic mass entered the chamber compared to unheated BBA; refer to Figure 2-2C for an example of aerosol composition. This method allowed us to examine the INA of the initial aerosol population stripped of most of the OA. The subsequent addition of the hydroxyl radical directly targets the oxidative aging of the aerosol composed of the remaining very low volatility organic carbon components, inorganics, minerals, and graphitic soot.

In the cutgrass experiment there was a sharp increase in the ice-active site density specifically at –23 °C following thermal evaporation then oxidation. This suggests an enhancement in a specific type of ice-active site because of the large increase in INA in a narrow temperature range. One possible type is the mineral phases present in BBA, which could more effectively nucleate ice upon exposure to the hydroxyl radical, especially since the removal of the more volatile OA in the thermodenuder would expose more of the mineral surfaces. Another candidate ice-active site in BBA is graphitic soot, whose surfaces could also become exposed after the removal of the more volatile OA. ·OH oxidation could also produce surface hydroxyl groups on the graphitic surfaces that will interact strongly with water through hydrogen bonding. The molecular dynamics simulations of Lupi and Molinero revealed that OH-modified graphitic surfaces were more effective at inducing freezing than unmodified graphitic surfaces (Lupi and Molinero, 2014). Increased hydrophilicity of soot particles through atmospheric aging has been demonstrated experimentally to increase INA at cirrus cloud temperatures < –40 °C (Koehler et al., 2009; Mahrt et al., 2018, 2020b, 2020a). While authentic combustion soot particles are not typically ice active at mixed-phase cloud temperatures > –35 °C (Kanji et al., 2017; Mahrt et al., 2018), it is possible that the soot particles emitted from some types of biomass fuel combustion

are ice active at warmer temperatures than soot from fossil fuel combustion, and/or that these soot particle surfaces are more susceptible to enhancements in INA through oxidation.

In the sawgrass experiment, the denuded fresh and aged aerosol had nearly the same INA. While the trends in INA for the thermally denuded aerosol vary by experiment, it is noteworthy that these experiments with most OA removed still result in ice-active site densities above background levels and within the same orders of magnitude as unaltered fresh BBA. This further supports the idea that ice-active sites in BBA active under immersion-freezing conditions are not organic carbon-based. Our prior analysis of the BBA and ash produced from these same fuels concluded that the production of new mineral phases from the biomass combustion itself is the major source of the ice nucleants, and that fuels that produced the most soot had the weakest or even unmeasurable INA at temperatures warmer than –25 ºC (Jahn et al., 2020).

2.3.4 Impairment of ice activity from production of secondary organic aerosol by dark ozonolysis

The INA of BBA subjected to dark ozonolysis was lower than that of fresh aerosol, likely due to the production of secondary organic aerosol that covered ice-active surface sites (Fig. 2-1D). In this aging mechanism ~300 ppb of ozone was injected into the chamber with no UV light illumination. Previous studies have shown that dark ozonolysis reliably produces significant SOA mass and the largest increase in total OA from biomass-burning emissions, making this aging mechanism a good test for the effects of SOA production and OA particle coatings on ice activity (Ahern et al., 2019; Tkacik et al., 2017). Note that some ·OH is still generated without UV photolysis, produced by the ozonolysis of unsaturated organic molecules such as monoterpenes or alkenes (Paulson, 1996; Tkacik et al., 2017). Dark ozonolysis did result in the greatest SOA production compared to other aging mechanisms, with the OA:BC mass ratio increasing by up to 25%, as shown in Figure 2-2D.

The fresh and aged BBA had essentially the same ice-nucleating abilities following dark ozonolysis or even a decrease in INA for the cutgrass experiment (Fig. 2-1D). We attribute this to increasing SOA coating amount and thickness on the BBA, counteracting the effects of the evaporation and oxidation plus dissolution of OA observed in the time aging and ·OH aging experiments. These results also indicate that the SOA coatings are not sufficiently removed when the aerosol is extracted into water for immersion freezing analysis, perhaps because the SOA generated during dark ozonolysis is less fragmented and of lower water solubility and therefore remains concealing the ice-active sites. The already existing primary hydrocarbon-like OA likely only partially coats the highly heterogeneous BBA particles and SOA production may also act to more completely coat the complex aerosol through condensation of oxidized OA. Indeed SOA of an oxidation state similar to the O:C of the aged BBA in our experiments is often found to phase separate from the aqueous phase and adopt a core–shell morphology with the organic phase on the outside (Gorkowski et al., 2020).

2.3.5 Analysis of individual biomass-burning aerosol particles

The collected BBA was analyzed at a single-particle level using transmission electron microscopy (TEM) to investigate the potential particle types that are responsible for the observed ice activity and how these respond to the simulated aging. Many mineral-based particles coated in organic carbon phases were observed. Figure 2-3A shows a fractal soot particle that is agglomerated with an iron-based mineral as determined by energy dispersive X-ray (EDX) spectroscopy. The particle in Figure 2-3B contains potassium chloride salts and a mineral core made of magnesium, aluminum, silicon, and oxygen, also surrounded by an organic coating that appears to have partially evaporated under the vacuum of the TEM. The particle in Figure 2-3C has several inorganic salt phases surrounded by a dense organic carbon coating. These particle types and mixtures are all representative of fresh BBA filter samples where heterogeneous ice nucleation was observed above –25 °C. Note that the small < 500 nm size of the mineral

components suggests that these were formed during combustion, as the majority of minerals lofted by mechanical action from soil dust or biomass ash would be supermicron. In our previous work, the most crystalline mineral phases were present in all samples of both aerosol and ash from the tall grass fuels, which also contain more INPs and have higher INA than BBA from wood fuels (Jahn et al., 2020). As most mineral particles in the BBA were found to be submicron, these potential INPs will have longer lifetimes versus gravitational settling, undergo atmospheric transport over longer distances, and exert more extensive effects on cloud microphysics over larger spatial scales than the much larger supermicron lofted ash particles would (Jahn et al., 2020).
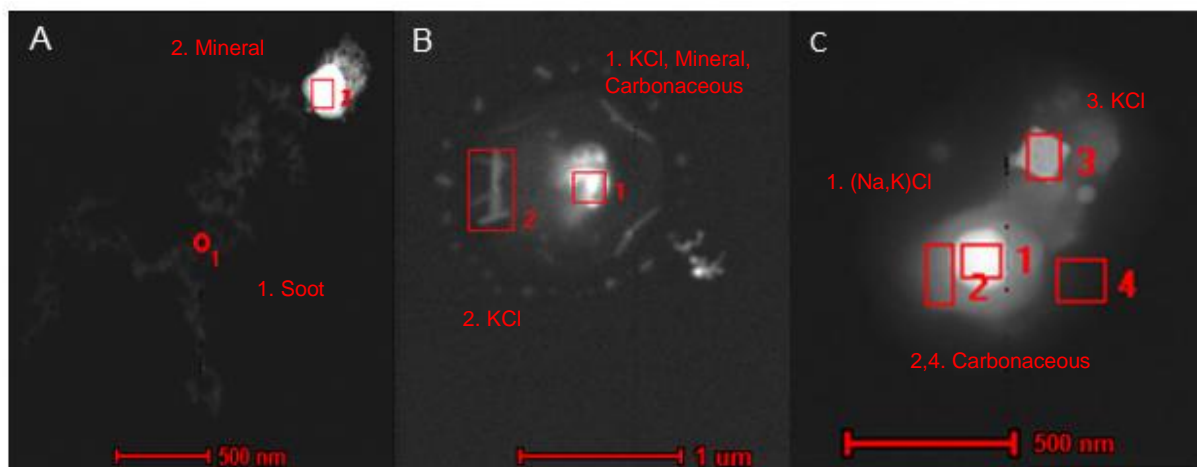
Figure 2-3. Transmission electron microscopy (TEM) images of fresh BBA. **A-B)** are from ponderosa pine needles and **C)** is from sawgrass BBA collected on substrates indicating the presence of organic aerosol coatings around mineral-containing particles. Particle **A** is a fractal soot particle agglomerated with an iron-based mineral in the region indicated by the box. Particle **B** has a mixed core in region 1 composed of KCl, minerals, and carbonaceous material, with additional KCl in region 2 and a carbonaceous OA coating that appears gray surrounding the entire particle. Particle **C** contains several inorganic salt phases in regions 1 & 3 and is also surrounded by an OA coating that appears gray in regions 2 & 4. EDX spectra of the boxed regions are provided in Fig. A2-6.

2.4   Discussion

Simulated atmospheric aging indicates that the ice-nucleation activity and INP number concentration of authentic BBA would generally increase as the aerosol undergoes atmospheric transport, though plume dilution must also be accounted for. The evaporation of organic coatings off the BBA reveals mineral-based ice-active sites, increasing the ice-nucleating ability of the BBA during most experiments. Simulations based off of FLAME III biomass-burning experiments estimated that 35% of the loss of OA after combustion was due to organic evaporation driven by loss of semi-volatile OA following smoke dilution into the chamber and vapor partitioning to the chamber walls (Bian et al., 2015). Fresh BBA is composed of 20-90% organic carbon compounds, a substantial fraction of which are known to evaporate upon dilution from near-fire to dispersed plume aerosol concentrations, but overall evaporation rates and partitioning depends on many factors such as aerosol mass loading, fuel type and combustion conditions, and dilution rate (Hodshire et al., 2019a). These factors also contribute to the variability in INA amongst other studies of INPs from biomass burning.

Loss of OA through natural evaporation or evaporation also driven by photooxidation was observed in the time aging experiments as well as during ·OH photooxidation and therefore these two aging mechanisms both resulted in similar trends in INA. The additional chemical oxidation during ·OH photooxidation experiments likely increased the water solubility of OA particle coatings, allowing for easier dissolution during immersion-mode experiments and uncovering of ice-active surface sites. However, more secondary organic aerosol (SOA) mass was generated during the latter part of the ·OH aging experiments compared to the time aging experiments where total OA only decreased in time. This may account for the smaller increase in ice-active site density following ·OH photooxidation by not resulting in as extensive an uncovering of ice-active sites as in the time aging experiments with more significant evaporation of OA. Direct oxidation

of mineral surfaces within the BBA may have also led to the increased INA observed in aged BBA produced from mineral-rich grass fuels, but this mechanism could not be directly tested.

Even greater SOA production such as from dark ozonolysis (that avoids OA fragmentation by photolysis) further conceals ice-active sites on the particles, resulting in no increase or even a decrease in INA with aging. Previous literature has shown that SOA coatings can decrease the INA of other INPs in some instances. For example, Arizona test dust and the mineral dust illite were coated with SOA created from the ozonolysis of α-pinene, and aerosol mass fractions percentages of SOA as low as 17% were found to decrease the deposition-mode INA of these atmospheric mineral dust proxies (Möhler et al., 2008). However, the immersion-mode INA of desert mineral dusts did not significantly change when coated in SOA produced from α-pinene ozonolysis (Kanji et al., 2019). Here, SOA produced by the dark ozonolysis of authentic biomass-burning smoke appears to be concealing the ice-active sites in BBA, presumably because the biomass burning SOA is more effective at covering the ice-active sites compared to prior terpene SOA coating experiments. The SOA produced here may also be less volatile and more viscous than the proxy SOA created through α-pinene ozonolysis and therefore remain concealing ice-active sites during immersion-mode freezing. While different studies demonstrate variable degrees of SOA production or OA loss in biomass-burning plumes, our results are relevant for plumes that undergo significant SOA production, such as those from larger fires in more polluted areas (Hodshire et al., 2019b; Shrivastava et al., 2017).

Figure 2-4 illustrates a new framework to understand how INPs from biomass burning and their chemical composition and ice-nucleation activity co-evolve during plume dilution and atmospheric processing based on these new findings. Evaporation of organic aerosol occurs to different extents following the emission and dilution of the smoke and leads to an increased availability of ice-active surface sites. Photooxidation of organic compounds changes the chemical composition to produce more oxidized OA with increased water solubility such that when

37

the particle is immersed in a cloud droplet prior to undergoing immersion freezing, the OA can dissolve more readily to reveal ice-active sites. Condensation of SOA, driven by more oxidized and less volatile OA produced from evaporated organic carbon (that avoids the fragmentation channel), conceals ice-active sites on the particles and decreases the apparent INA. Authentic biomass-burning plumes undergo varying degrees of evaporation, oxidation, and re-condensation of organic aerosol (Ahern et al., 2019; Donahue et al., 2011; Garofalo et al., 2019). These processes compete simultaneously to different degrees, depending on fuel composition, combustion conditions, dilution ratios, and atmospheric conditions surrounding biomass plumes that entrain background air and reactants into the plume as it dilutes and spreads (Hodshire et al., 2019b). Therefore, all these processes must be taken into account when considering the INA of BBA during or following atmospheric aging.

This work is the first to investigate how INPs released by the combustion of several different biomass fuels evolve under different simulated atmospheric aging schemes. A strong enhancement of the INA through some types of atmospheric aging was discovered. INA increased more after aging in BBA produced by the combustion of grassy fuels – which have a much higher mineral content – than other fuels like pine needles and woods that produce BBA with higher organic aerosol and black carbon content instead. These differences can be attributed to the observed changes in particle properties and composition that lead to an uncovering of pre-existing ice-active surface sites that we recently demonstrated are mostly mineral phases produced by the biomass combustion itself (Jahn et al., 2020; Vassilev et al., 2013). TEM images of the BBA collected in these experiments also clearly show mineral phases and their mixtures with other particle components such as BC soot and salt phases that are often coated by organic carbon.
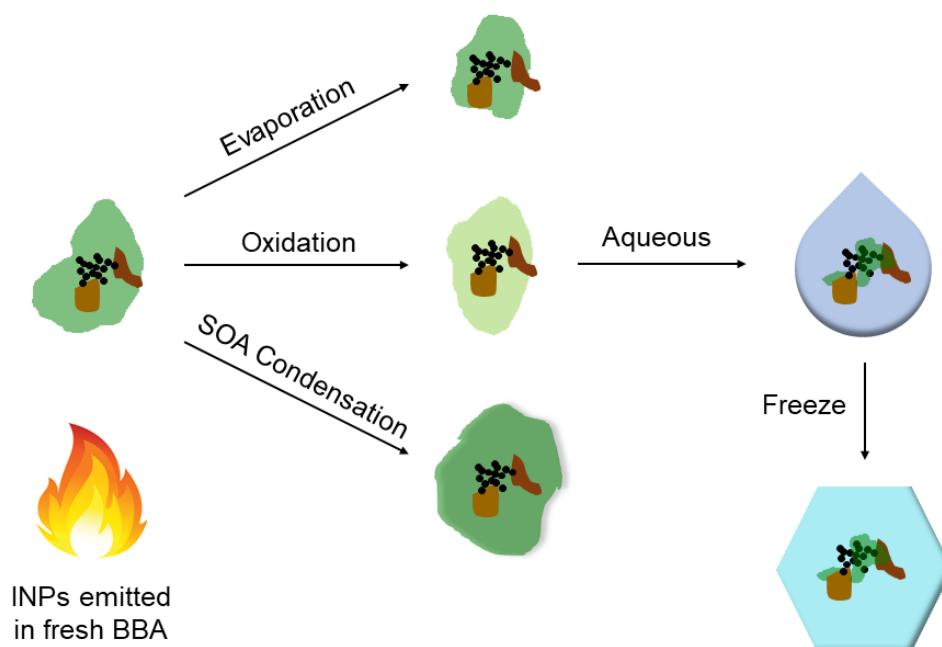
Figure 2-4. Schematic representation of the atmospheric co-evolution BBA composition and ice-nucleation activity. The particle contains minerals depicted in shades of brown, soot depicted in black, and organic aerosol depicted in green. Evaporation of OA leads to increased availability of ice-active sites. Oxidation of OA changes its chemical composition to be more oxidized and water-soluble organic carbon such that when the particle is immersed in a droplet the OA can dissolve more readily to reveal ice-active sites. Secondary organic aerosol (SOA) condensation from oxidation and condensation of organic carbon onto the particle conceals ice-active sites.

Here, we show how the INA of biomass-burning aerosol can be enhanced through some types of relevant atmospheric aging mechanisms. Unlike many previous studies that have shown that the INA of mineral dust particles can sometimes be impaired through atmospheric aging, here we find some types of aging actually enhance the INA of BBA (Cziczo et al., 2009; Möhler et al., 2008; Sullivan et al., 2010b, 2010a). The different effects of aging for these two mineral-containing aerosol systems are due to the presence of primary components emitted in the nascent BBA that can conceal the ice-active particle surfaces such as the mineral phases. Aging can lead to the partial removal of these coatings, thus increasing the INA. Mineral dust particles do not typically

contain primary particle coatings that resist dissolution such as the hydrocarbon-like tar material common in BBA (Adachi et al., 2019; Pósfai et al., 2004; Sedlacek et al., 2018). For atmospheric mineral dust, any coatings are acquired through atmospheric aging thus concealing or chemically altering ice-active surface sites with soluble inorganic components or oxidized SOA that sometimes lead to a decrease in INA.

Dilution, evaporation, and exposure of the BBA to oxidants often results in an increase of ice-active site density greater than an order of magnitude even at temperatures above –25 °C and an increase in the onset freezing temperature of up to 8 °C. This process would likely be enhanced under many atmospherically relevant scenarios as OA evaporation is driven more rapidly and extensively by the continual dilution of the smoke plume during transport that proceeds for several days or even weeks for submicron aerosol; most of the mineral particles observed in the BBA that are the likely source of ice nucleation were submicron in size. Removal of these OA coatings can also make reactive mineral and halide salt phases available for direct reaction with atmospheric reactants, such as the activation of chlorine as $ClNO_2(g)$ and $HCl(g)$ from $Cl^-(aq)$ through reactive uptake of $N_2O_5(g)$ that we have recently demonstrated in BBA (Ahern et al., 2018; Goldberger et al., 2019).

The implications of this new framework for the co-evolution of biomass-burning aerosol composition and ice-nucleation activity are that the emitted ice nucleating particles will make important contributions to the distribution of atmospheric INPs over larger spatial and temporal extents and at warmer cloud temperatures than previously understood. In fact, the effective concentration of INPs emitted in BBA will increase during plume dilution as particle coatings experience net evaporation, until dilution of the aerosol particle numbers overcomes this effect. Previous estimates of the INP concentration in fresh BBA emitted during wildfires include 10^6–10^{15} INPs per m^2 of burned land (active at –30 °C) based on a variety of tested fuels, and 5×10^{10}–1×10^{12} INPs per m^2 of burned grassland (active at –25 °C) based on our recent report on INPs

emitted by combustion of tall grasses. This estimate of INP emissions results in an area of 10^4 km^2 with a 5 km plume height having INP concentrations elevated above typical background levels due to biomass burning and likely sufficient to modify cloud microphysics, from just 1 m^2 of burned land (Jahn et al., 2020; Petters et al., 2009b). Our results presented here show that atmospheric aging enhances the ice-active site density by up to a factor of 27 at –25 °C. Therefore, atmospheric aging of BBA could increase the area affected by INPs by at least one decade, causing an estimated area of 10^5 km^2 by 5 km in altitude to be affected for each 1 m^2 of burned grassland. These observed increases in ice activity in terms of both INP concentration and freezing temperature are substantial considering the vast areas of biomass consumed in wildfires, especially in recent years. Fully understanding the impacts of this newly understood dynamic evolution of the INPs in BBA requires investigation using chemical transport models that properly account for the evolution of BBA composition during atmospheric transport (Bian et al., 2017; Hodshire et al., 2019a).

2.5   Methods

A small portion of each biomass fuel was placed into a partially enclosed galvanized steel pan and lit from the side with a butane lighter. The remaining biomass fuel was gradually added to maintain flaming phase combustion, until a total of 0.5 kg was burned. The smoke emissions were injected and diluted using Dekati eductor diluters (Dekati DI-1000) into a 12 m^3 Teflon smog chamber (Ahern et al., 2018; Jahn et al., 2020). Before each experiment, the chambers were purged overnight using filtered clean air and UV lights until particle number concentrations were < 50 cm^{-3}. The fuels used were giant cutgrass (*zizaniopsis miliacea*), obtained at the UF/IFAS Center for Aquatic and Invasive Plants in Florida, USA; ponderosa pine needles (*pinus ponderosa*) obtained at the Klamath Basin National Wildlife Refuge Complex in Tulelake, California, USA; sawgrass (*cladium jamaicense*), obtained at the Loxahatchee National Wildlife Refuge in Florida, USA; and birch and fatwood logs, purchased locally.

Online particle analysis included a scanning mobility particle sizer (SMPS, TSI Inc.: DMA model 3082 and CPC model 3775) for aerosol size distribution measurements between 8 and 749 nm in mobility diameter, and a soot-particle aerosol mass spectrometer (SP-AMS, Aerodyne Inc.) for submicron particle chemical characterization. The SP-AMS uses an infrared laser to measure refractory black carbon (BC) soot, and the instrument was operated with switching the IR laser on/off every 60 seconds (Onasch et al., 2012). During both modes, a 600 °C tungsten thermal vaporizer was used to vaporize non-refractory aerosol components: organic carbon aerosol (OA), nitrate, sulfate, chloride, and ammonium. Laser-on (BC) mode was used to obtain the mass concentrations shown in Figure 2-2, and the O:C mass ratio was determined from laser-off (EI) mode. For volatility analysis, the aerosol was alternated between passing through a heated thermodenuder (centerline residence time of 23 s) or through an unheated bypass line before being sampled by the SP-AMS. Gas monitors included a chemiluminescent NO_x analyzer (Advanced Pollution Instrumentation, Inc., Model 200A) and an ozone analyzer (Teledyne, Model T400). Particles were collected onto copper formvar TEM grids (carbon type B, 400 mesh, Ted Pella #01754-F) for offline electron microscopy analysis. TEM/EDX measurements were acquired at the Environmental Molecular Sciences Laboratory (EMSL) at PNNL using a Titan 80-300 scanning/transmission electron microscope equipped with an Si(Li) detector at an accelerating voltage of 300 keV.

Particles were collected for ice nucleation analysis on polycarbonate filters (GE Healthcare 111103, Nuclepore 50 nm pore size) using an inline 44 mm filter holder and refrigerated until use. Immediately before analysis, particles were extracted off of the filter by vortexing the filter in a polypropylene Falcon tube with 3 mL of HPLC-grade water (Sigma Aldrich HPLC Plus #34877) that was pre-filtered (Anotop 25 Plus 0.02 μm pore size, Whatman #6809-4102), as this results in the lowest level of background freezing (Polen et al., 2018). The suspension was then filled into a custom microfluidic chip where 600 uniformly sized isolated 6 nL droplets are produced and can

be tested simultaneously with a background freezing temperature for filtered water of < -33 °C (Brubaker et al., 2020). The chip was placed atop a thermoelectric cooling element and cooled at 1 °C min^{-1}, with droplet freezing detected using the observed change in grayscale value. The ice-active surface site density (n_s) was calculated using the total surface area of the collected aerosol samples based off of the total air volume passed through the filters and an averaged aerosol size distribution measured by SMPS during the fresh or aged BBA collection period (Vali, 1971). For some earlier experiments presented in the SI, the droplet freezing assay was performed using a conventional droplet-on-substrate method and 0.1 µL droplets (Polen et al., 2018).

2.6 Acknowledgements

2.7   Appendix

Summary

Below we show six additional figures to support our findings presented in the main manuscript. Figure A2-1 shows the experimental setup of the chamber used for authentic biomass-burning aerosol (BBA) aging experiments. Figure A2-2 shows additional ice-active site density (n_s) vs. temperature spectra for fresh and aged BBA through ·OH photooxidation not depicted in Figure 2-1 to prevent overcrowding the main figure. As discussed in the main paper, all of these samples had an increase in INA with photooxidative aging across at least some temperature ranges.

Figure A2-3 shows selected ice-active site density (n_s) vs. temperature spectra with 95% confidence intervals, demonstrating which aging experiments exhibited statistically significant changes between the INA of fresh versus aged BBA. Shaded 95% confidence intervals shown were calculated following the Monte Carlo method presented by Vali (Vali, 2019). Briefly, each freezing experiment was discretized into 0.25 °C temperature bins. Then μ, the number of droplets that freeze in each temperature bin, can be approximated as a Poisson process and the random spread of μ approaches a Poisson distribution. A series of 100 outcomes are drawn from each Poisson distribution to produce 100 simulated experiments, each with a new n_s (INA) spectrum. The linearly interpolated 2.50% and 97.5% quantiles of n_s at each discrete temperature are then interpreted as the 95% confidence intervals (p = 0.05).

Figure A2-4 shows the raw frozen fraction temperature spectra (rather than n_s plots, because all droplets froze within the filtered water background freezing temperature range) for two wood BBA samples. This demonstrates that photooxidative aging does not increase the INA of BBA produced from wood combustion, which tends to produce fewer mineral particles and more soot compared to the tall grass fuels. Figure A2-5 shows the mass fraction of organic aerosol remaining after passing through a heated thermodenuder – used to determine the volatility of the

fresh and aged BBA. Figure A2-6 shows TEM/EDX spectra of the BBA particles depicted in Figure 2-3, used to determine the chemical composition of different regions of individual particles. Many particles have organic aerosol coatings which evaporate to reveal ice-active sites, leading to an increase in INA for aged BBA.
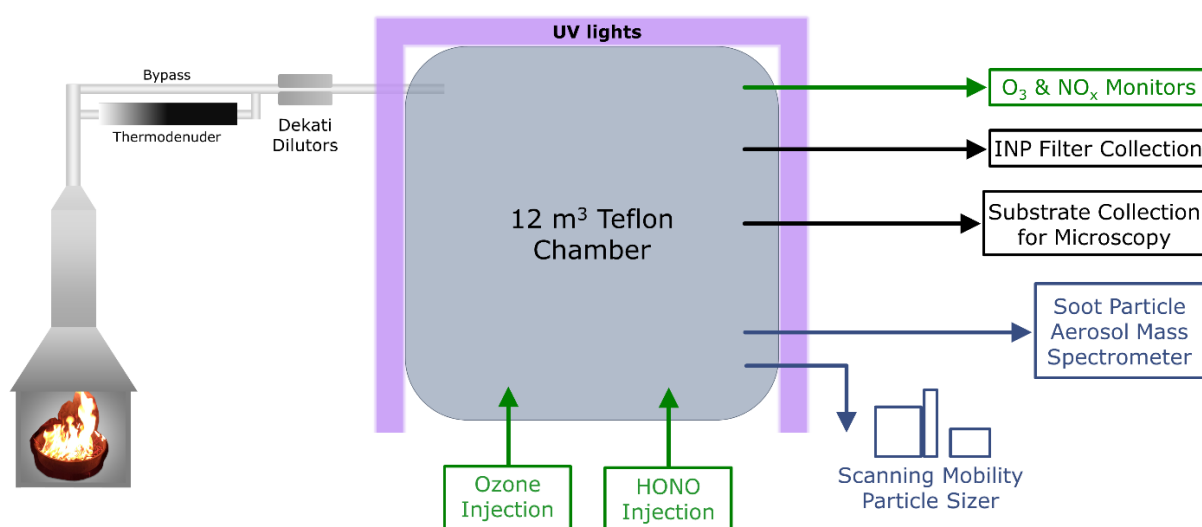
Figure A2-1. Experimental setup for chamber aging of authentic BBA. Experiments were conducted in the combustion facility of the CMU Air Quality Laboratory. Each fuel was burned in a galvanized steel pan inside a partial enclosure. Clean air diluted and pulled the resulting smoke into a 12 m^3 Teflon chamber which was thoroughly flushed overnight with clean air and UV radiation before each experiment. For experiments with BBA passed through the thermodenuder before chamber injection, the Dekati dilutors were operated at a lower flowrate to increase the residence time of the aerosol in the thermodenuder. Ozone was produced from pure $O_2(g)$ using a corona discharge ozone generator and nitrous acid (HONO) vapor was produced from the headspace of a solution of sodium nitrite and sulfuric acid.
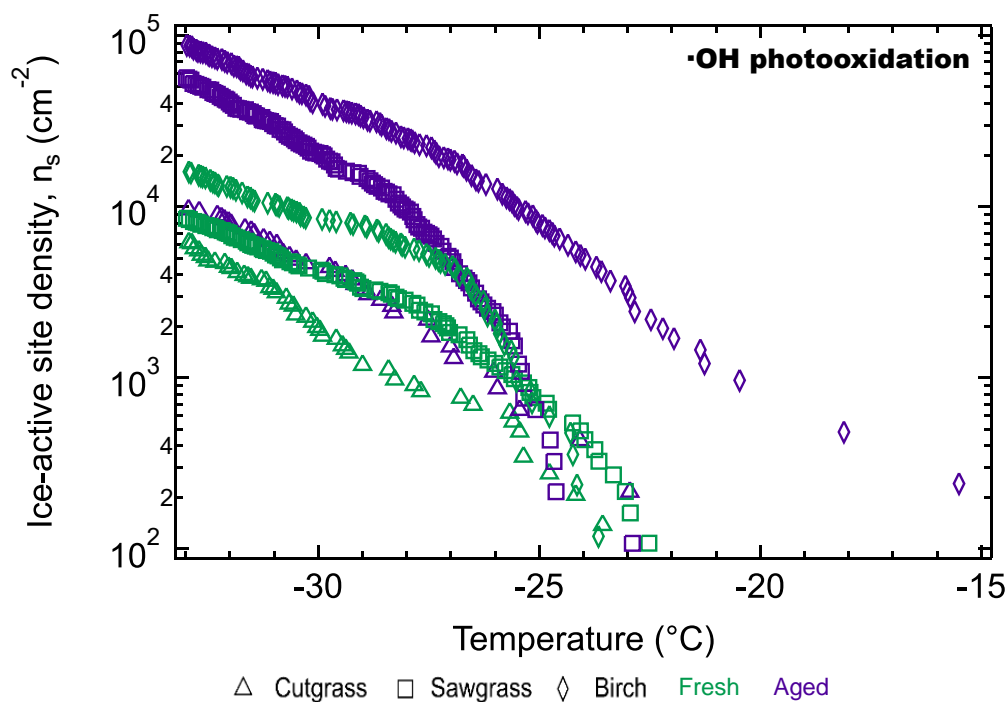
Figure A2-2. Ice-active surface site density (n_s) temperature spectra for additional BBA ·OH photooxidation aging experiments. The experiments here are ·OH photooxidation of biomass-burning aerosol produced from combustion of cutgrass, sawgrass, or birch. Fresh BBA samples (prior to external perturbation) are shown in green and aged samples following several hours of chamber photooxidative aging are shown in purple. ·OH photooxidation tended to increase the INA across most if not all temperatures, similar to the results shown in Figure 2-1. The birch experiment shown here was the only BBA produced from wood (as opposed to grass) combustion that showed appreciable INA and an increase in INA after aging. See Fig. A2-4 for additional data and discussion on wood BBA.
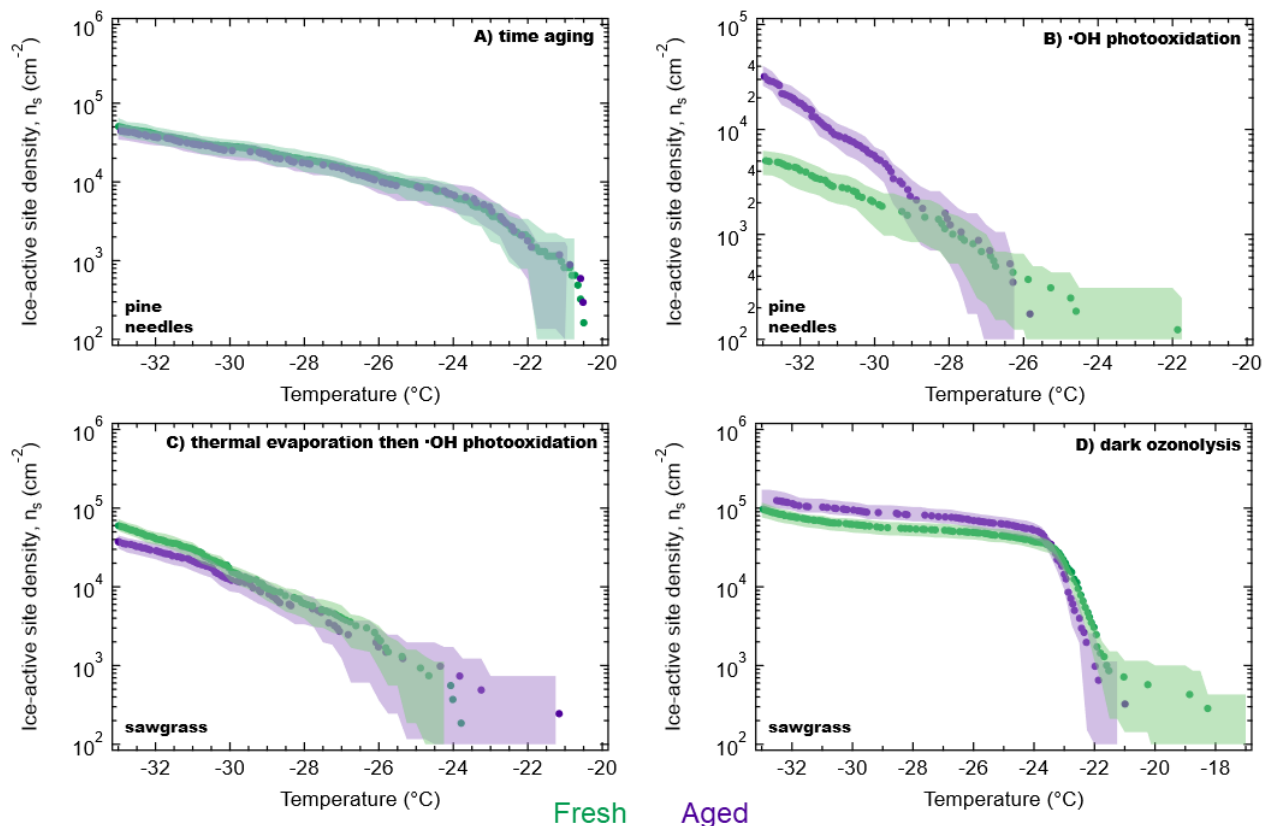
Figure A2-3. Selected n_s spectra from Figure 2-1 with 95% confidence intervals shown. One experiment for each aging type (fuel indicated within each panel) was chosen based off their fresh and aged ice-active site densities being the most similar. Shaded 95% confidence intervals were calculated following the Monte Carlo method presented by Vali (60) as described above. This emphasizes that unless the INA of the fresh and aged are extremely similar, we can confidently state that the observed increases in INA are statistically significant and beyond measurement uncertainty or variability. For **A)** time aging here there is no significant difference between fresh and aged, but in all other experiments in Fig. 2-1, the fresh and aged BBA are significantly different at temperatures < −23.5 °C. For **B)** ·OH photooxidation experiments, the aged ponderosa pine needle BBA is significantly greater than the fresh BBA only at temperatures < −29.6 °C, while the fresh & aged cutgrass and sawgrass experiments in Fig. 2-1 are different < −27.2 °C and < −24.2 °C, respectively. The **C)** thermal evaporation then ·OH photooxidation sawgrass experiment shown here does not have a statistically significant difference between the fresh and aged aerosol, but for the cutgrass experiment in Fig. 2-1, fresh and aged BBA are different between −23 °C and −31 °C. The **D)** dark ozonolysis sawgrass experiment has no significant difference between fresh and aged BBA, while the cutgrass experiment in Fig. 2-1 has a significant decrease in INA after aging across all temperatures. These data show that at temperatures relevant to mixed-phased clouds, there are statistically significant increases in INA after dilution, evaporation, and photooxidative aging, and no increase or even a statistically significant decrease in INA following aging that involved substantial SOA production.

47

Figure A2-4. Frozen fraction temperature spectra for BBA from two wood fuels. Ice nucleation analysis was performed by a traditional droplet-on-substrate technique; method details are described by Polen et al. (2016, 2018). BBA from birch wood **(A)** and fatwood **(B)** was subjected to ·OH photooxidation without additional NO_x, and no increase in INA was observed. Average background freezing temperature spectrum for filtered water shown as gray line; all BBA sample data for birch and fatwood lay within the water background freezing spectrum. Based off of previous work, EDX revealed less mineral formation in BBA produced from woods compared to tall grasses, with slightly more minerals present in birch BBA compared to fatwood BBA (Jahn et al., 2020). The combustion of these woods also produced the most black carbon (BC) in the aerosol compared to other fuels studied – birch BBA was 65% BC by mass and fatwood was 86% BC as measured by the SP-AMS. The reasoning behind the lack of increase in INA with aging observed here is consistent with our previous discussion. For wood fuels, there are few mineral-based ice-active sites present in even the fresh BBA, so any evaporation of organic carbon coatings – that revealed the mineral-based ice-active sites in BBA produced from grass combustion – made no difference in the INA of aged BBA produced from the combustion of these woods. These results further emphasize that black carbon from biomass combustion cannot explain the ice activity of BBA, or how it responds to aging.
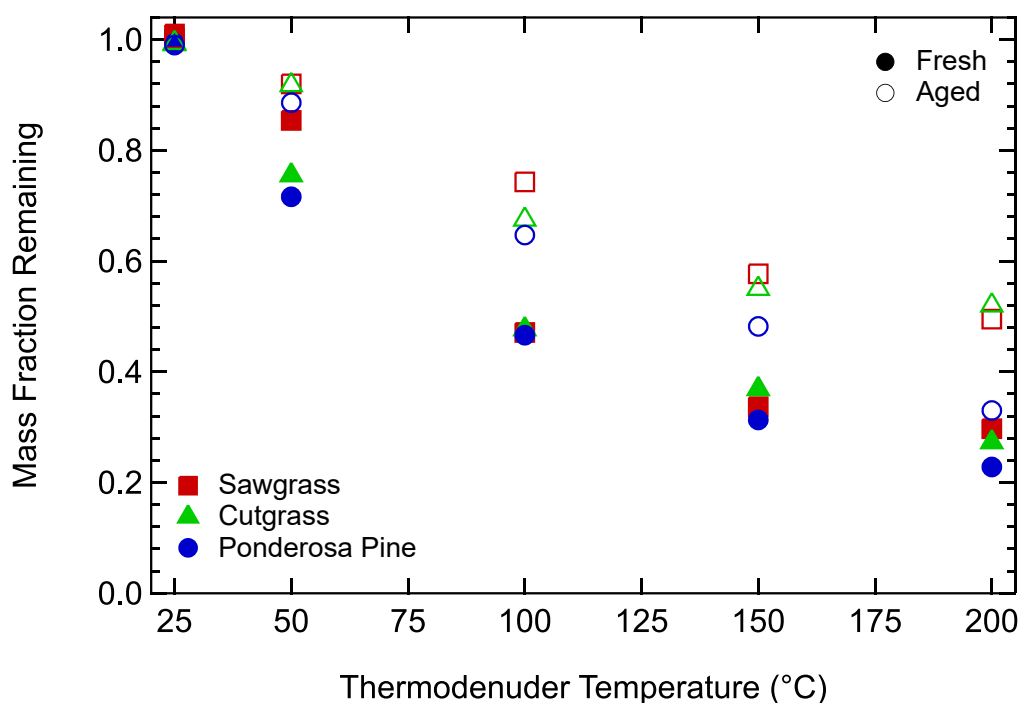
Figure A2-5. Effects of ·OH photooxidative aging on the volatility of organic aerosol (OA) in BBA. Trends in aerosol volatility are demonstrated based on the mass fraction of OA remaining after being subjected to thermal desorption, plotted as a function of thermodenuder (TD) temperature. The OA mass fraction remaining was calculated from the SP-AMS in laser-off mode by dividing the OA concentration following the TD by the OA concentration following an unheated bypass line. Filled symbols indicate fresh BBA, while hollow symbols indicate ·OH-aged BBA. For each of these fuels, the mass fraction remaining after aging is less than that for the fresh aerosol particles, indicating that aged aerosol is less volatile. This complements our understanding of how organic aerosol aging reveals ice-active sites present in the BBA. The TD methodology used here is further described by Cain & Pandis (Cain and Pandis, 2017). All SP-AMS data analysis was completed in the Igor software packages SQUIRREL (version 1.62A) and PIKA (version 1.22A).
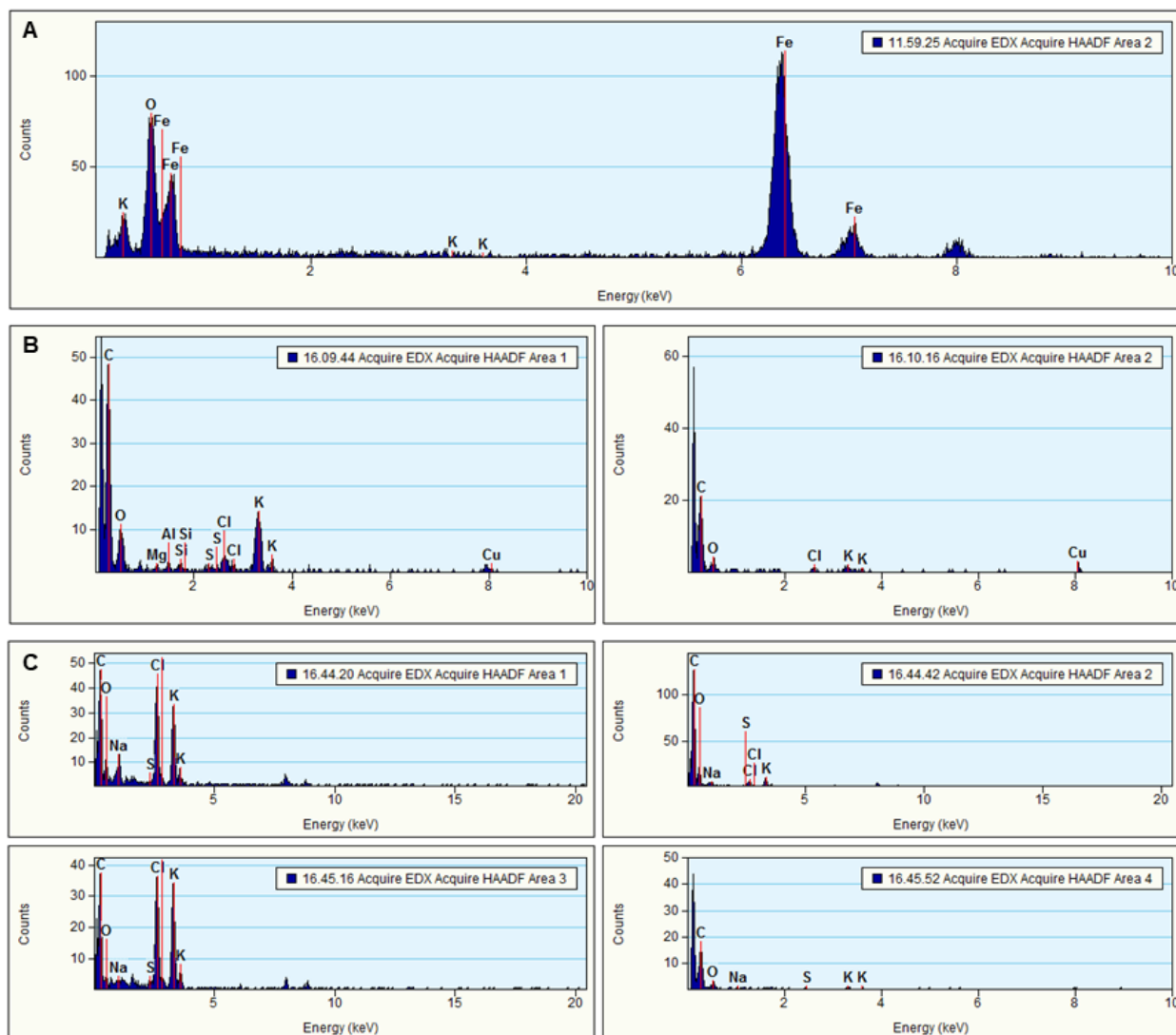
Figure A2-6. Energy dispersive X-ray spectroscopy (EDX) spectra from TEM images of BBA particles displayed in Figure 2-3. The ordering of the particle microscopy images and spectra here are the same as in Figure 2-3, and the area numbers within the legend of each spectrum here corresponds to the numbered regions in Fig. 2-3. Particle **A)** EDX spectrum shows the iron-based mineral region. Particle **B)** EDX spectra show region 1 composed of KCl; Al, Mg, and Si-containing minerals; and carbonaceous material, with additional KCl in region 2. Particle **C)** EDX spectra show chloride salts in regions 1 & 3, and carbonaceous material in regions 2 & 4 on the outer edges of the particle. These spectra, as well as previous work on the same biomass fuels, show organic aerosol coating inorganic/mineral regions, supporting our new framework suggesting that OA evaporation exposes the ice-active mineral surface sites in BBA (Jahn et al., 2020).
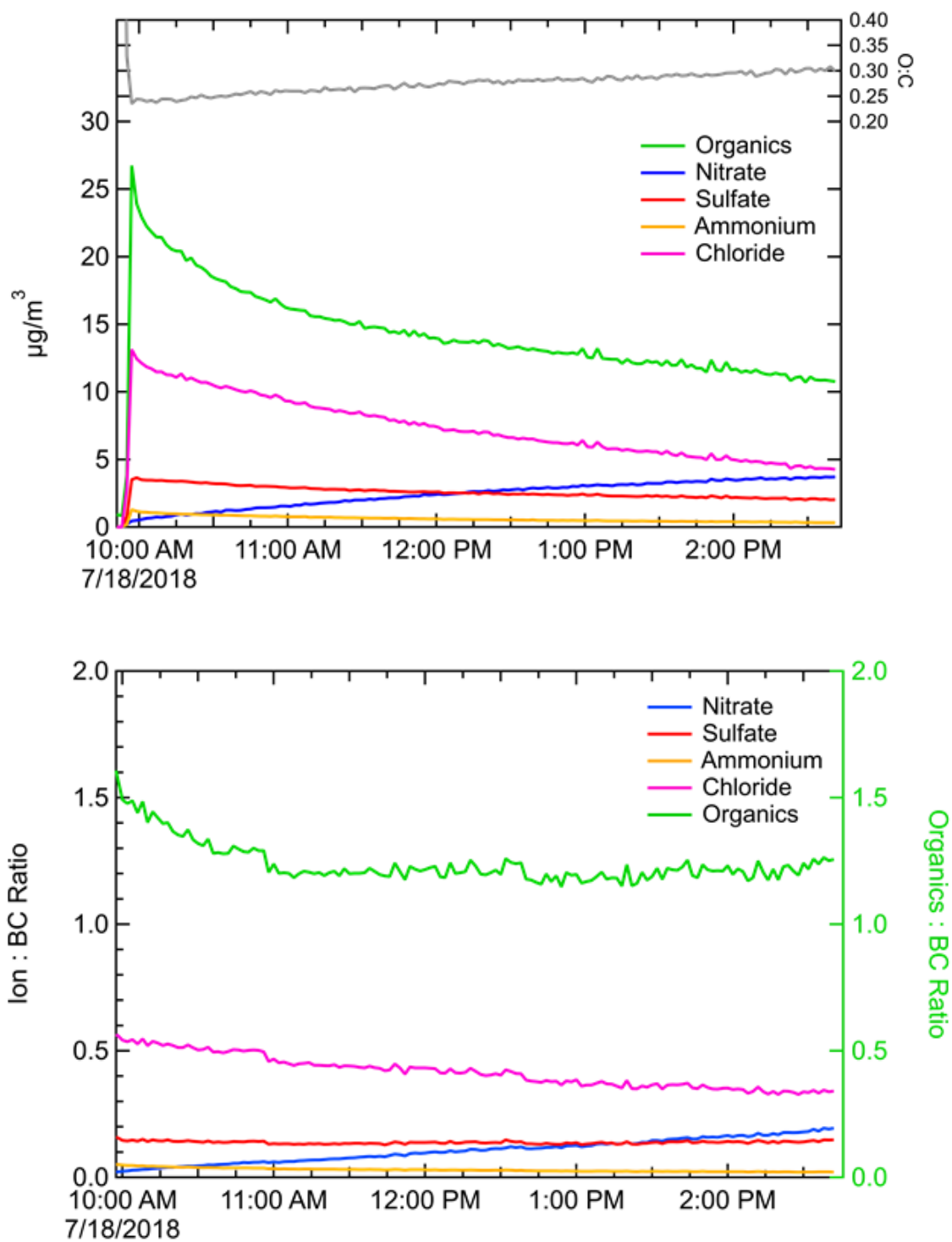
Figure A2-7. High-resolution AMS chemical composition of cutgrass time-aging experiment. Top panel is absolute concentrations of different species and O:C. Bottom panel is ratio of each species to black carbon.
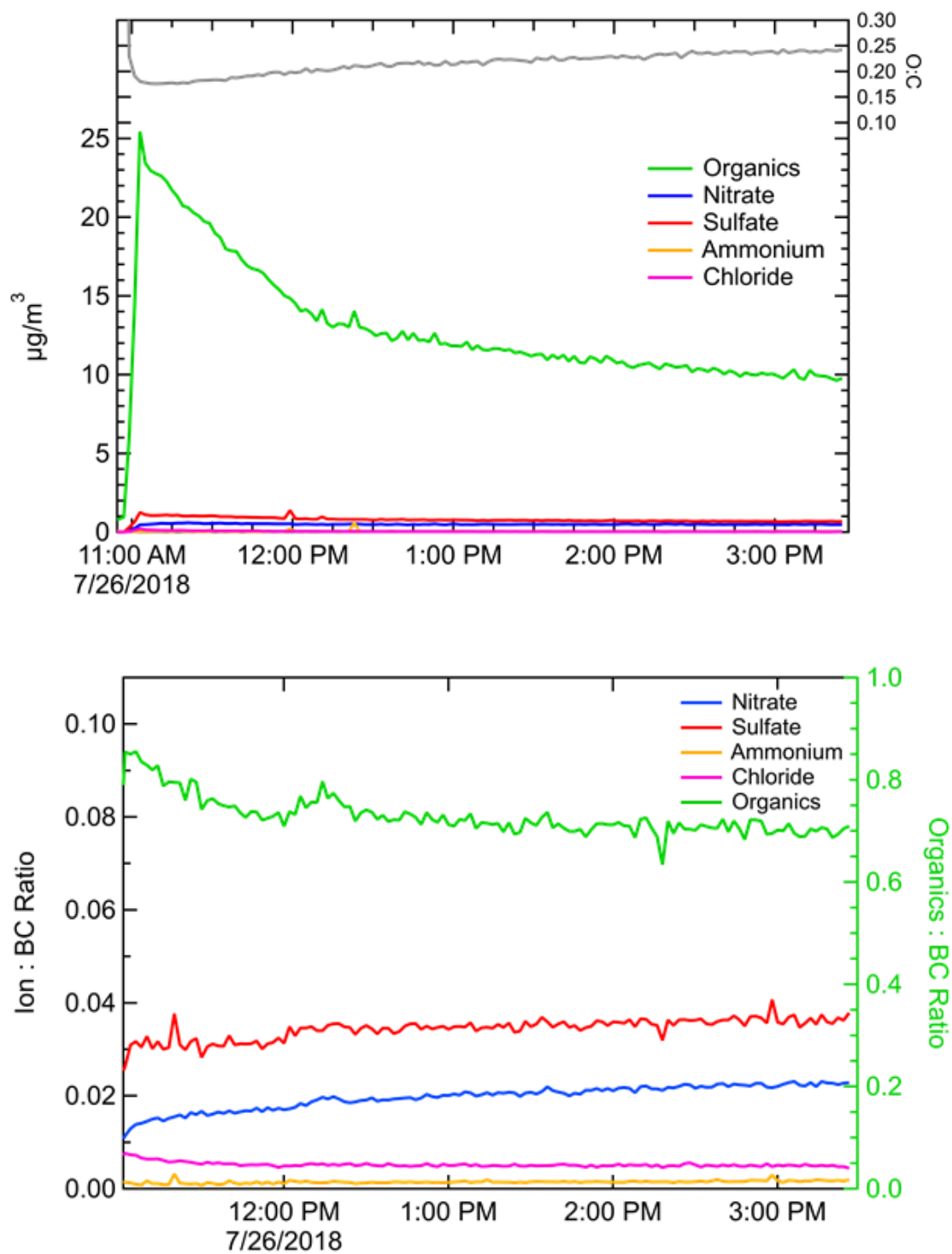
Figure A2-8. High-resolution AMS chemical composition of ponderosa pine needles time-aging experiment. Top panel is absolute concentrations of different species and O:C. Bottom panel is ratio of each species to black carbon.
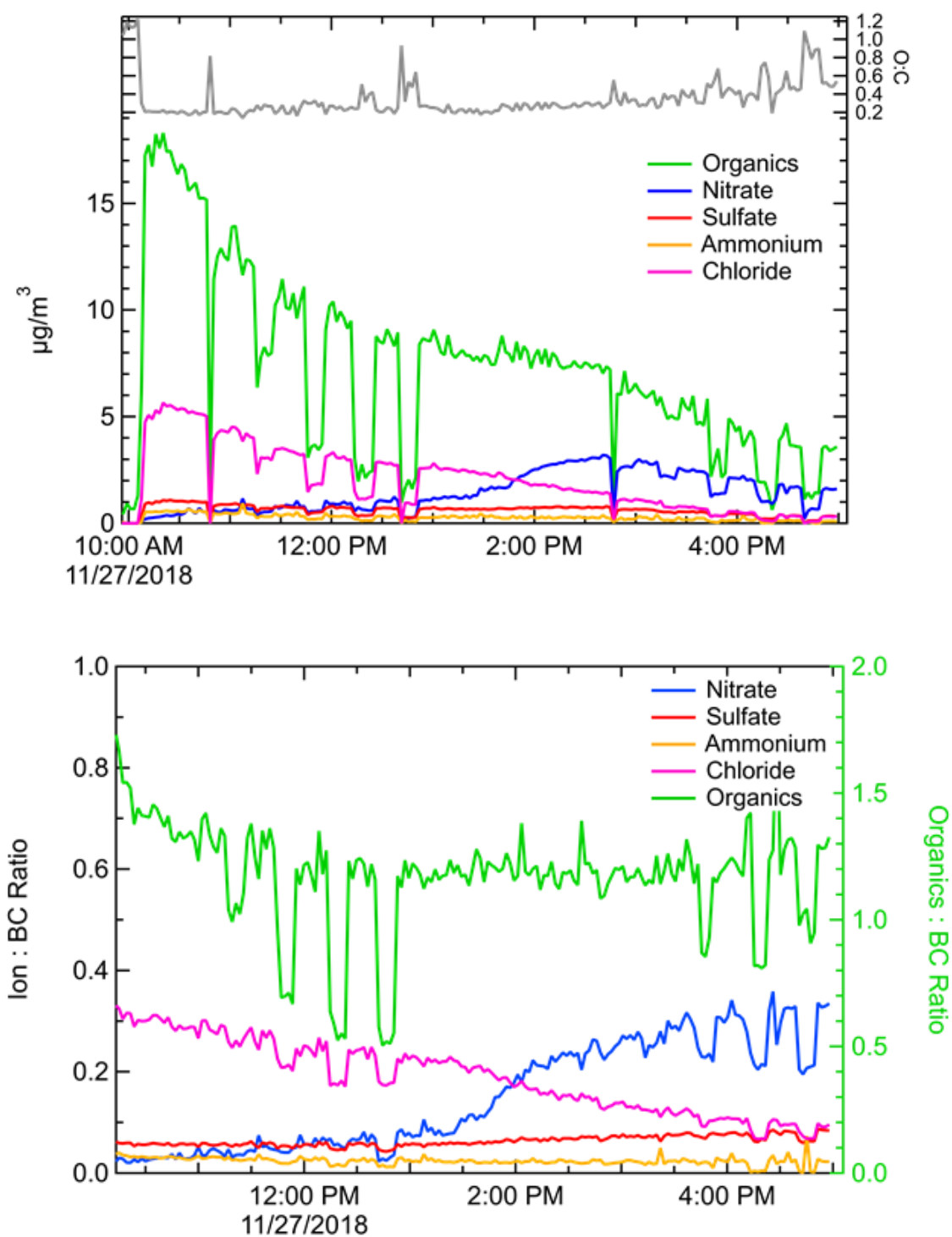
Figure A2-9. High-resolution AMS chemical composition of cutgrass OH-aging experiment. Top panel is absolute concentrations of different species and O:C. Bottom panel is ratio of each species to black carbon.
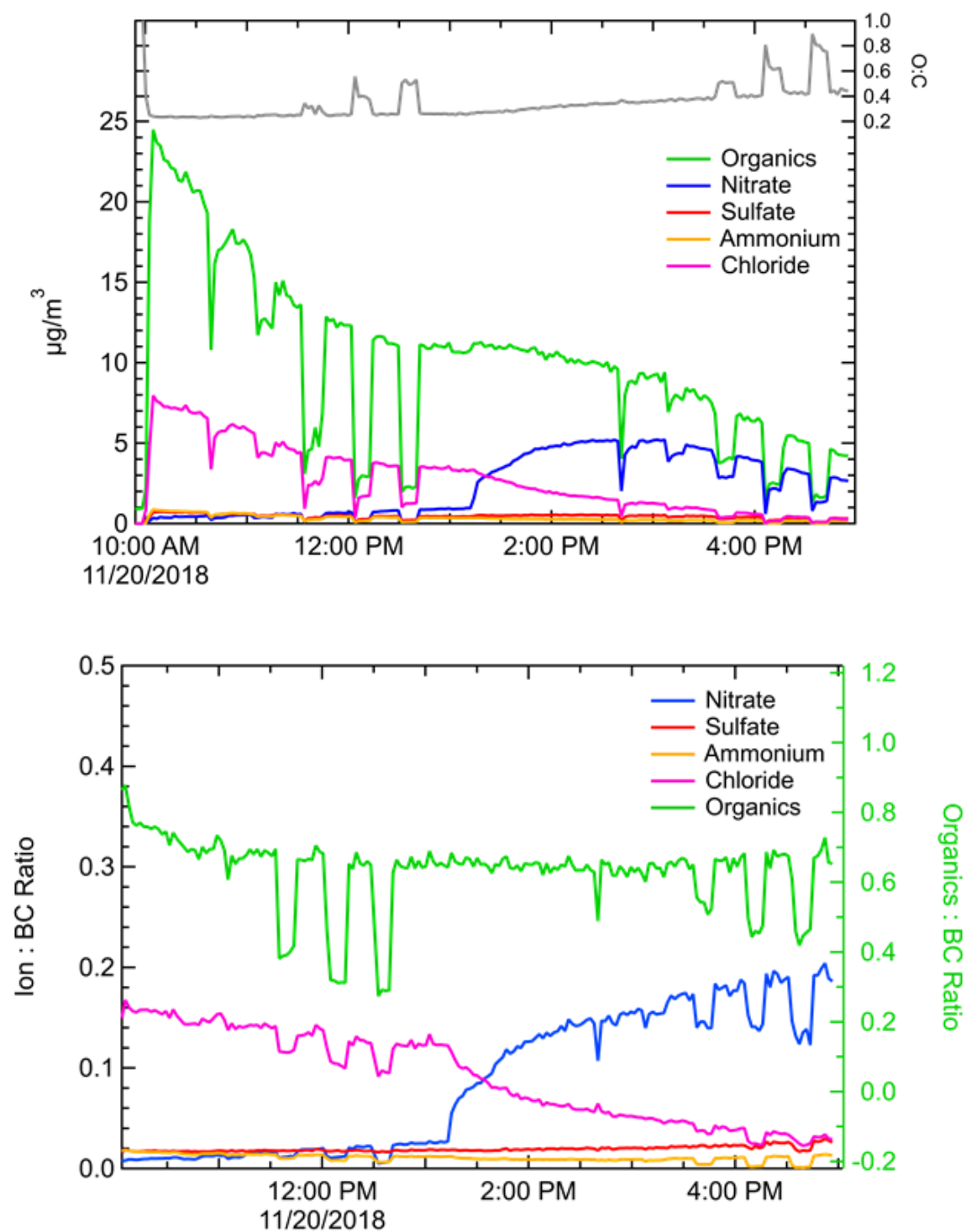
Figure A2-10. High-resolution AMS chemical composition of sawgrass OH-aging experiment. Top panel is absolute concentrations of different species and O:C. Bottom panel is ratio of each species to black carbon.
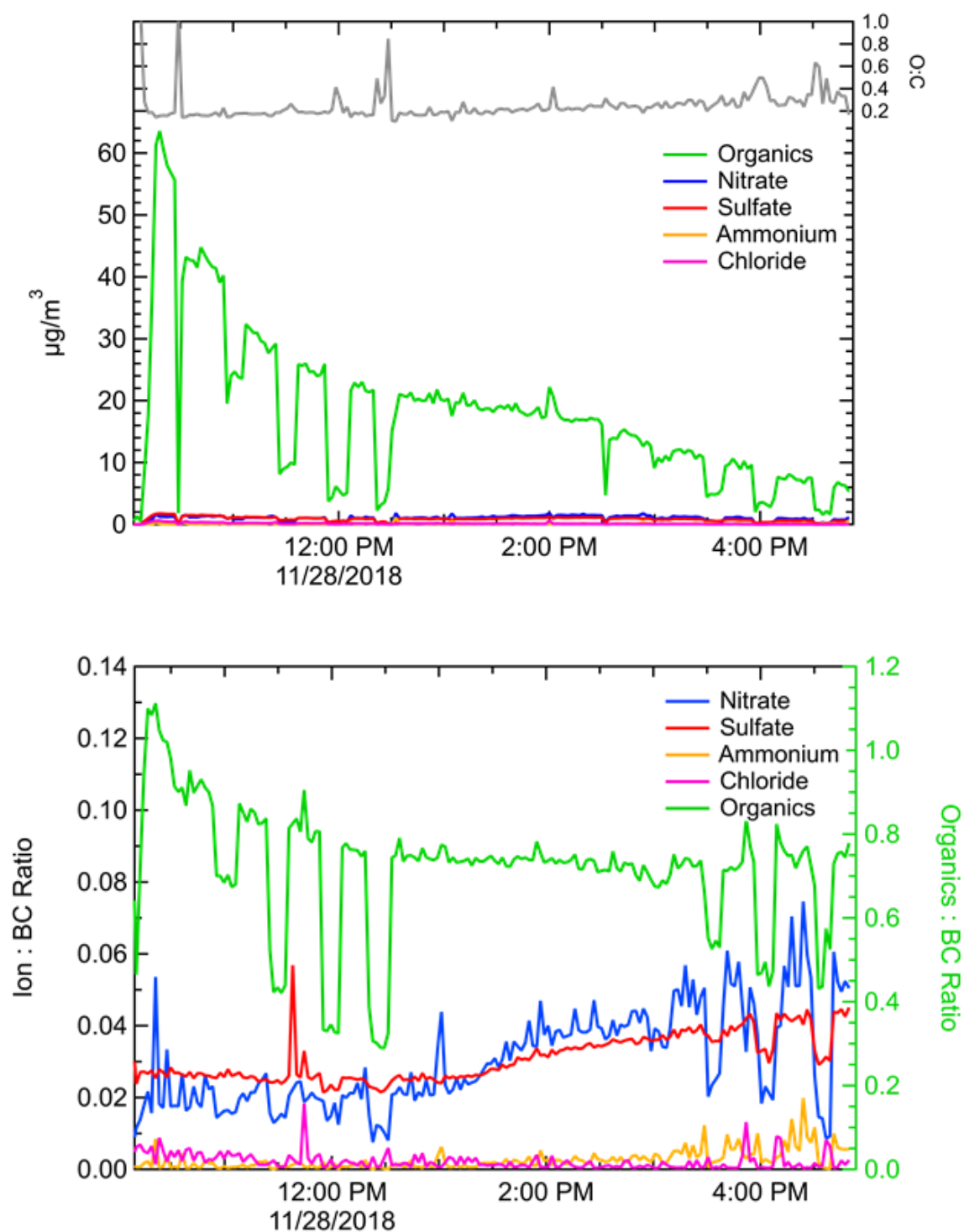
Figure A2-11. High-resolution AMS chemical composition of ponderosa pine needles OH-aging experiment. Top panel is absolute concentrations of different species and O:C. Bottom panel is ratio of each species to black carbon.
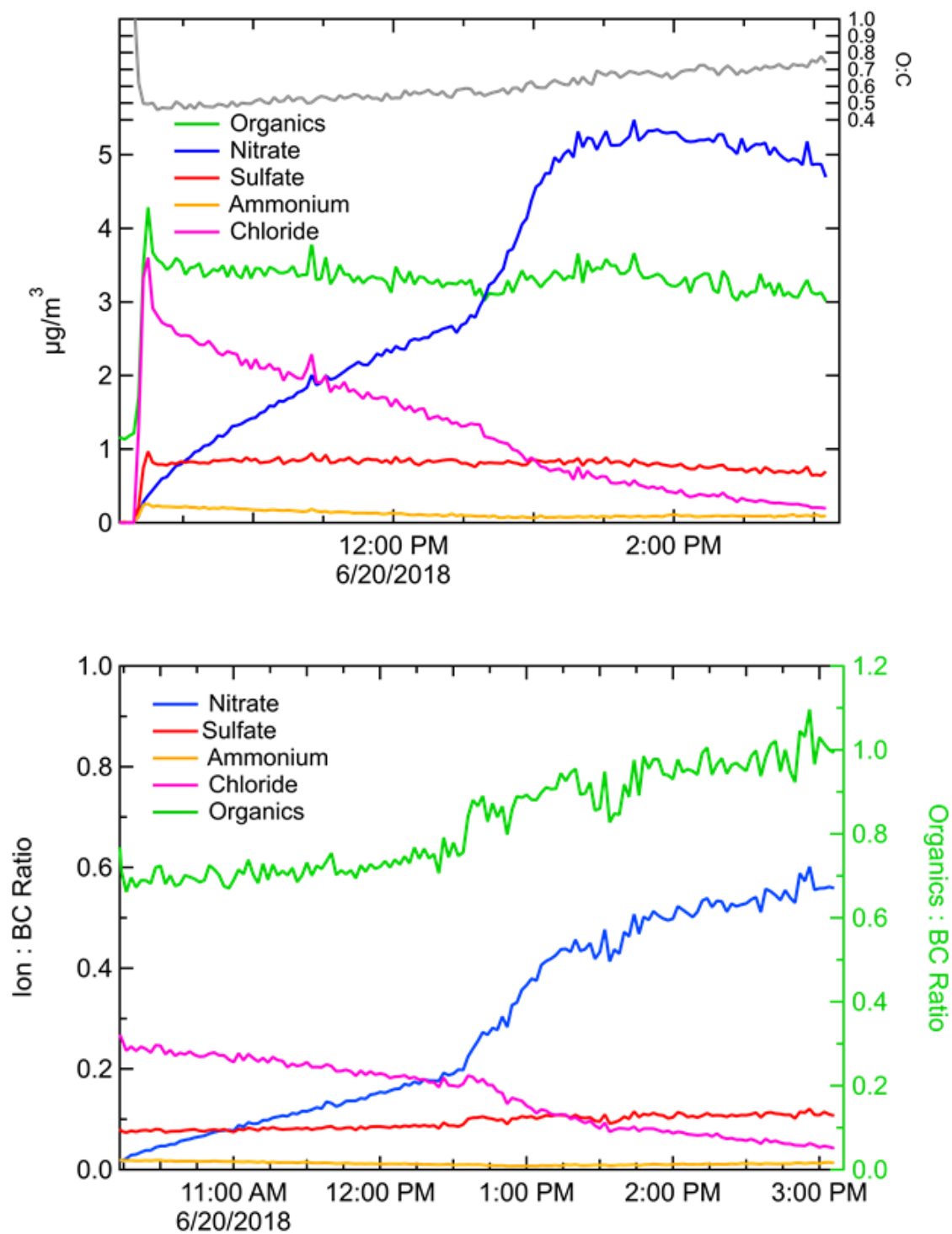
Figure A2-12. High-resolution AMS chemical composition of cutgrass, thermally denuded then OH-aging experiment. Top panel is absolute concentrations of different species and O:C. Bottom panel is ratio of each species to black carbon.
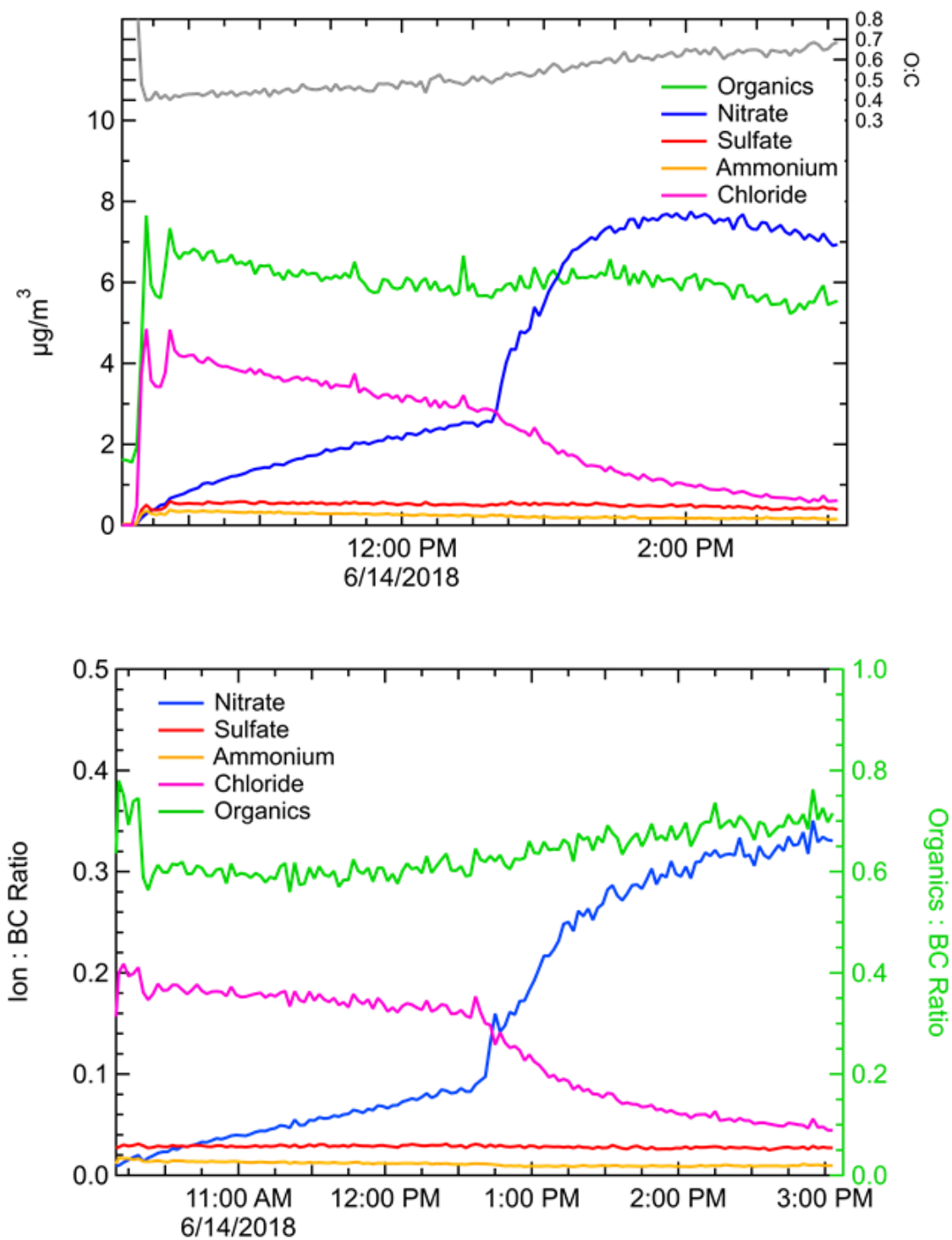
Figure A2-13. High-resolution AMS chemical composition of sawgrass, thermally denuded then OH-aging experiment. Top panel is absolute concentrations of different species and O:C. Bottom panel is ratio of each species to black carbon.
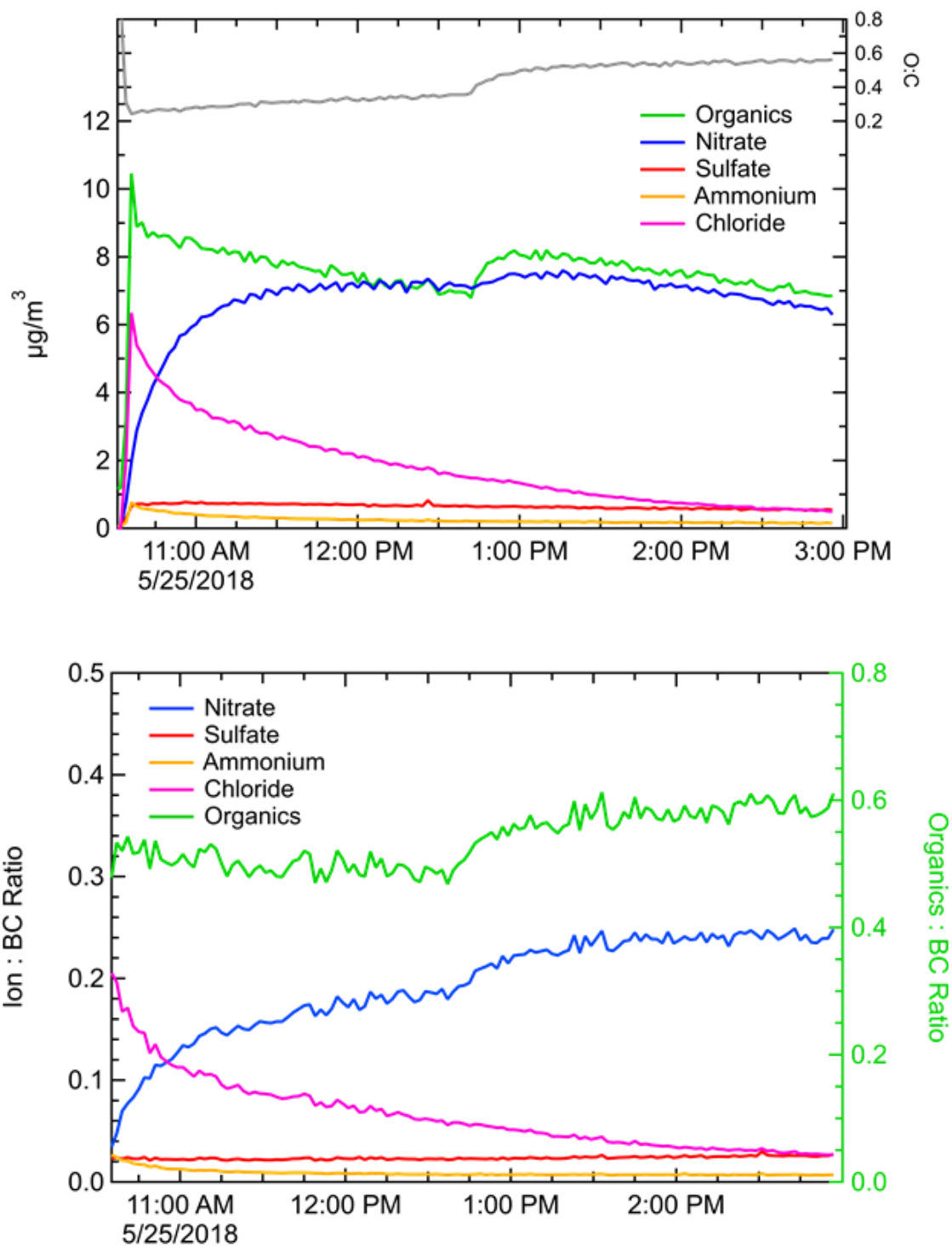
Figure A2-14. High-resolution AMS chemical composition of sawgrass ozonolysis experiment. Top panel is absolute concentrations of different species and O:C. Bottom panel is ratio of each species to black carbon.
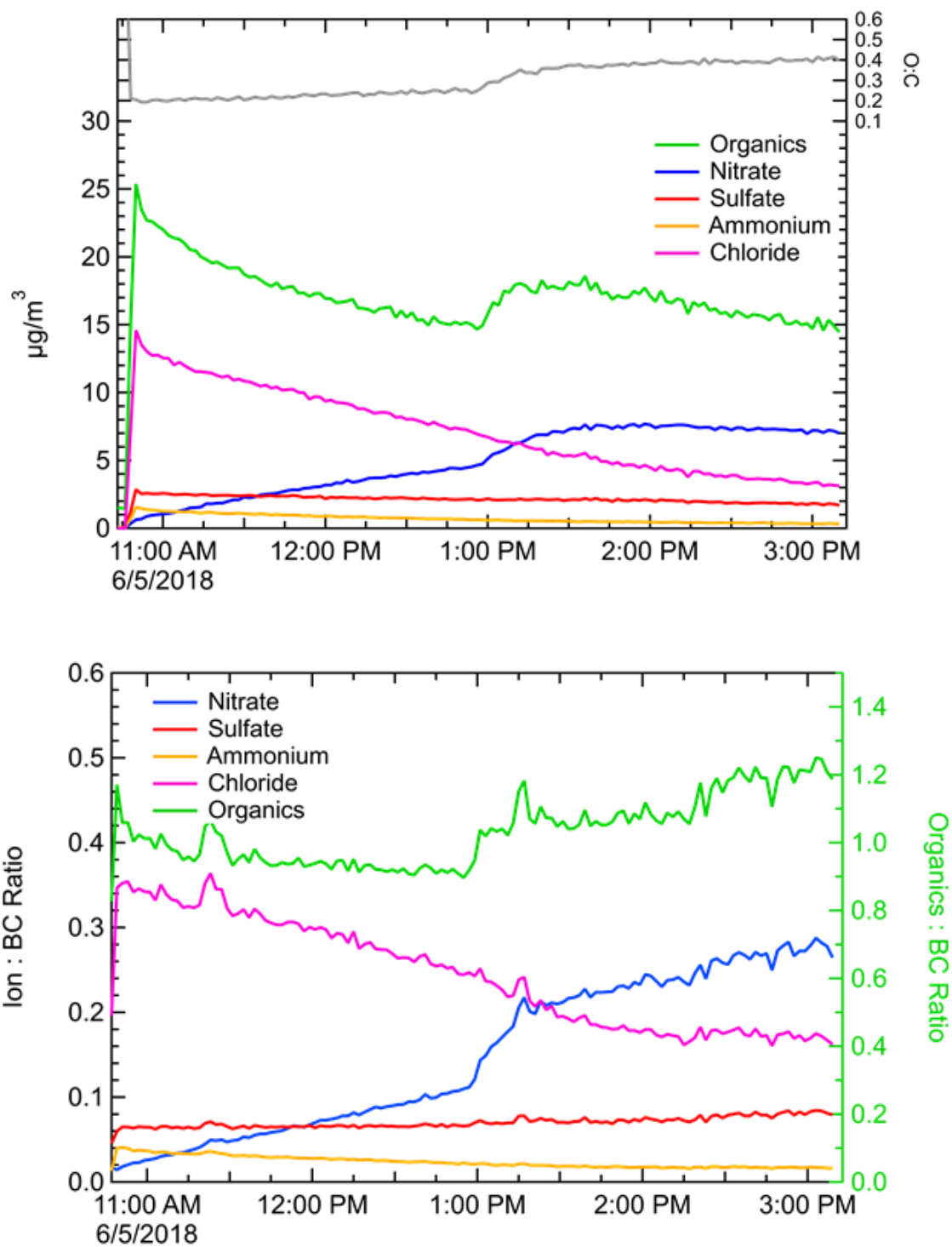
Figure A2-15. High-resolution AMS chemical composition of cutgrass ozonolysis experiment. Top panel is absolute concentrations of different species and O:C. Bottom panel is ratio of each species to black carbon.

2.8   References

Adachi, K., Sedlacek, A. J., Kleinman, L., Springston, S. R., Wang, J., Chand, D., Hubbe, J. M., Shilling, J. E., Onasch, T. B., Kinase, T., Sakata, K., Takahashi, Y. and Buseck, P. R.: Spherical tarball particles form through rapid chemical and physical changes of organic matter in biomass-burning smoke, Proc. Natl. Acad. Sci. U. S. A., 116(39), 19336–19341, doi:10.1073/pnas.1900129116, 2019.

Ahern, A. T., Goldberger, L., Jahl, L., Thornton, J. and Sullivan, R. C.: Production of N2O5 and ClNO2 through Nocturnal Processing of Biomass-Burning Aerosol, Environ. Sci. Technol., 52(2), 550–559, doi:10.1021/acs.est.7b04386, 2018.

Ahern, A. T., Robinson, E. S., Tkacik, D. S., Saleh, R., Hatch, L. E., Barsanti, K. C., Stockwell, C. E., Yokelson, R. J., Presto, A. A., Robinson, A. L., Sullivan, R. C. and Donahue, N. M.: Production of Secondary Organic Aerosol During Aging of Biomass Burning Smoke From Fresh Fuels and Its Relationship to VOC Precursors, J. Geophys. Res. Atmos., 124(6), 3583–3606, doi:10.1029/2018JD029068, 2019.

Bian, Q., May, A. A., Kreidenweis, S. M. and Pierce, J. R.: Investigation of particle and vapor wall-loss effects on controlled wood-smoke smog-chamber experiments, Atmos. Chem. Phys, 15, 11027–11045, doi:10.5194/acp-15-11027-2015, 2015.

Bian, Q., Jathar, S. H., Kodros, J. K., Barsanti, K. C., Hatch, L. E., May, A. A., Kreidenweis, S. M. and Pierce, J. R.: Secondary organic aerosol formation in biomass-burning plumes: theoretical analysis of lab studies and ambient plumes, Atmos. Chem. Phys, 17, 5459–5475, doi:10.5194/acp-17-5459-2017, 2017.

Bond, T. C., Doherty, S. J., Fahey, D. W., Forster, P. M., Berntsen, T., DeAngelo, B. J., Flanner, M. G., Ghan, S., Kärcher, B., Koch, D., Kinne, S., Kondo, Y., Quinn, P. K., Sarofim, M. C., Schultz, M. G., Schulz, M., Venkataraman, C., Zhang, H., Zhang, S., Bellouin, N., Guttikunda, S. K., Hopke, P. K., Jacobson, M. Z., Kaiser, J. W., Klimont, Z., Lohmann, U., Schwarz, J. P., Shindell, D., Storelvmo, T., Warren, S. G. and Zender, C. S.: Bounding the role of black carbon in the climate system: A scientific assessment, J. Geophys. Res. Atmos., 118(11), 5380–5552, doi:10.1002/jgrd.50171, 2013.

Brubaker, T., Polen, M., Cheng, P., Ekambaram, V., Somers, J., Anna, S. L. and Sullivan, R. C.: Development and characterization of a "store and create" microfluidic device to determine the heterogeneous freezing properties of ice nucleating particles, Aerosol Sci. Technol., 54(1), 79–93, doi:10.1080/02786826.2019.1679349, 2020.

Cain, K. P. and Pandis, S. N.: A technique for the measurement of organic aerosol hygroscopicity, oxidation level, and volatility distributions, Atmos. Meas. Tech, 10, 4865–4876, doi:10.5194/amt-10-4865-2017, 2017.

Chou, C., Kanji, Z. A., Stetzer, O., Tritscher, T., Chirico, R., Heringa, M. F., Weingartner, E., Prévôt, A. S. H., Baltensperger, U. and Lohmann, U.: Effect of photochemical ageing on the ice nucleation properties of diesel and wood burning particles, Atmos. Chem. Phys., 13(2), 761–772, doi:10.5194/acp-13-761-2013, 2013.

Cziczo, D. J., Froyd, K. D., Gallavardin, S. J., Moehler, O., Benz, S., Saathoff, H. and Murphy, D. M.: Deactivation of ice nuclei due to atmospherically relevant surface coatings, Environ. Res. Lett., 4(4), doi:10.1088/1748-9326/4/4/044013, 2009.

DeMott, P. J., Petters, M. D., Prenni, A. J., Carrico, C. M., Kreidenweis, S. M., Collett, J. L. and Moosmüller, H.: Ice nucleation behavior of biomass combustion particles at cirrus temperatures, J. Geophys. Res. Atmos., 114(16), D16205, doi:10.1029/2009JD012036, 2009.

DeMott, P. J., Prenni, A. J., Liu, X., Kreidenweis, S. M., Petters, M. D., Twohy, C. H., Richardson, M. S., Eidhammer, T. and Rogers, D. C.: Predicting global atmospheric ice nuclei distributions and their impacts on climate, Proc. Natl. Acad. Sci., 107(25), 11217–11222, doi:10.1073/pnas.0910818107, 2010.

Donahue, N. M., Epstein, S. A., Pandis, S. N. and Robinson, A. L.: A two-dimensional volatility basis set: 1. organic-aerosol mixing thermodynamics, Atmos. Chem. Phys., 11(7), 3303–3318, doi:10.5194/acp-11-3303-2011, 2011.

Engelhart, G. J., Hennigan, C. J., Miracolo, M. A., Robinson, A. L. and Pandis, S. N.: Cloud condensation nuclei activity of fresh primary and aged biomass burning aerosol, Atmos. Chem. Phys., 12(15), 7285–7293, doi:10.5194/acp-12-7285-2012, 2012.

Fan, J., Wang, Y., Rosenfeld, D. and Liu, X.: Review of aerosol-cloud interactions: Mechanisms, significance, and challenges, J. Atmos. Sci., 73(11), 4221–4252, doi:10.1175/JAS-D-16-0037.1, 2016.

Fromm, M., Peterson, D. and Di Girolamo, L.: The primary convective pathway for observed wildfire emissions in the upper troposphere and lower stratosphere: a targeted reinterpretation, J. Geophys. Res. Atmos., 2019JD031006, doi:10.1029/2019JD031006, 2019.

Garofalo, L. A., Pothier, M. A., Levin, E. J. T., Campos, T., Kreidenweis, S. M. and Farmer, D. K.: Emission and Evolution of Submicron Organic Aerosol in Smoke from Wildfires in the Western United States, ACS Earth Sp. Chem., 3(7), 1237–1247, doi:10.1021/acsearthspacechem.9b00125, 2019.

Goldberger, L. A., Jahl, L. G., Thornton, J. A. and Sullivan, R. C.: N2O5 reactive uptake kinetics and chlorine activation on authentic biomass-burning aerosol, Environ. Sci. Process. Impacts, 21(10), 1684–1698, doi:10.1039/c9em00330d, 2019.

Gorkowski, K., Donahue, N. M. and Sullivan, R. C.: Aerosol Optical Tweezers Constrain the Morphology Evolution of Liquid-Liquid Phase-Separated Atmospheric Particles, Chem, 6(1), 204–220, doi:10.1016/j.chempr.2019.10.018, 2020.

Hennigan, C. J., Miracolo, M. A., Engelhart, G. J., May, A. A., Presto, A. A., Lee, T., Sullivan, A. P., McMeeking, G. R., Coe, H., Wold, C. E., Hao, W.-M., Gilman, J. B., Kuster, W. C., De Gouw, J. A., Schichtel, B. A., Collett, J. L., Kreidenweis, S. M. and Robinson, A. L.: Chemical and physical transformations of organic aerosol from the photo-oxidation of open biomass burning emissions in an environmental chamber, Atmos. Chem. Phys. Atmos. Chem. Phys., 11, 7669–7686, doi:10.5194/acp-11-7669-2011, 2011.

Hodshire, A. L., Akherati, A., Alvarado, M. J., Brown-Steiner, B., Jathar, S. H., Jimenez, J. L., Kreidenweis, S. M., Lonsdale, C. R., Onasch, T. B., Ortega, A. M. and Pierce, J. R.: Aging Effects on Biomass Burning Aerosol Mass and Composition: A Critical Review of Field and Laboratory Studies, Environ. Sci. Technol., 53(17), 10007–10022, doi:10.1021/acs.est.9b02588, 2019a.

Hodshire, A. L., Bian, Q., Ramnarine, E., Lonsdale, C. R., Alvarado, M. J., Kreidenweis, S. M., Jathar, S. H. and Pierce, J. R.: More Than Emissions and Chemistry: Fire Size, Dilution, and Background Aerosol Also Greatly Influence Near-Field Biomass Burning Aerosol Aging, J. Geophys. Res. Atmos., 124(10), 5589–5611, doi:10.1029/2018JD029674, 2019b.

Jahn, L., Polen, M., Jahl, L. G., Brubaker, T., Somers, J. and Sullivan, R. C.: Biomass combustion produces ice-active minerals in biomass-burning aerosol and bottom ash, Proc. Natl. Acad. Sci., doi/10.1073/pnas.1922128117, 2020.

Kanji, Z. A., Ladino, L. A., Wex, H., Boose, Y., Burkert-Kohn, M., Cziczo, D. J. and Krämer, M.: Overview of Ice Nucleating Particles, Meteorol. Monogr., 58, 1.1-1.33, doi:10.1175/amsmonographs-d-16-0006.1, 2017.

Kanji, Z. A., Sullivan, R. C., Niemand, M., Demott, P. J., Prenni, A. J., Chou, C., Saathoff, H. and Möhler, O.: Heterogeneous ice nucleation properties of natural desert dust particles coated with a surrogate of secondary organic aerosol, Atmos. Chem. Phys, 19, 5091–5110, doi:10.5194/acp-19-5091-2019, 2019.

Koehler, K. A., DeMott, P. J., Kreidenweis, S. M., Popovicheva, O. B., Petters, M. D., Carrico, C. M., Kireeva, E. D., Khokhlova, T. D. and Shonija, N. K.: Cloud condensation nuclei and ice nucleation activity of hydrophobic and hydrophilic soot particles, Phys. Chem. Chem. Phys., 11(36), 7906, doi:10.1039/b905334b, 2009.

Kroll, J. H., Donahue, N. M., Jimenez, J. L., Kessler, S. H., Canagaratna, M. R., Wilson, K. R., Altieri, K. E., Mazzoleni, L. R., Wozniak, A. S., Bluhm, H., Mysak, E. R., Smith, J. D., Kolb, C. E. and Worsnop, D. R.: Carbon oxidation state as a metric for describing the chemistry of atmospheric organic aerosol, Nat. Chem., 3(2), 133–139, doi:10.1038/nchem.948, 2011.

Kulkarni, G. R., Sanders, C., Zhang, K., Liu, X. and Zhao, C.: Ice nucleation of bare and sulfuric acid-coated mineral dust particles and implication for cloud properties, J. Geophys. Res. Atmos., 119(16), 9993–10011, doi:10.1002/2014JD021567, 2014.

Lathem, T. L., Beyersdorf, A. J., Thornhill, K. L., Winstead, E. L., Cubison, M. J., Hecobian, A., Jimenez, J. L., Weber, R. J., Anderson, B. E. and Nenes, A.: Analysis of CCN activity of Arctic aerosol and Canadian biomass burning during summer 2008, Atmos. Chem. Phys., 13(5), 2735–2756, doi:10.5194/acp-13-2735-2013, 2013.

Levin, E. J. T., McMeeking, G. R., DeMott, P. J., McCluskey, C. S., Carrico, C. M., Nakao, S., Jayarathne, T., Stone, E. A., Stockwell, C. E., Yokelson, R. J. and Kreidenweis, S. M.: Ice-nucleating particle emissions from biomass combustion and the potential importance of soot aerosol, J. Geophys. Res. Atmos., 121(10), 5888–5903, doi:10.1002/2016JD024879, 2016.

Li, J., Pósfai, M., Hobbs, P. V. and Buseck, P. R.: Individual aerosol particles from biomass burning in southern Africa: 2, Compositions and aging of inorganic particles, J. Geophys. Res. Atmos., 108(D13), n/a-n/a, doi:10.1029/2002JD002310, 2003.

Lim, C. Y., Hagan, D. H., Coggon, M. M., Koss, A. R., Sekimoto, K., De Gouw, J., Warneke, C., Cappa, C. D. and Kroll, J. H.: Secondary organic aerosol formation from the laboratory oxidation of biomass burning emissions, Atmos. Chem. Phys, 19, 12797–12809, doi:10.5194/acp-19-12797-2019, 2019.

Lupi, L. and Molinero, V.: Does hydrophilicity of carbon particles improve their ice nucleation ability?, J. Phys. Chem. A, 118(35), 7330–7337, doi:10.1021/jp4118375, 2014.

Mahrt, F., Marcolli, C., David, R. O., Grönquist, P., Meier, E. J. B., Lohmann, U. and Kanji, Z. A.: Ice nucleation abilities of soot particles determined with the Horizontal Ice Nucleation Chamber, Atmos. Chem. Phys, 18, 13363–13392, doi:10.5194/acp-18-13363-2018, 2018.

Mahrt, F., Alpert, P. A., Dou, J., Grönquist, P., Arroyo, P. C., Ammann, M., Lohmann, U. and Kanji, Z. A.: Aging induced changes in ice nucleation activity of combustion aerosol as determined

by near edge X-ray absorption fine structure (NEXAFS) spectroscopy, Environ. Sci. Process. Impacts, 22(4), 895–907, doi:10.1039/c9em00525k, 2020a.

Mahrt, F., Kilchhofer, K., Marcolli, C., Grönquist, P., David, R. O., Rösch, M., Lohmann, U. and Kanji, Z. A.: The Impact of Cloud Processing on the Ice Nucleation Abilities of Soot Particles at Cirrus Temperatures, J. Geophys. Res. Atmos., 125(3), doi:10.1029/2019JD030922, 2020b.

McClure, C. D. and Jaffe, D. A.: US particulate matter air quality improves except in wildfire-prone areas, Proc. Natl. Acad. Sci. U. S. A., 115(31), 7901–7906, doi:10.1073/pnas.1804353115, 2018.

McCluskey, C. S., DeMott, P. J., Prenni, A. J., Levin, E. J. T., McMeeking, G. R., Sullivan, A. P., Hill, T. C. J., Nakao, S., Carrico, C. M. and Kreidenweis, S. M.: Characteristics of atmospheric ice nucleating particles associated with biomass burning in the US: Prescribed burns and wildfires, J. Geophys. Res. Atmos., 119(17), 10458–10470, doi:10.1002/2014JD021980, 2014.

Möhler, O., Benz, S., Saathoff, H., Schnaiter, M., Wagner, R., Schneider, J., Walter, S., Ebert, V. and Wagner, S.: The effect of organic coating on the heterogeneous ice nucleation efficiency of mineral dust aerosols, Environ. Res. Lett., 3(2), doi:10.1088/1748-9326/3/2/025007, 2008.

O'Dell, K., Ford, B., Fischer, E. V and Pierce, J. R.: Contribution of Wildland-Fire Smoke to US PM 2.5 and Its Influence on Recent Trends, Environ. Sci. Technol., 53(4), 1797–1804, doi:10.1021/acs.est.8b05430, 2019.

Onasch, T. B., Trimborn, A., Fortner, E. C., Jayne, J. T., Kok, G. L., Williams, L. R., Davidovits, P., Worsnop, D. R., Hare, C., Olfert, J., Kimmel, J. R., Sueper, D., Coe, H., Allan, J., Cross, E., Ng, S., Liscinsky, D., Mcmanus, B. and Gonzalez, L.: Soot Particle Aerosol Mass Spectrometer: Development, Validation, and Initial Application, Aerosol Sci. Technol., 46, 804–817, doi:10.1080/02786826.2012.663948, 2012.

Paulson, S. E.: The reactions of ozone with alkenes: An important source of HOx in the boundary layer, Geophys. Res. Lett., 23(25), 3727–3730, doi:10.1029/96GL03477, 1996.

Petters, M. D., Carrico, C. M., Kreidenweis, S. M., Prenni, A. J., DeMott, P. J., Collett, J. L. and Moosmüller, H.: Cloud condensation nucleation activity of biomass burning aerosol, J. Geophys. Res., 114(D22), D22205, doi:10.1029/2009JD012353, 2009a.

Petters, M. D., Parsons, M. T., Prenni, A. J., DeMott, P. J., Kreidenweis, S. M., Carrico, C. M., Sullivan, A. P., McMeeking, G. R., Levin, E. J. T., Wold, C. E., Collett, J. L. and Moosmüller, H.: Ice nuclei emissions from biomass burning, J. Geophys. Res., 114(D7), D07209, doi:10.1029/2008JD011532, 2009b.

Polen, M., Lawlis, E. and Sullivan, R. C.: The unstable ice nucleation properties of Snomax bacterial particles, J. Geophys. Res. Atmos., 121(19), 11666–11678, doi:10.1002/2016JD025251, 2016.

Polen, M., Brubaker, T., Somers, J. and Sullivan, R. C.: Cleaning up our water: Reducing interferences from nonhomogeneous freezing of "pure" water in droplet freezing assays of ice-nucleating particles, Atmos. Meas. Tech., 11(9), 5315–5334, doi:10.5194/amt-11-5315-2018, 2018.

Pósfai, M., Gelencsér, A., Simonics, R., Arató, K., Li, J., Hobbs, P. V. and Buseck, P. R.: Atmospheric tar balls: Particles from biomass and biofuel burning, J. Geophys. Res. Atmos., 109(D6), n/a-n/a, doi:10.1029/2003JD004169, 2004.

Prenni, A. J., Demott, P. J., Sullivan, A. P., Sullivan, R. C., Kreidenweis, S. M. and Rogers, D. C.: Biomass burning as a potential source for atmospheric ice nuclei: Western wildfires and

prescribed burns, Geophys. Res. Lett., 39(11), n/a-n/a, doi:10.1029/2012GL051915, 2012.

Reddy, M. S. and Boucher, O.: A study of the global cycle of carbonaceous aerosols in the LMDZT general circulation model, J. Geophys. Res., 109(D14), D14202, doi:10.1029/2003JD004048, 2004.

Reid, J. S., Koppmann, R., Eck, T. F. and Eleuterio, D. P.: A review of biomass burning emissions part II: intensive physical properties of biomass burning particles, Atmos. Chem. Phys, 5, 799–825, 2005.

Robinson, A. L., Donahue, N. M., Shrivastava, M. K., Weitkamp, E. A., Sage, A. M., Grieshop, A. P., Lane, T. E., Pierce, J. R. and Pandis, S. N.: Rethinking organic aerosols: Semivolatile emissions and photochemical aging, Science (80-.)., 315(5816), 1259–1262, doi:10.1126/science.1133061, 2007.

Sedlacek, A. J., Buseck, P. R., Adachi, K., Onasch, T. B., Springston, S. R. and Kleinman, L.: Formation and evolution of tar balls from northwestern US wildfires, Atmos. Chem. Phys., 18(15), 11289–11301, doi:10.5194/acp-18-11289-2018, 2018.

Seinfeld, J. H., Bretherton, C., Carslaw, K. S., Coe, H., DeMott, P. J., Dunlea, E. J., Feingold, G., Ghan, S., Guenther, A. B., Kahn, R., Kraucunas, I., Kreidenweis, S. M., Molina, M. J., Nenes, A., Penner, J. E., Prather, K. A., Ramanathan, V., Ramaswamy, V., Rasch, P. J., Ravishankara, A. R., Rosenfeld, D., Stephens, G. and Wood, R.: Improving our fundamental understanding of the role of aerosol-cloud interactions in the climate system, Proc. Natl. Acad. Sci. U. S. A., 113(21), 5781–5790, doi:10.1073/pnas.1514043113, 2016.

Shrivastava, M., Cappa, C. D., Fan, J., Goldstein, A. H., Guenther, A. B., Jimenez, J. L., Kuang, C., Laskin, A., Martin, S. T., Ng, N. L., Petaja, T., Pierce, J. R., Rasch, P. J., Roldin, P., Seinfeld, J. H., Shilling, J., Smith, J. N., Thornton, J. A., Volkamer, R., Wang, J., Worsnop, D. R., Zaveri, R. A., Zelenyuk, A. and Zhang, Q.: Recent advances in understanding secondary organic aerosol: Implications for global climate forcing, Rev. Geophys., 55(2), 509–559, doi:10.1002/2016RG000540, 2017.

Silva, P. J., Liu, D.-Y., Noble, C. A. and Prather, K. A.: Size and Chemical Characterization of Individual Particles Resulting from Biomass Burning of Local Southern California Species, Environ. Sci. Technol., 33(18), 3068–3076, doi:10.1021/es980544p, 1999.

Stevens-Rumann, C. S., Kemp, K. B., Higuera, P. E., Harvey, B. J., Rother, M. T., Donato, D. C., Morgan, P. and Veblen, T. T.: Evidence for declining forest resilience to wildfires under climate change, edited by F. Lloret, Ecol. Lett., 21(2), 243–252, doi:10.1111/ele.12889, 2018.

Sullivan, R. C., Miñambres, L., Demott, P. J., Prenni, A. J., Carrico, C. M., Levin, E. J. T. and Kreidenweis, S. M.: Chemical processing does not always impair heterogeneous ice nucleation of mineral dust particles, Geophys. Res. Lett., 37(24), 1–5, doi:10.1029/2010GL045540, 2010a.

Sullivan, R. C., Petters, M. D., Demott, P. J., Kreidenweis, S. M., Wex, H., Niedermeier, D., Hartmann, S., Clauss, T., Stratmann, F., Reitz, P., Schneider, J. and Sierau, B.: Irreversible loss of ice nucleation active sites in mineral dust particles caused by sulphuric acid condensation, Atmos. Chem. Phys., 10(23), 11471–11487, doi:10.5194/acp-10-11471-2010, 2010b.

Tkacik, D. S., Robinson, E. S., Ahern, A. T., Saleh, R., Stockwell, C., Veres, P., Simpson, I. J., Meinardi, S., Blake, D. R., Yokelson, R. J., Presto, A. A., Sullivan, R. C., Donahue, N. M. and Robinson, A. L.: A dual-chamber method for quantifying the effects of atmospheric perturbations on secondary organic aerosol formation from biomass burning emissions, J. Geophys. Res. Atmos., 122(11), 6043–6058, doi:10.1002/2016JD025784, 2017.

Vali, G.: Quantitative Evaluation of Experimental Results an the Heterogeneous Freezing Nucleation of Supercooled Liquids, J. Atmos. Sci., 28(3), 402–409, doi:10.1175/1520-0469(1971)028<0402:qeoera>2.0.co;2, 1971.

Vali, G.: Revisiting the differential freezing nucleus spectra derived from drop-freezing experiments: methods of calculation, applications, and confidence limits, Atmos. Meas. Tech., 12(2), 1219–1231, doi:10.5194/amt-12-1219-2019, 2019.

Vassilev, S. V., Baxter, D. and Vassileva, C. G.: An overview of the behaviour of biomass during combustion: Part I. Phase-mineral transformations of organic and inorganic matter, Fuel, 112, 391–449, doi:10.1016/j.fuel.2013.05.043, 2013.

Williams, A. P., Abatzoglou, J. T., Gershunov, A., Guzman-Morales, J., Bishop, D. A., Balch, J. K. and Lettenmaier, D. P.: Observed Impacts of Anthropogenic Climate Change on Wildfire in California, Earth's Futur., 7(8), 892–910, doi:10.1029/2019EF001210, 2019.

3 Reactive Uptake of N_2O_5 on Authentic Biomass-Burning Aerosol

3.1 Abstract

N_2O_5 and $ClNO_2$ were recently demonstrated to be directly produced in biomass-burning plumes. These gaseous reactants affect ozone concentrations, the cycling of oxidants, the lifetime of nitrogen oxides, and the formation of particulate matter, yet the detailed heterogeneous kinetics and product yields of these reactions are still unknown. Existing literature has examined the kinetics of these trace reactants on simplified atmospheric aerosol mimics which may or may not provide results relevant to complex atmospheric particles such as biomass-burning aerosol. In this work, we examine the reactive uptake coefficients (reaction probability) of dinitrogen pentoxide, $\gamma(N_2O_5)$, and the nitryl chloride yield, $\varphi(ClNO_2)$, for four types of authentic biomass-burning aerosol (BBA) at ~35% and ~70% relative humidities (RH) using an entrained aerosol flow tube system. The four biomass fuels tested produce BBA with a range of chloride and organic carbon mass fractions. $\gamma(N_2O_5)$ ranged from 2.1 (±0.4) x 10^{-3} on black needlerush BBA at 34% RH to 6.0 (±0.6) x 10^{-3} on wiregrass BBA at 60% RH, with values generally greater at higher relative humidities within each fuel. After N_2O_5 uptake, the products $ClNO_2(g)$, $HNO_3(g)$, and particulate nitrate were observed and used to calculate a reactive nitrogen budget. $\varphi(ClNO_2)$ was only substantial for the highest-chloride fuel, black needlerush. These results suggest that the complex chemical composition and morphology of BBA as well as the solid phase state of chloride salts in BBA at RH less than ~80% limit the ability for N_2O_5 to heterogeneously react with BBA

and form $ClNO_2$. Additional experiments were conducted for each fuel at 86% RH, above the deliquescence relative humidity (DRH) of the chloride salts common in BBA. For BBA high in particulate chloride, $\gamma(N_2O_5)$ was further increased by 100-300% to 7.2 x 10^{-3} for saw palmetto BBA and 16 x 10^{-3} for black needlerush BBA. Low chloride fuels exhibited little change in $\gamma(N_2O_5)$ at high versus low RH, demonstrating how aqueous chloride in the particles drives N_2O_5 reactive uptake. Preliminary analysis revealed that the two high chloride fuels produced the only $ClNO_2$(g) above background concentrations. Given that biomass-burning events release high quantities of particulate matter, chlorine species, and nitrogen oxide gases (NO_x), accurately quantifying N_2O_5 heterogeneous kinetics on BBA is important for accurate predictions of the effects of wildfires on atmospheric chemistry, particulate matter, and atmospheric oxidant budgets.

3.2   Introduction

Knowledge of the atmospheric budget of reactive species expands our understanding of atmospheric chemistry and is necessary for predicting the formation and concentrations of particulate matter (PM), oxidants, and other pollutants that contribute to climate change, poor air quality, and negative health conditions. Biomass burning (BB) occurs globally year-round, releasing substantial PM, CO and CO_2, carbonaceous gases, and nitrogen oxides (NO_x = NO + NO_2). At night, NO_2 can react with residual ozone to form the nitrate radical ($NO_3\bullet$), which can then react with additional NO_2 to form dinitrogen pentoxide, N_2O_5, as shown below in R1 (Abbatt et al., 2012; Dentener and Crutzen, 1993; Thornton et al., 2003). If N_2O_5 remains in the gas phase nocturnally, the lifetime of NO_x is extended until the morning when NO_3 photolysis and reaction with NO reduces the concentration of N_2O_5 through thermal equilibrium. However, when N_2O_5 reacts heterogeneously with an aerosol particle (R2), aqueous nitrated intermediates form (R3) that then can go on to form HNO_3 (R4). Deposition of HNO_3 is rapid and presents a net removal of two NO_x. Alternatively N_2O_5 hydrolysis can go on to form $ClNO_2$ if aqueous chloride is present in the aerosol particle (R5) (Finlayson-Pitts et al., 1989). Other products may also form after

reactions with other species such as iodide or phenols, represented by X in R6. ClNO$_2$ rapidly evaporates from the particle (R7), but photolyzes when the sun rises into NO$_2$ and Cl• (R8). This overall reaction is shown in R9, where φ is the yield of ClNO$_2$ versus the HNO$_3$ channel.

$$NO_2(g) + NO_3(g) \rightleftharpoons N_2O_5(g) \tag{R1}$$

$$N_2O_5(g) \rightleftharpoons N_2O_5(p) \tag{R2}$$

$$N_2O_5(p) + H_2O(p) \rightleftharpoons NO_3^-(aq) + H_2ONO_2^+(aq) \tag{R3}$$

$$H_2ONO_2^+(aq) + H_2O(p) \rightarrow H_3O^+(aq) + HNO_3(aq) \tag{R4}$$

$$H_2ONO_2^+(aq) + Cl^-(aq) \rightarrow ClNO_2(aq) \tag{R5}$$

$$H_2ONO_2^+(aq) + X(aq) \rightarrow products \tag{R6}$$

$$ClNO_2(aq) \rightleftharpoons ClNO_2(g) \tag{R7}$$

$$ClNO_2(g) + hv \rightarrow Cl(g) + NO_2(g) \tag{R8}$$

$$N_2O_5(g) + particles \rightarrow \varphi ClNO_2 + (2-\varphi)HNO_3 \tag{R9}$$
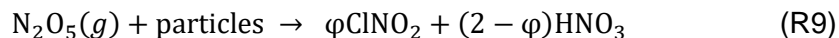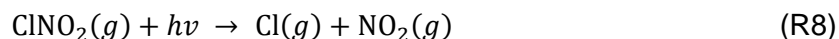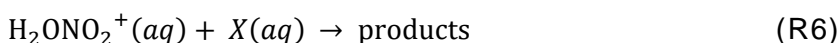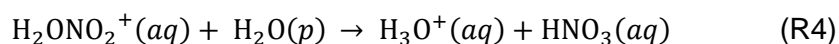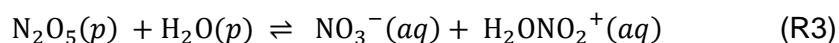
Understanding the formation of ClNO$_2$ is important as the chlorine atom is a strong atmospheric oxidant and affects the production of hydroxyl radicals (the most common atmospheric oxidant of similar reactivity to Cl•), ozone, hydrocarbon oxidation, and secondary PM (Bannan et al., 2019; Haskins et al., 2019; McNamara et al., 2019; Riedel et al., 2013, 2014; Sarwar et al., 2014). Renewed interest in identifying sources of ClNO$_2$ began when high concentrations were measured inland, as ClNO$_2$ was originally thought to only form in sea spray aerosol that contains high concentrations of sodium chloride (Mielke et al., 2011; Thornton et al., 2010). As biomass burning releases both NO$_x$ — from the combustion of nitrogen present in all biomass fuels — and particulate chloride, present in many plant species, biomass-burning aerosol represented a likely yet unexplored candidate for N$_2$O$_5$ and ClNO$_2$ formation (Levin et al., 2010; Lobert et al., 1999; McMeeking et al., 2009). Several studies of ambient air detected N$_2$O$_5$ and/or

ClNO$_2$ in air masses that shared various markers for BB, but until recently there was no direct evidence that either of these molecules were produced in biomass-burning plumes (Tereszchuk et al., 2011; Tham et al., 2016). Our prior chamber reactor experiments demonstrated for the first time that authentic biomass-burning aerosol could produce N$_2$O$_5$ and subsequently ClNO$_2$ in high-chloride biomass fuels under dark conditions, following the addition of ozone (Ahern et al., 2018).

Experimental challenges such as long, uneven mixing and chamber wall effects did not allow for the determination of N$_2$O$_5$ heterogeneous kinetics in these previous chamber reactor experiments. Yet, the reactive uptake coefficient of N$_2$O$_5$ (γ(N$_2$O$_5$)) and nitryl chloride yield (φ(ClNO$_2$)) have important atmospheric implications and are known to vary based on particle composition and morphology. In particular, high water content increases γ(N$_2$O$_5$) by promoting hydrolysis, particulate nitrate can reduce γ(N$_2$O$_5$) by up to an order of magnitude in what is called the 'nitrate effect' (R3), and particulate chloride enhances γ(N$_2$O$_5$) and leads to ClNO$_2$ formation (Bertram and Thornton, 2009; Mentel et al., 1999; Thornton et al., 2003). Organic carbon coatings have also been shown to reduce γ(N$_2$O$_5$), and primary organic aerosol makes up a large fraction of biomass-burning aerosol and may be present as coatings (Ahern et al., 2018; Anttila et al., 2006; Gaston et al., 2014, Jahn et al., 2020). Thus far, γ(N$_2$O$_5$) has only been calculated on other organic aerosol or BBA proxies (Abbatt et al., 2012; Bertram and Thornton, 2009; Escorcia et al., 2010; Gaston et al., 2014; Knopf et al., 2011) which may not represent authentic BBA and its complex composition and morphology (Ahern et al., 2016; Li et al., 2003; Pósfai et al., 2003; Reid et al., 2005). Therefore, in this chapter, we investigate N$_2$O$_5$ reactive uptake and ClNO$_2$ production in authentic biomass-burning aerosol generated from a live fire, using a custom entrained aerosol flow tube reactor system.

3.3   Methods

3.3.1   BBA generation

Biomass fuels were combusted in a galvanized steel pan and emissions were injected into a either a 2 m^3 or 10 m^3 Teflon smog chamber using two Dekati diluters in parallel. The fuels used were saw palmetto (*Serenoa repens*, collected at the Okefenokee National Wildlife Refuge in Georgia, USA), wiregrass (*Aristida stricta,* collected at the Okefenokee National Wildlife Refuge in Georgia, USA), black needlerush (*Juncus roemerianus,* collected at the Alligator River National Wildlife Refuge in North Carolina, USA), and longleaf pine needles (*Pinus palustris,* fallen needles collected in Milan, Georgia, USA). All of these biomass types are common throughout the United States. A small portion of the fuel was ignited using a butane lighter, then additional fuel was added to the fire to maintain flaming-phase combustion, until a high enough concentration of aerosol surface area was reached in the chamber. Between experiments, the chamber was flushed with filtered, clean air and exposed to UV lights to clean the chamber until particle concentrations reached < 20 cm^{-3}. During experiments, the chamber was shielded from any light as these experiments targeted nocturnal chemistry.

3.3.2   Entrained aerosol flow tube reactors

Two custom designed and constructed entrained aerosol flow tube reactors were used; experimental setups are shown in Figure 3-1. The University of Washington UW-flow tube was a 90 cm long Pyrex cylinder with an inner diameter of 9 cm. The CMU-flow tube was 122 cm in long with an inner diameter of 10.2 cm. The inner walls of both flow tubes were coated with halocarbon wax (Series 1500 Inert Wax, Halocarbon Products Corp.) to make the glass surface more chemically inert, and the outsides were covered to block room light. Flow tubes were kept at room temperature and atmospheric pressure and were continually flushed with clean air between experiments. Downstream of the smog chamber, an activated carbon denuder and a Purafil permanganate denuder were used to remove volatile organic compounds (VOCs) and NO_x,

respectively, created from the biomass combustion that could interfere with the N_2O_5 reactions occurring in the flow tubes. The scrubbing efficiencies of the denuders after all experiments were completed were > 90% NO_x (measured by an Advanced Pollution Instrumentation Inc. NO_x monitor), and > 95% VOCs (measured by an Ionicon Analytic GmbH PTR-MS with 500 ppt limit of detection).

For the UW-flow tube, the desired relativity humidity (RH) was reached by passing purified nitrogen through a water bubbler at room temperature. For the CMU-flow tube, the desired relative humidity was reached by passing purified air through a heated three-neck flask filled with MilliQ water to access high RH > 80% conditions. Both flow tubes had long sections of tubing that served as RH-conditioning tubes before the aerosol reached the kinetics flow tube reactor itself.

Aerosol particles were filtered either just prior to the UW-flow tube using a Teflon membrane filter unit, or just after the chamber for the CMU-flow tube using a nylon Parker filter; each of these setups allowed for switching to a bypass line to transfer the aerosol into the kinetics flow tube. The filtered mode was used to determine the background levels of reactants and products and wall loss rates of N_2O_5 following the "perturbation" method (Bertram et al., 2009a). Filters had to be carefully selected such that the BBA was efficiently removed from the aerosol flow while avoiding large pressure drops across the filter unit that would create unrealistic responses in the CIMS ion signals and alter the $N_2O_5(g)$ generation source. NO_2 from a 10 ppm NO_2 in N_2 tank was reacted with an excess of ozone in a small Teflon vessel to produce a steady source of N_2O_5. The N_2O_5 was introduced into the flow tubes through a 1/8" Teflon line that entered the beginning of the kinetics flow tubes through an orthogonal port.

3.3.3 Instrumentation

Gas-phase measurements included NO_x (Advanced Pollution Instrumentation Inc., Model 200A) and ozone (Dasibi Environmental Corp., Model 1008-PC). Relative humidity was either

checked periodically during UW-flow tube experiments (Vaisala HMP233) or continuously monitored at the end of the flow tube during CMU-flow tube experiments (Vaisala HMT120). An HR-LToF-CIMS using iodide-adduct ionization constantly monitored $N_2O_5(g)$ and $ClNO_2(g)$ concentrations. Iodide reagent ions were generated by passing methyl iodide vapor in dry nitrogen through a ^{210}P 10 mCi radioactive source. $ClNO_2$ was calibrated by passing N_2O_5 over an aqueous NaCl salt bed, assuming a stoichiometric conversion of N_2O_5 to $ClNO_2$ (Finlayson-Pitts et al., 1989; Lee et al., 2018; McNeill et al., 2006; Roberts et al., 2009).

Size distributions of the BBA were measured at the end of the flow tube using a DMA (TSI Inc. model 3082) and CPC (TSI Inc. model 3775) acting as a Scanning Mobility Particle Sizer (SMPS) with an aerosol flow rate of 0.3 lpm and sheath flow rate of 3.0 lpm. Submicron aerosol chemical composition was measured using a Soot-Particle Aerosol Mass Spectrometer (SP-AMS, Aerodyne), although most measurements are presented with the SP laser off (EI mode) to maximize the number of experiments available. In laser-off mode only non-refractory aerosol components are measured, while laser-on mode also measures black carbon soot aerosol. Total BBA surface area concentrations in the flow tube typically ranged from 0.5 to 2.0 x 10^4 μm^2 cm^{-3} and decreased throughout the experiment as the Teflon chamber reservoir was depleted of aerosol. This method of providing BBA to the flow tube was ideal as it allowed for the experiments to be conducted on authentic BBA while still providing a fairly steady source of aerosol particles.

BBA particles were collected onto copper TEM grids with a formvar coating (carbon type B, 400 mesh, Ted Pella #01754-F) using a Microorifice Uniform Deposit Impactor (MOUDI) during separate experiments using the same biomass fuel types sourced from the same locations, but the particles collected were from burns different than those conducted for the flow tube experiments. Transmission electron microscopy/energy dispersive X-ray spectroscopy (TEM/EDX) measurements were acquired at the Environmental Molecular Sciences Laboratory (EMSL) at PNNL using a Titan 80-300 scanning/transmission electron microscope equipped with

an Si(Li) detector at an accelerating voltage of 300 keV. Computer-controlled scanning electron microscopy (CCSEM) measurements were also performed at EMSL using a Quanta 3D environmental SEM (FEI) with a Si(Li) detector. Particles greater than 200 nm in diameter were imaged at 10,000x magnification at an accelerating voltage of 20.00 keV.
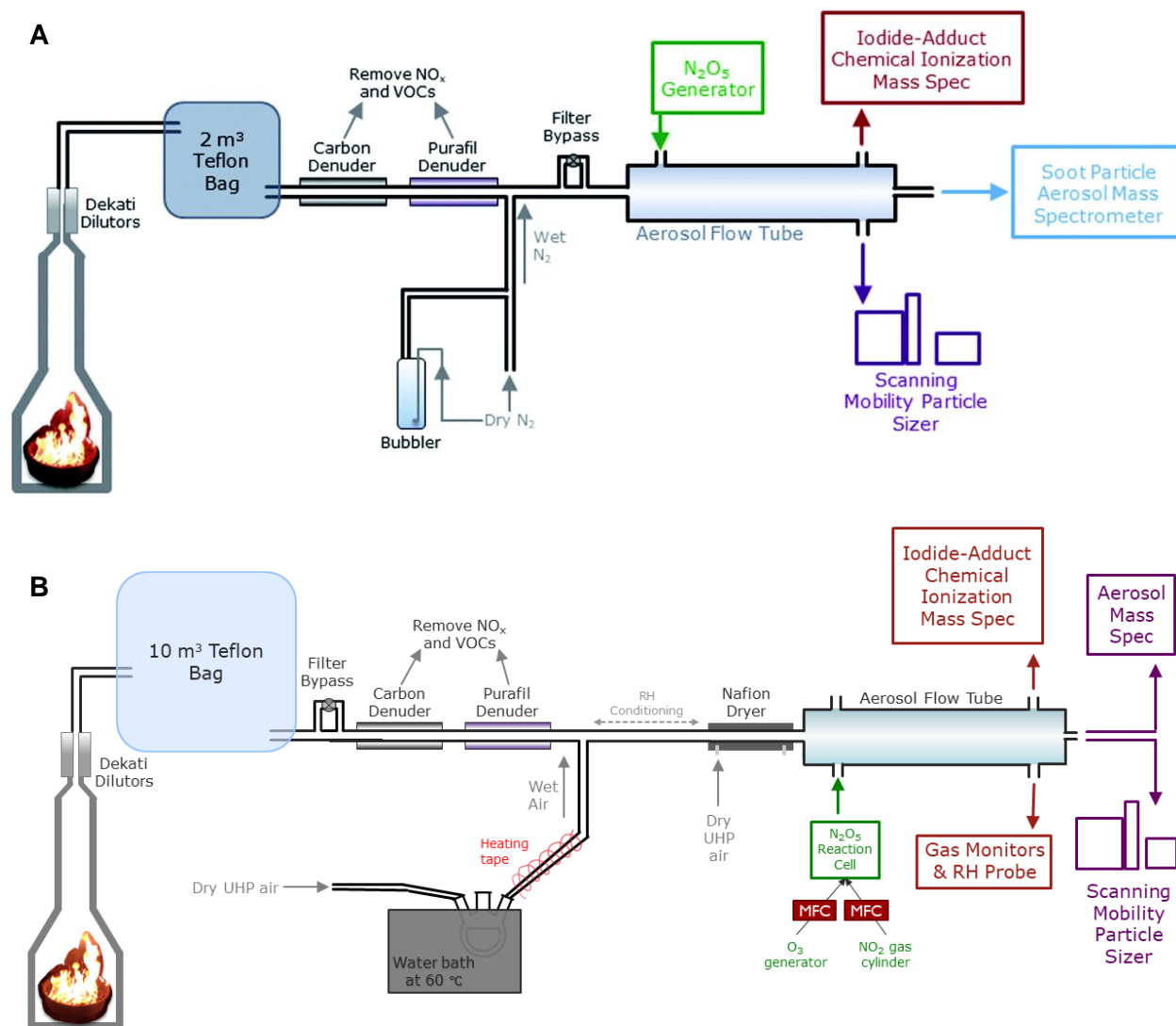
Figure 3-1. A) Experimental setup for UW-entrained aerosol flow tube reactor, reproduced from Goldberger et al. (2019). **B)** Experimental setup for CMU-flow tube. Key differences include a larger Teflon smog chamber that contained the BBA source to allow for longer experiments, a larger flow tube to allow for increased instrumental sampling flow rates while maintaining a two minute aerosol flow tube residence time, and a different RH control system to enable higher relative humidities.

3.3.4 Determination of heterogeneous kinetics parameters k_{het}, $\gamma(N_2O_5)$, and $\varphi(ClNO_2)$

Equations 1-3 describe the rate of change of N_2O_5 and the products $ClNO_2$ and HNO_3 that form following the uptake of N_2O_5 into a particle. Assuming that N_2O_5 is successfully accommodated into the particle, as in R2, and goes on to form either $ClNO_2$ or HNO_3, φ represents the branching ratio between these two products. k_{het} is the pseudo-first order reaction rate constant for the reactive uptake of N_2O_5 into BBA. As shown in Equation 4, k_{het} is dependent on the heterogeneous reactive uptake probability, $\gamma(N_2O_5)$, as well as the mean molecular speed of N_2O_5, ω, and the aerosol particle surface area per volume of air, S_a.

$$\frac{d[N_2O_5]}{dt} = -k_{het}[N_2O_5] \qquad (E1)$$

$$\frac{d[ClNO_2]}{dt} = \varphi k_{het}[N_2O_5] \qquad (E2)$$

$$\frac{d[HNO_3]}{dt} = (2 - \varphi)k_{het}[N_2O_5] \qquad (E3)$$

$$k_{het} = \frac{\gamma_{N_2O_5}\omega S_a}{4} \qquad (E4)$$

These parameters were calculated using the particle modulation technique described in Bertram et al. (2009a) and in the Methods above. Here, a steady concentration of N_2O_5 is input into the flow tube and the total instrumental flow pulling from the smog chamber into the flow tube is kept constant so that the residence time in the flow tube (Δt) is static. When BBA is injected into the chamber then pulled into the flow tube, it reacts with the N_2O_5 in the flow tube such that the gas-phase concentration of N_2O_5 decreases. The experimental setup can then be switched such that the BBA is filtered out before reaching the flow tube, and thus the N_2O_5 concentrations increase again. The flow can be switched multiple times between bypass and filtered modes to obtain multiple measurements of N_2O_5 concentrations at the end of the flow tube both with and without particles. This determines the background loss rate of N_2O_5 such as to the flow tube walls, and background levels of N_2O_5 and $ClNO_2$. After measuring these values and assuming that the

N_2O_5 reaction rates on the walls and with BBA are both first-order in N_2O_5, k_{het} can be calculated as it is proportional to the natural logarithm of the difference between N_2O_5 concentrations during filtered versus aerosol bypass modes, shown in Equation 5 (Bertram et al., 2009a).

$$k_{het} = -\frac{1}{\Delta t} \, ln \left(\frac{[N_2O_5]^{with\ particles}}{[N_2O_5]^{without\ particles}} \right)$$ (E5)

[N_2O_5] is determined by the CIMS. The value for k_{het} obtained here can then be used in Equation 4 to calculate $\gamma(N_2O_5)$, with updated surface area values (S_a) for each modulation between filtered and bypass modes. $\gamma(N_2O_5)$ was calculated from a linear fit of k_{het} vs. S_a to average values; the overall S_a concentration of BBA in the chamber reservoir decreased throughout each experiment but $\gamma(N_2O_5)$ remained steady. Gas-phase diffusion is not a kinetic limitation in these experiments due to the small particle sizes present and low reactive uptake coefficients measured here (Thornton and Abbatt, 2005).

To calculate $\varphi(ClNO_2)$, any $ClNO_2$ produced by reactions of N_2O_5 on flow tube walls must be subtracted from $ClNO_2$ produced by reactions of N_2O_5 on biomass-burning particles. Therefore, we calculated a $ClNO_2$ wall production efficiency using the measured $ClNO_2/N_2O_5$ ratio while the particle filter was inline. The assumption that the production efficiency of $ClNO_2$ from the flow tube walls was not dependent on the presence of BBA was supported since background $ClNO_2$ concentrations while BBA was filtered stayed relatively constant across the filter/bypass modulations during the length of each experiment. $ClNO_2$ produced solely by reactions of N_2O_5 reactions on BBA could then be calculated by subtracting wall-produced $ClNO_2$ from total observed $ClNO_2$. Observed mass spectral $ClNO_2$ ion signal was scaled relative to N_2O_5 by a factor of 1.5 as determined by CIMS sensitivity calibrations to account for the lower instrument response to $ClNO_2$. The yield of $ClNO_2$ can then be calculated by the ratio of the $ClNO_2$ mole fraction produced in BBA ($\Delta ClNO_2$) to the N_2O_5 mole fraction that reacted on the BBA (ΔN_2O_5), using Equation 6.

$$\varphi ClNO_2 = \frac{\Delta ClNO_2}{\Delta N_2O_5} \qquad (E6)$$

3.3.5   Control experiments

To validate the experimental setup, the reactive uptake coefficient of N_2O_5 on deliquesced ammonium bisulfate (ABS) particles was tested as this is a well-studied reaction system that provides a reliable calibration of the two custom flow tube reactors and analysis methods used here (Bertram and Thornton, 2009; Mentel et al., 1999; Wahner et al., 1998). ABS in milli-Q water was atomized (Aerosol Generator 3076, TSI Inc.) and passed through the RH conditioning tube to reach 55% RH before entering the flow reactor to ensure the ABS remained in an aqueous deliquesced state above the efflorescence RH of < 35% RH (Imre et al., 1997; Seinfeld and Pandis, 1998). ABS surface area concentrations similar to the BBA concentrations present during these experiments were used, and the same perturbation method was used to calculate $\gamma(N_2O_5)$. The reactive uptake coefficient of N_2O_5 on ABS aerosol in these control experiments was 0.009 ± 0.004 for the UW-flow tube and 0.025 ± 0.007 for the CMU-flow tube, both within range of literature values (0.005-0.03) (Bertram and Thornton, 2009). Additional control experiments included periodically stopping the source flow of N_2O_5 to measure background concentrations of HNO_3 and $ClNO_2$, modulating between filter and bypass mode with no aerosol added to the system to ensure that N_2O_5 concentrations remained steady, and sampling the BBA at the entrance of the flow tube with the AMS to evaluate particle losses throughout the flow reactor, which were negligible.

3.4   Results and discussion

3.4.1   Particle- and gas-phase chemical composition and reactivity

Typical non-refractory chemical compositions for each BBA type produced from the four biomass fuels as measured by the AMS are shown in Figure 3-2 (left) with detailed composition for each experiment also listed in Table 3-1. Organic aerosol (OA) was the predominant

component for all fuel types, although the exact percentages of each component exhibited natural variation between each replicate burn; the mean value from experiments of the same fuel type will be used in the following discussions. The four biomass fuels were chosen primarily because of their prevalence across fire-prone regions of the United States and also based off of previous literature to have two fuels with high chloride levels and two with low chloride (Levin et al., 2010; McMeeking et al., 2009). Indeed, we found that black needlerush and saw palmetto had the highest chloride mass content in the BBA (22% and 18% respectively), while wiregrass and longleaf pine needles BBA had lower chloride content (4.7% and 2.4% respectively). Black needlerush also had high concentrations of other inorganic components, such as 4.5% nitrate and 6.3% sulfate, much higher than the other three fuels. Longleaf pine needle BBA had the highest concentration of organic aerosol with a mass fraction of 95%, followed by wiregrass at 91%. An example surface area distribution as measured by the SMPS is shown in Figure 3-2 (right); other experiments exhibited similar distributions.
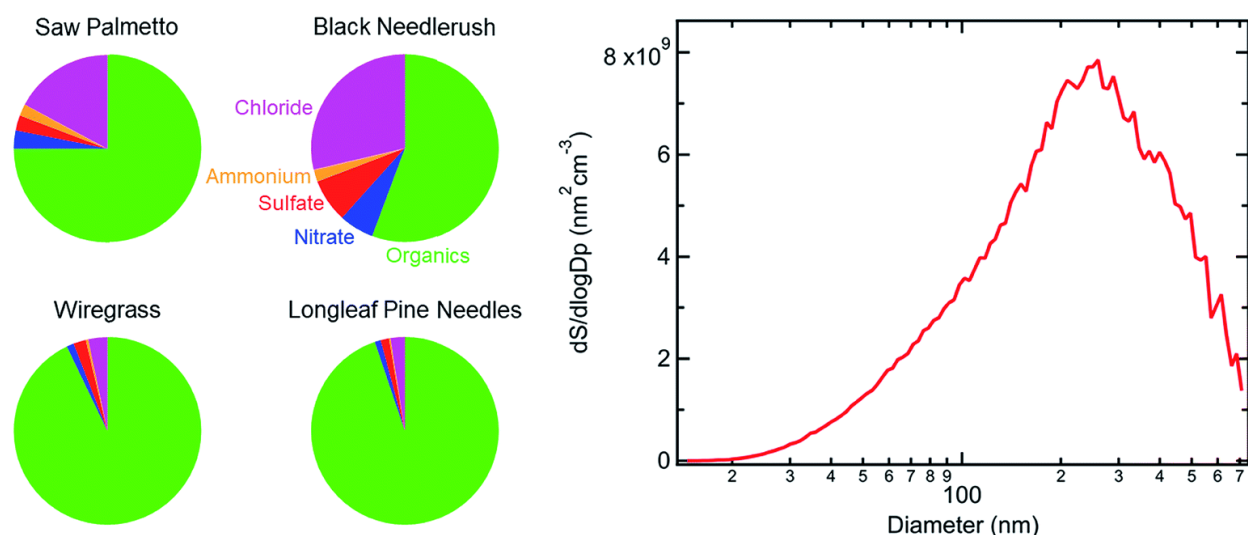
Figure 3-2. Left: Non-refractory chemical composition of BBA produced by combustion of each of the four fuels listed, as measured by the AMS. Average composition shown as percentage of total PM_1 from low RH experiments before exposure to N_2O_5. Right: Example BBA surface area size distribution from a wiregrass low RH experiment. The surface area mean diameter increased slightly (~15%) over the course of each experiment. Reproduced from Goldberger et al. (2019).

77

Table 3-1. Non-refractory chemical composition of BBA for each experiment before exposure to N_2O_5. Absolute concentrations are shown in units of $\mu g\ m^{-3}$ and mass percentages are shown in parentheses.

BBA fuel type	RH (%)	OA [$\mu g\ m^{-3}$]	Nitrate [$\mu g\ m^{-3}$]	Sulfate [$\mu g\ m^{-3}$]	Ammonium [$\mu g\ m^{-3}$]	Chloride [$\mu g\ m^{-3}$]
Saw palmetto	40	48 (75%)	2.0 (3.1%)	1.7 (2.7%)	1.3 (2.0%)	11 (17%)
Saw palmetto	60	49 (72%)	1.7 (2.5%)	2.6 (3.8%)	1.7 (2.5%)	13 (19%)
Wiregrass	37	85 (93%)	1.1 (1.2%)	2.0 (2.2%)	0.4 (0.4%)	3.0 (3.3%)
Wiregrass	70	29 (89%)	0.9 (2.8%)	0.6% (1.8%)	0.2 (0.6%)	2.0 (6.1%)
Black needlerush	34	68 (56%)	7.3 (6.0%)	9.2 (7.5%)	2.6 (2.0%)	35 (29%)
Black needlerush	76	135 (75%)	5.4 (3.0%)	9.3 (5.1%)	1.9 (1.1%)	29 (16%)
LL pine needles	30	77 (95%)	0.8 (1.0%)	1.2 (1.5%)	0.2 (0.3%)	2.0 (2.5%)
LL pine needles	76	126 (96%)	1.2 (0.9%)	1.2 (0.9%)	0.5 (0.4%)	3.0 (2.3%)

Regardless of fuel type, it was expected that there would be at least some uptake of N_2O_5 into the particle phase when BBA was present in the flow tube due to N_2O_5 hydrolysis on the particles; an example of this is shown in Figure 3-3. After the fuel was combusted and the initial aerosol composition was measured, N_2O_5 was introduced into the flow tube, as seen by the increase in the red line. As soon as the aerosol was removed in filter mode, the N_2O_5 decreased, and this trend continued throughout multiple filter/bypass modulations. This inverse relationship between N_2O_5 and the presence of aerosol particles clearly shows the uptake of N_2O_5 into the BBA. When BBA was continually introduced into the flow reactor (yellow & green horizontal bars) but N_2O_5 addition was modulated on/off, particulate nitrate (pNO$_3$) increased and particulate chloride (pCl) decreased while N_2O_5 was present. This trend will be examined further below.
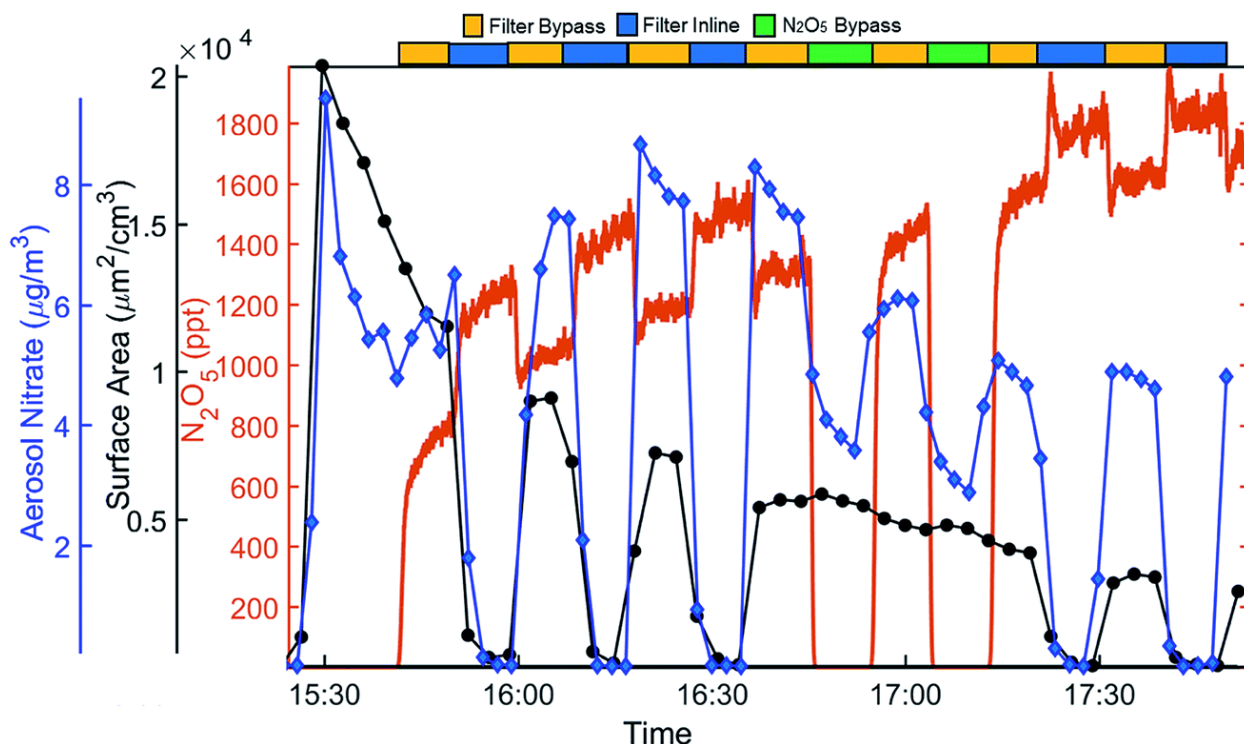
Figure 3-3. Example N_2O_5 reactive uptake experiment for black needlerush BBA at 75% RH. BBA was first introduced before 15:30. N_2O_5(g) measured by CIMS (red line) decreases whenever aerosol is present in the flow tube during filter bypass mode (indicated by yellow bars on top). During times when the particle filter was inline (blue bars), total BBA surface area measured by the SMPS (black circles) and particulate nitrate measured by the AMS (blue diamonds) decreased to nearly 0. Green bars indicate when N_2O_5 was not present in flow tube and bypass line was maintained. Reproduced from Goldberger et al. (2019).

3.4.2   Determination of N_2O_5 reactive uptake probability, $\gamma(N_2O_5)$

The N_2O_5 signal and particle surface area were used to calculate $\gamma(N_2O_5)$ based off of Equations 4 and 5. Figure 3-4 shows the natural logarithm of the ratio of N_2O_5 signal with over without BBA present in the flow reactor plotted versus the BBA surface area. Each of the four different fuel types are shown at two different relative humidities, ~35% and ~70%. The slope of each least-squares line of best fit can be scaled by the flow tube residence time, Δt, and the mean molecular speed of N_2O_5 using Eqns. 4 and 5 and is then directly proportional to $\gamma(N_2O_5)$. This linear relationship ($R^2 > 0.8$) supports the fact that N_2O_5 uptake is caused by heterogeneous reaction on the BBA particle surfaces. N_2O_5 ion signal was normalized by the signal for the reagent

ion, I[-], and its cluster with water, [I•H_2O][-], to account for changes in N_2O_5 signal due to availability of the reagent ion rather than due to uptake into BBA.
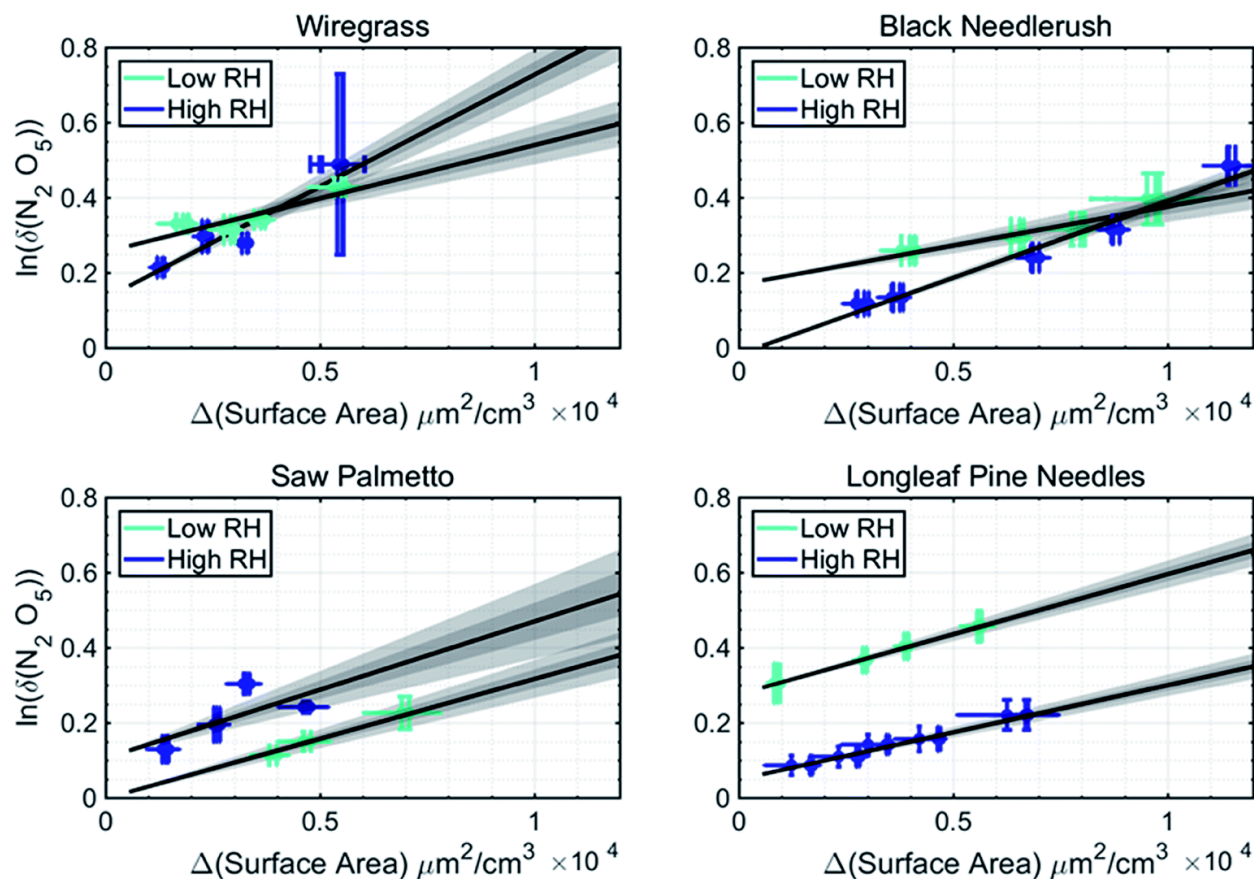
Figure 3-4. Determination of reactive uptake probability of N_2O_5, $\gamma(N_2O_5)$, on biomass-burning aerosol under low (aqua) and high (blue) RH conditions. The y-axis is the change in N_2O_5 for bypass versus filter modes, and the x-axis is the change in aerosol surface area for bypass versus filter modes. Error bars are uncertainties related to each experimental measurement and shaded gray error regions around lines of best fit are bounds of 1σ and 2σ uncertainty propagated from underlying variables. Best fit lines for each experiment are: wiregrass, 37% RH: $y = 2850 \pm 260x + 0.25$; wiregrass, 60% RH: $y = 6270 \pm 340x + 0.12$; black needlerush, 34% RH: $y = 2200 \pm 210x + 0.16$; black needlerush, 76% RH: $4130 \pm 120x - 0.02$; saw palmetto, 40% RH: $y = 3500 \pm 250x - 0.02$; saw palmetto, 60% RH: $y = 3820 \pm 500x + 0.1$; longleaf pine needles, 30% RH: $y = 3250 \pm 180x + 0.27$; longleaf pine needles, 76% RH: $y = 2670 \pm 140x + 0.04$. Reproduced from Goldberger et al. (2019).

The reactive uptake coefficients determined for N_2O_5 on BBA from each fuel type at low and high relative humidities are shown in Table 3-2; values ranged from 2.1– 6 x 10^{-3}. Within three out of four fuel types, the uptake coefficient at high RH was higher than that at low RH, as is expected (Bertram and Thornton, 2009). The biomass fuel that did not follow this trend, longleaf pine needles, had the highest mass percentage of organic aerosol (95%), and the lack of a positive trend between RH and N_2O_5 uptake is possibly due to the particle morphology as organic coatings are known to inhibit $\gamma(N_2O_5)$ (Anttila et al., 2006; Gaston et al., 2014; Ryder et al., 2015; Jahn et al., 2020). Both wiregrass BBA (4.7% pCl) and black needlerush BBA (22% pCl) had $\gamma(N_2O_5)$ values that doubled for low versus high RH: from ~3 x 10^{-3} to ~6 x 10^{-3} for the wiregrass BBA and from ~2 x 10^{-3} to ~4 x 10^{-3} for the black needlerush. The particulate chloride also had the largest decrease upon exposure to N_2O_5 in wiregrass BBA at 60% RH, but no $ClNO_2$ was detected. Saw palmetto BBA had a smaller increase in $\gamma(N_2O_5)$ with increased RH and exhibited the largest change in pNO_3 and smallest change in pCl after exposure to N_2O_5. This indicates that most N_2O_5 uptake into BBA produced HNO_3 rather than $ClNO_2$.

There were no strong trends between $\gamma(N_2O_5)$ and bulk BBA chemical composition. Particulate organic aerosol and nitrate are known to suppress N_2O_5 uptake and may have played a role here (Bertram and Thornton, 2009; Gaston et al., 2014). For example, wiregrass and longleaf pine needle BBA both had organic aerosol mass fractions > 90% as well as fairly high nitrate to chloride ratios of 0.3 and 0.4, respectively, in the nascent BBA. These fuels also exhibited the smallest changes in pNO_3 after N_2O_5 exposure – a 70% and 50% increase for wiregrass and LL pine needles, respectively. Black needlerush also had a smaller pNO_3 increase after N_2O_5 exposure of 87%, but had a higher $ClNO_2$ yield of 50% compared to < 1%. Changes in nitrogen-containing particle- and gas-phase species are summarized in Table 3-3 and a longer discussion of the reactive nitrogen budget is presented below.

Table 3-2. N_2O_5 reactive uptake probability ($\gamma(N_2O_5)$) and $ClNO_2$ product yield ($\varphi(ClNO_2)$) for each BBA kinetics experiment. Experimentally-observed uncertainty levels (2σ) are given in parentheses.

BBA fuel type	RH (%)	$\gamma(N_2O_5)$ $(2\sigma)^a$ x 10^{-3}	$\varphi(ClNO_2)$ % (2σ)
Saw palmetto	40	3.2 (0.5)	< 1 (2)
Saw palmetto	60	3.6 (1)	< 0.5 (1.5)
Wiregrass	37	2.8 (0.6)	ND[b]
Wiregrass	70	6.0 (0.6)	ND[b]
Black needlerush	34	2.1 (0.4)	6 (2)
Black needlerush	76	4.1 (0.2)	50 (9)
LL pine needles	30	3.2 (0.4)	ND[b]
LL pine needles	76	2.5 (0.4)	ND[b]

[a]2σ uncertainty corresponds to the variability observed over the course of the experiment
[b]ND stands for "not detected", which was the case for all $\varphi(ClNO_2)$ values from low-chloride fuels.

Table 3-3. Reactive nitrogen budget during all experiments based on CIMS measurements of N_2O_5, HNO_3, and $ClNO_2$, and AMS measurements of particulate NO_3; measurement uncertainties are shown in parentheses. Nitrogen balance percentage was determined using Equation 7 and reflects whether or not the reactive nitrogen lost during N_2O_5 uptake is accounted for in the products $HNO_3(g)$, $ClNO_2(g)$ or pNO_3.

BBA fuel type	RH (%)	$2\Delta N_2O_5(g)$ (pptv)	$\Delta HNO_3(g)+$ $\Delta ClNO_2(g)$ (pptv)	ΔpNO_3 (pptv)	N balance (%)
Saw palmetto	40	726 (220)	321 (100)	378 (110)	4 ± 6
Saw palmetto	60	1136 (340)	911 (270)	322 (100)	-9 ± 31
Wiregrass	37	2843 (850)	870 (260)	136 (40)	65 ± 42
Wiregrass	70	2329 (700)	1086 (330)	146 (40)	47 ± 26
Black needlerush	34	2000 (600)	1204 (360)	1512 (450)	-36 ± 32
Black needlerush	76	319 (100)	165 (50)	957 (290)	-250 ± 78
LL pine needles	30	2300 (690)	1054 (316)	60 (20)	52 ± 51
LL pine needles	76	394 (120)	97 (30)	100 (30)	50 ± 19

3.4.3 $ClNO_2$ production and yield

As N_2O_5 addition into the flow tube most often resulted in an increase in particulate nitrate without a decrease in particulate chloride or increase in gas-phase $ClNO_2$, most N_2O_5 uptake presumably resulted in production of HNO_3 rather than $ClNO_2$. HNO_3 cannot be measured

instantaneously in the CIMS as $ClNO_2$ can be measured because of the memory effects of HNO_3 that slowly desorbs from the flow reactor walls. Instead, we must assume that N_2O_5 that did not go on to produce $ClNO_2$ (R5) and instead produced HNO_3 (R4). There is also evidence of acid displacement in the wiregrass experiment where pCl did decrease without an increase in $ClNO_2$, suggesting the displacement of HCl by the stronger acid HNO_3. HCl was not detected during these experiments, but it may have been present below the detection limit of ~ 0.5 ppb (Lee et al., 2018). HCl is difficult to detect by iodide-adduct CIMS because it forms a weak cluster with the reagent ion and an overlapping ion occurs in high relative humidity conditions (Lee et al., 2014).

An experimental timeline of chlorine activation in the black needlerush BBA at 75% RH is shown in Figure 3-5, as this was the fuel tested with the highest $ClNO_2$ product yield. Once N_2O_5 is introduced into the flow tube, $ClNO_2$ is produced during both filter inline and filter bypass (BBA present) modes, suggesting that $ClNO_2$ is produced on both the BBA and the walls of the flow tube. The background $ClNO_2$ produced from surface chemistry on the walls (green trace) remains fairly constant throughout the experiment. The total $ClNO_2$ signal (black trace) decreases whenever the BBA was filtered out, but it also decreases over the entire experiment as BBA surface area decreases. The $ClNO_2$ signal also drops to zero when N_2O_5 is not added to the flow tube (N_2O_5 bypass, green bars in Fig. 3-5), indicating that any $ClNO_2$ production and evaporation from surfaces occurs promptly and there is little carryover between filtered and bypass modes. Subtracting the $ClNO_2$ produced from the walls measured during filter mode from the total $ClNO_2$ signal provides an estimate of the $ClNO_2$ produced following N_2O_5 uptake into chloride-containing BBA (purple trace). Naturally, this value falls to nearly zero when the aerosol was filtered which helps confirm the reliability of this analysis. Other experiments with the high-chloride fuels (black needlerush and saw palmetto) exhibited similar trends but $ClNO_2$ concentrations were much lower, and $ClNO_2$ production was not observed in the BBA from low-chloride fuels (wiregrass and longleaf pine needles).
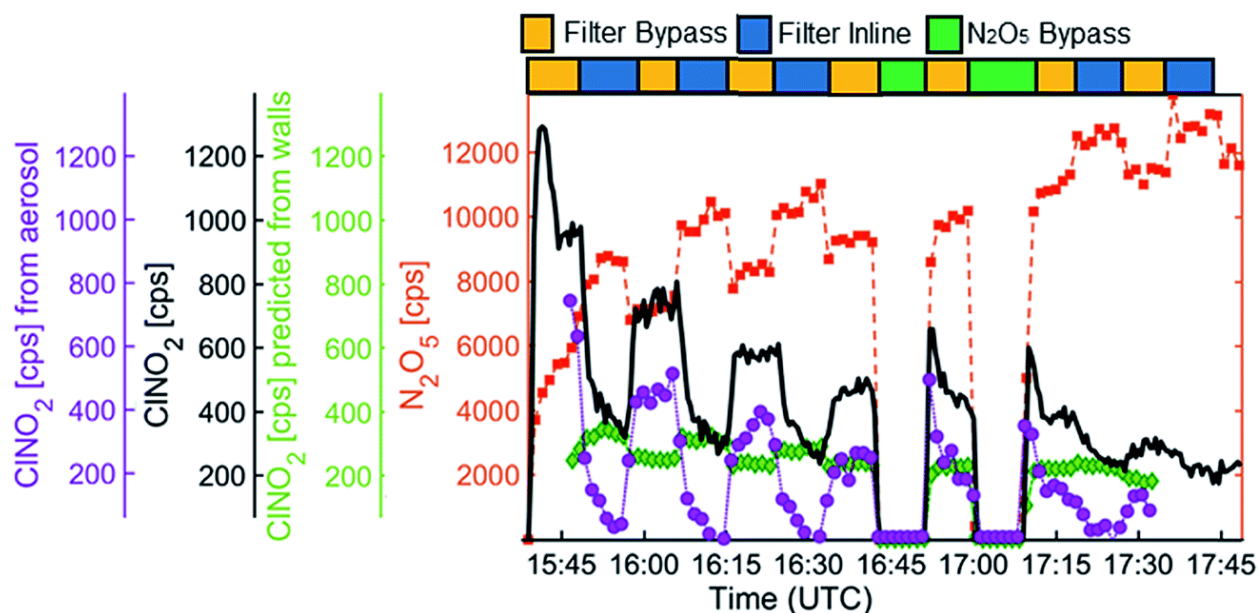
Figure 3-5. Experimental timeline from N_2O_5 reactive uptake experiment on black needlerush BBA at 75% RH. When N_2O_5 is present in the flow reactor (blue and yellow bar periods along top of figure), there is observed $ClNO_2(g)$ (black trace). Even while BBA is filtered out (filter inline, blue bars) there is some $ClNO_2$ measured, suggesting that some is produced from N_2O_5 reacting on the walls and transfer tubing. This wall-produced $ClNO_2$ (green diamonds) is estimated from the times when BBA is filtered. The difference between the total $ClNO_2$ and wall-produced $ClNO_2$ is then the $ClNO_2$ produced from BBA (purple circles). $ClNO_2$ (ppt) concentrations can be converted from the measured counts per second (cps) by dividing by 3.5, and N_2O_5 (ppt) by dividing the counts per second by 7. The lack of $ClNO_2$ detected during the N_2O_5 bypass period (green bars) when N_2O_5 was not added indicates that the $ClNO_2$ was indeed forming in particles following the reactive uptake of N_2O_5. Reproduced from Goldberger et al. (2019).

3.4.4 Reactive nitrogen budget

By examining all measurable gas- and particle-phase nitrogen oxide species, a reactive nitrogen budget can be created to balance the reactive nitrogen lost from N_2O_5 reactive uptake with the major possible products, gaseous or particulate HNO_3, and $ClNO_2$. This can be evaluated using Equation 7:

$$\text{Nitrogen Balance} = 2\Delta N_2O_5 - (\Delta HNO_3(g) + \Delta ClNO_2 + \Delta pNO_3) \qquad (E7)$$

For each N_2O_5 molecule that reacts on a particle, two N are converted into products – HNO_3, $ClNO_2$, pNO_3, or other unmeasured products. If the nitrogen balance is equal to zero, this implies a closure in that all reacted N_2O_5 is accounted for by one of these three products. Positive values mean that not all the products were accounted for, while negative values mean there was an excess of measured products.

Table 3-3 contains a summary of the calculated nitrogen balance for each experiment. Most resulted in a nitrogen balance within ± 50%, which is reasonable given all the instrumental measurement uncertainties involved. The best nitrogen balance was in the low RH saw palmetto experiment, where 44% of N_2O_5 resulted in HNO_3/$ClNO_2$(g) and 52% resulted in pNO_3, leaving just 4% unaccounted for. The worst nitrogen balance was the black needlerush at high RH experiment that had an excess of pNO_3 an order of magnitude higher than that of experiments with similar changes in N_2O_5, possibly because this experiment had one of the highest relative humidities used of 75%.

3.4.5 γ(N_2O_5) literature comparison

The N_2O_5 reaction probability values calculated for these biomass-burning aerosol UW-flow tube experiments, ranging from 0.002-0.006, fit within the range of previous literature values of many ambient and laboratory aerosol studies, see Figure 3-6. As this is the first work to study γ(N_2O_5) on authentic BBA we cannot compare our values to others, but we can examine similar types of aerosol particles. For example, a large component of BBA is black carbon, or soot, and γ(N_2O_5) on soot aerosol has been reported to be 2×10^{-4} – 0.03 (Karagulian et al., 2006). The ambient aerosol studied in semi-rural China (Tham et al., rightmost on Fig. 3-6) was influenced by biomass burning, but had γ(N_2O_5) values of 0.005–0.039, mostly higher compared to ours (Tham et al., 2018). One kinetics study on aerosol composed of pure organic components present in BBA (e.g. levoglucosan, abietic acid, 5-nitroguaiacol) under dry conditions resulted in much lower γ(N_2O_5) values of $4–6 \times 10^{-5}$ (Knopf et al., 2011). Other mixed organic/inorganic aerosol

particles have been studied, finding $\gamma(N_2O_5)$ for humic acid (6% and 40% by mass) mixed with aqueous ammonium sulfate was 3×10^{-4} and 8×10^{-3}, respectively, and $\gamma(N_2O_5)$ for particles with organic mass fractions from ~0 to 50% ranged from 0.003 to 0.025 (Badger et al., 2006; Gaston et al., 2014).
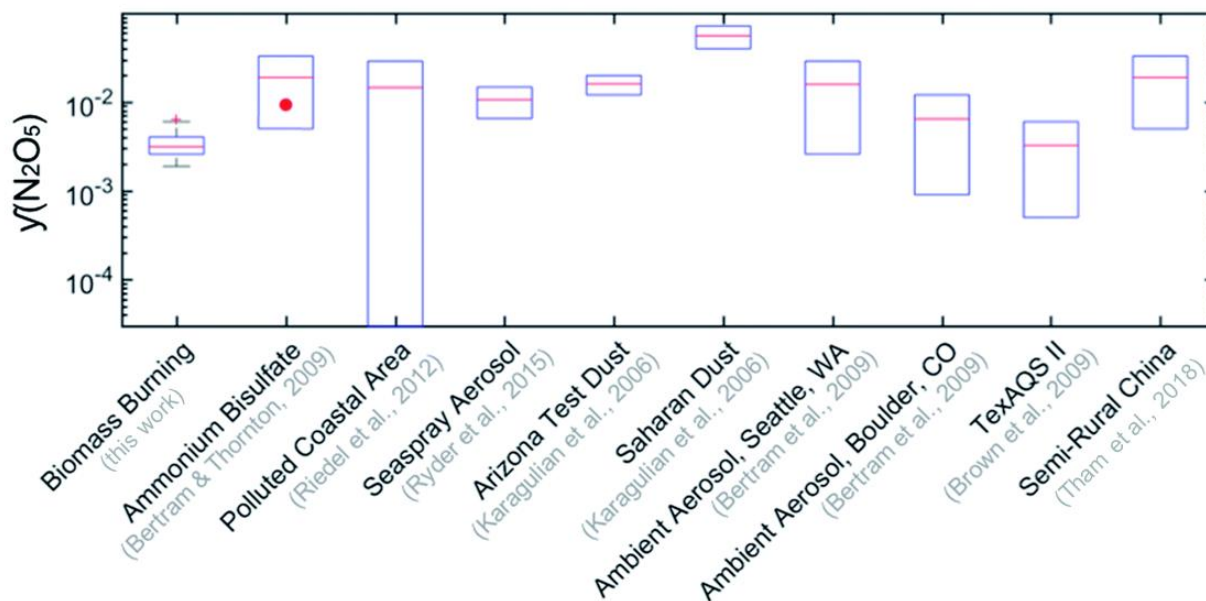
Figure 3-6. N_2O_5 reactive uptake values from these experiments at ~35% and ~70% RH ("biomass burning") compared to previous literature values of other aerosol types including ambient aerosol. The BBA values are within the lower end of the ranges reported for other aerosol, and the ammonium bisulfate control measured here (red circle) is also within literature values, validating our experimental system (Bertram et al., 2009b; Bertram and Thornton, 2009; Brown et al., 2009; Karagulian et al., 2006; Riedel et al., 2012; Ryder et al., 2015; Tham et al., 2018). Modified from Goldberger et al. (2019).

Previous studies found that organic coatings decrease the reactive uptake of N_2O_5 on particles (Anttila et al., 2006; Gaston et al., 2014; McNeill et al., 2006; Ryder et al., 2014, 2015). Electron microscopy of BBA from several biomass fuels revealed that many particles did indeed contain organic coatings that concealed inorganic salt phases (Figure 3-7). We unfortunately were not able to obtain TEM/EDX analysis of BBA from the same fuels used in these kinetics experiments, however given our extensive microscopy analysis on other BBA samples produced

from similar fuels, and previous research on chloride salts in BBA, we expect the similar particle morphologies to be present (Levin et al., 2010; Jahn et al., 2020). Such organic coatings prevalent in BBA would explain the lower $\gamma(N_2O_5)$ values even in high-chloride fuels. Similarly, conducting these experiments below the deliquescence relative humidities of chloride salts does not allow for the presence of accessible aqueous chloride phases that drive N_2O_5 hydrolysis, increase $\gamma(N_2O_5)$, and also promote the yield of $ClNO_2$.
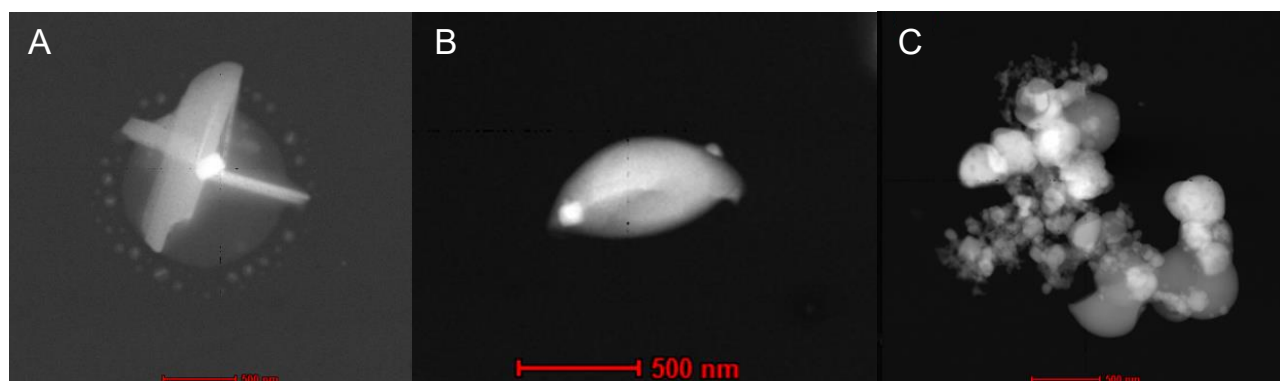
Figure 3-7. Transmission electron microscopy (TEM) images of biomass-burning aerosol collected on copper TEM grids. **A)** is from ponderosa pine needle BBA; the bright white spot is KCl and is surrounded by a liquid-like organic puddle which likely partially evaporated in the vacuum chamber of the TEM. **B)** is from sawgrass BBA; the bright white spot is KCl and the rest of the particle is organic aerosol. **C)** is from cutgrass BBA and is an aggregate of chloride salts (bright spots), organic carbon, and graphitic soot. These are the types of organic aerosol coatings that would limit the ability of N_2O_5 to access chloride salts. More details can be found in Jahn et al. (2020).

3.4.6 $\gamma(N_2O_5)$ over deliquescence relative humidity

In order to determine whether or not the solid phase state of the chloride salts in the BBA was limiting N_2O_5 uptake, additional experiments were conducted at higher relative humidities using the CMU-flow tube. Moist clean air was mixed with the BBA in a conditioning tube prior to the kinetics flow tube such that the aerosol flow into the flow reactor was brought to 86%, above the deliquescence relative humidity of chloride salts common to biomass-burning aerosol (Seinfeld and Pandis, 1998; Freney et al., 2009; Li et al., 2014). A Nafion drier was used to slightly dry the aerosol before entering the flow tube to limit wall effects and to ensure the instruments

sampling from the end of the flow tube could operate properly, but this RH was still maintained at RH > 60%, above the efflorescence relative humidity of chloride salts. We found that at very high RH of 86%, $\gamma(N_2O_5)$ increased substantially in BBA from high chloride fuels and remained relatively constant in BBA from low chloride fuels (Table 3-4). Figure 3-8 shows the N_2O_5 reactive uptake coefficient measured for BBA from both the UW- and CMU-flow tube experiments, colored by relative humidity; the fuels are in order of increasing pCl from left to right.

Table 3-4. Reactive uptake coefficients of N_2O_5 on each of the previously used biomass fuels, but after they had been exposed to relative humidities above the DRH of chloride salts.

BBA fuel type	RH (%) pre-flow tube [a]	RH (%) in flow tube [b]	$\gamma(N_2O_5)$ $(2\sigma) \times 10^{-3}$
LL Pine Needles	86	61	3.4 (1)
Wiregrass	86	73	5.4 (1)
Saw palmetto	86	74	7.2 (2)
Black needlerush	86	62	16 (2)

[a] *RH pre-flow tube* is the RH of the conditioning line where the aerosol was present for several seconds before entering the kinetics flow tube.
[b] *RH in flow tube* is the RH measured at the exit port of the kinetics flow tube.

The substantial changes in N_2O_5 reactive uptake in high-chloride BBA that only occurred at 86% RH are supported by environmental SEM analysis of black needlerush BBA. BBA was collected from the smog chamber onto grids, which were imaged as the relative humidity within the SEM chamber was increased from 1% – 97% (Figure 3-9). Particles do not begin to take up water until 69% RH, with substantial changes in size and morphology not appearing until 80% RH. These observations are consistent with the deliquescence relative humidities of chloride salts being near 80%, and similar behavior was observed in particles on different areas of the grid, as shown in Figures 3-10 – 3-11.
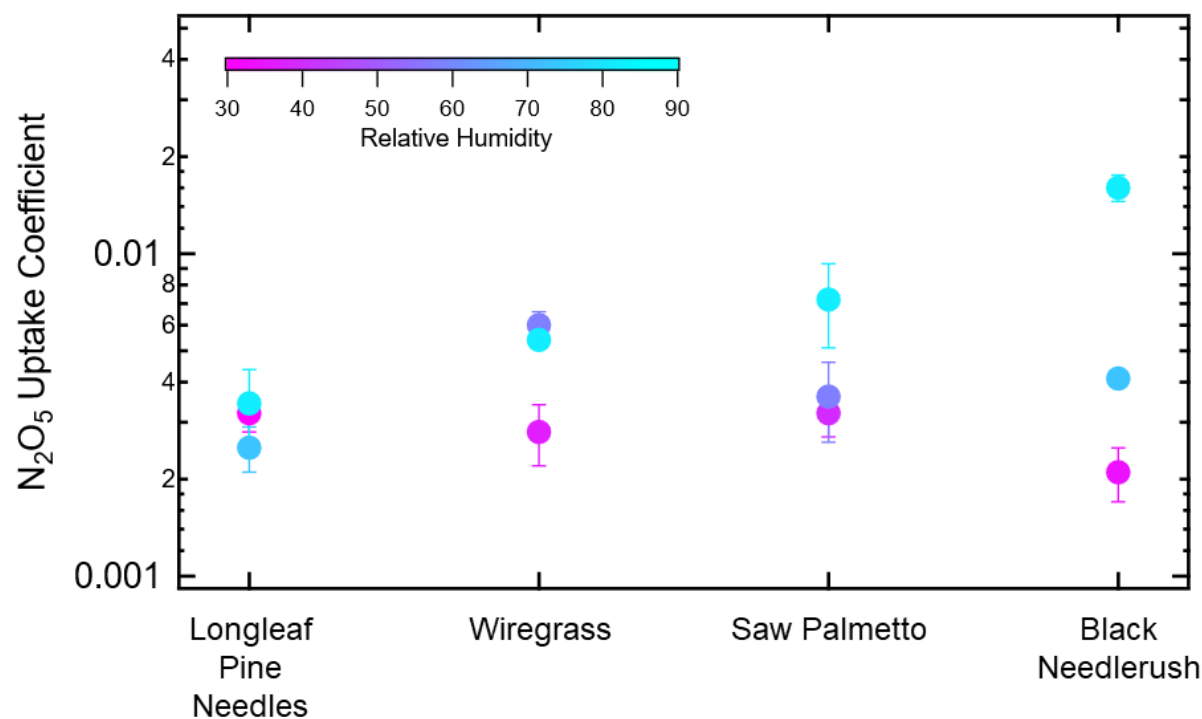
Figure 3-8. Reactive uptake coefficients of N_2O_5 for all biomass fuel types across all three relative humidities tested in both the UW-flow tube and CMU-flow tube. The two high-chloride fuels, saw palmetto and black needlerush, exhibit much larger changes in $\gamma(N_2O_5)$ when increasing from ~70% RH to 86% RH compared to the low-chloride fuels, longleaf pine needles and wiregrass. Symbols are colored based on the maximum relative humidity the BBA was exposed to in the conditioning line just prior to entering the kinetics flow tube.
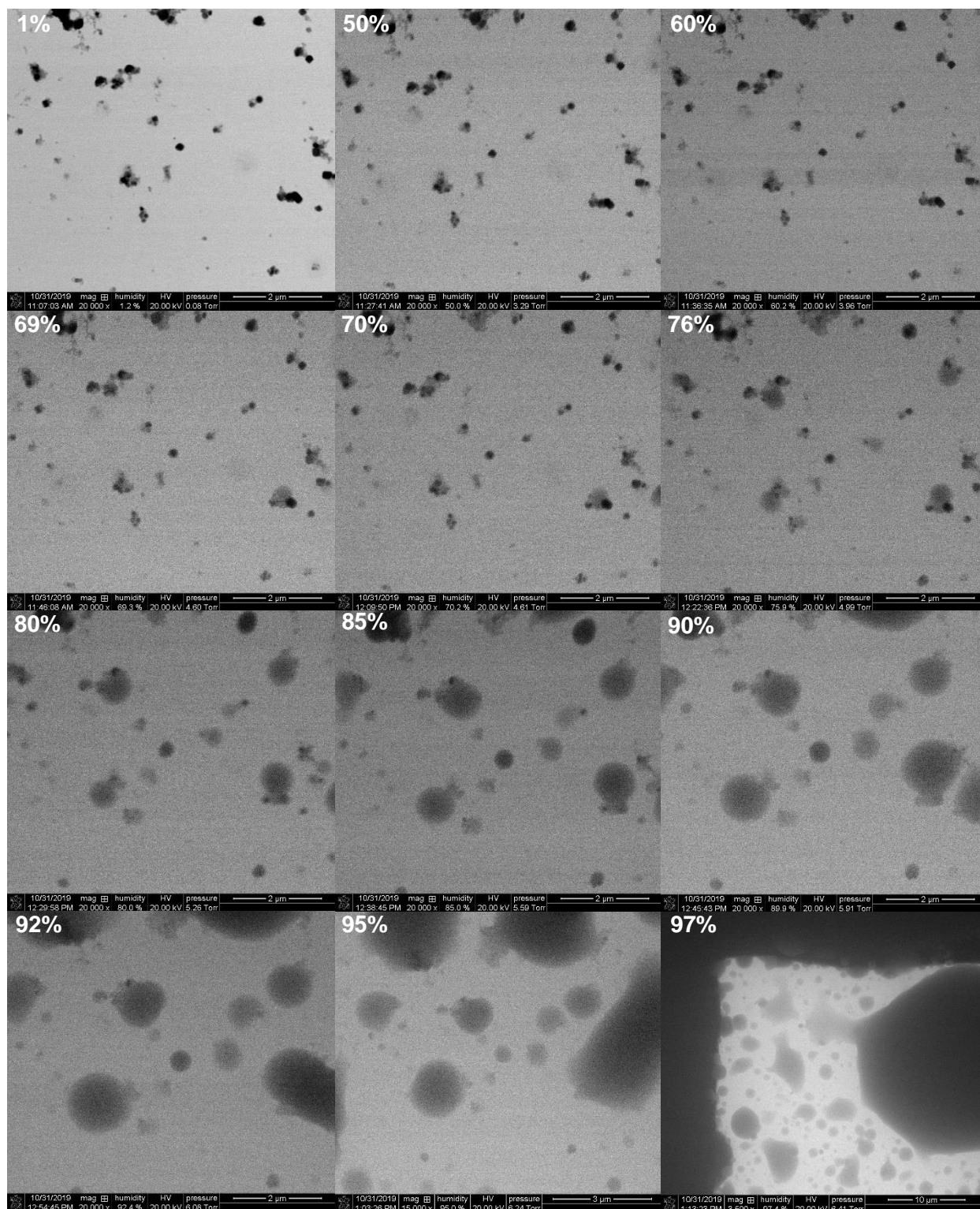
Figure 3-9. Environmental SEM images of black needlerush BBA on a grid throughout a relative humidity ramp from 1% to 97%. Large changes in particle size and morphology are only observed near 80% RH, indicating substantial water uptake and hygroscopic growth, likely driven by inorganic salt deliquescence.

90
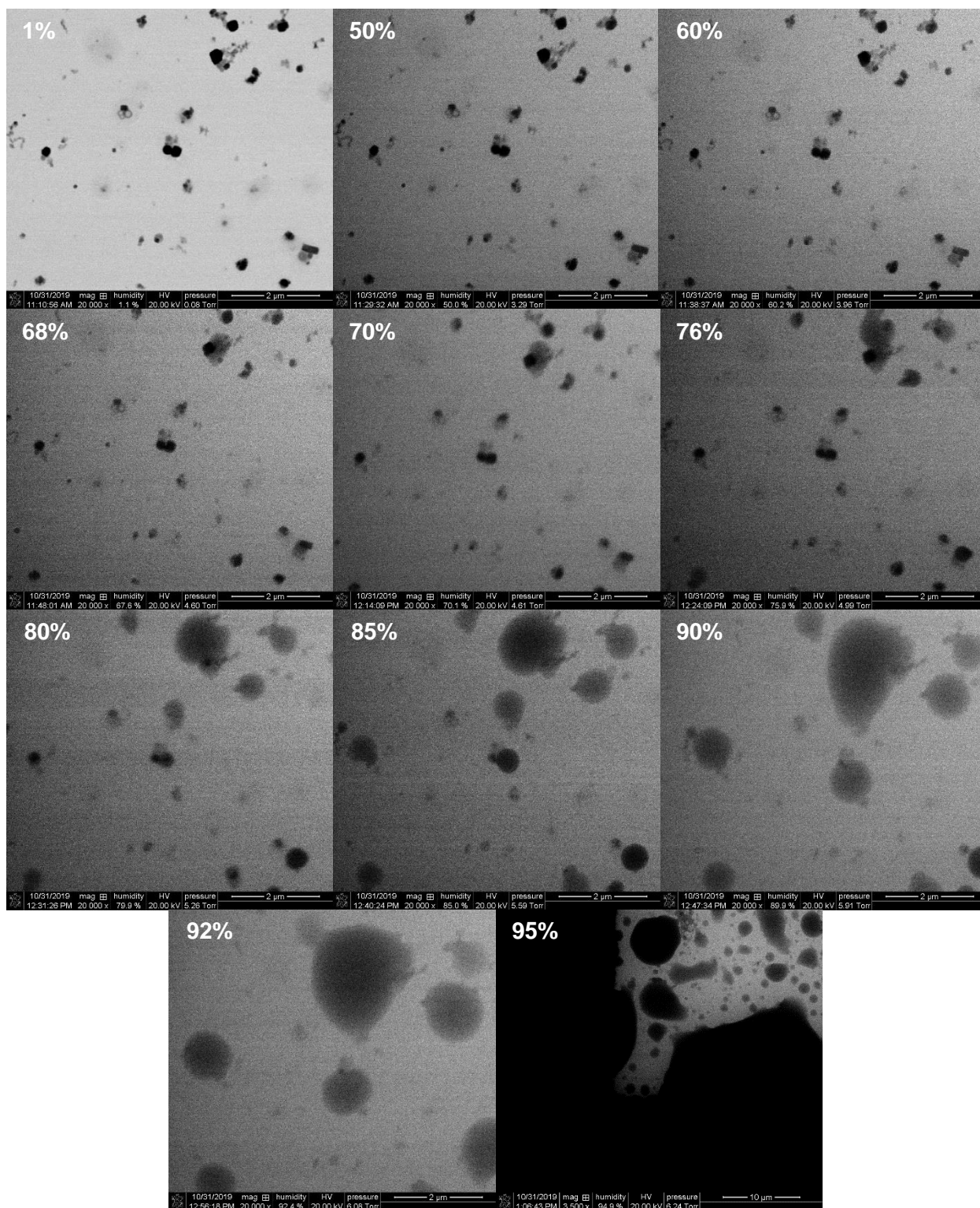
Figure 3-10. Additional environmental SEM images of black needlerush BBA as it is exposed to increasing RH levels – a second area of the grid.
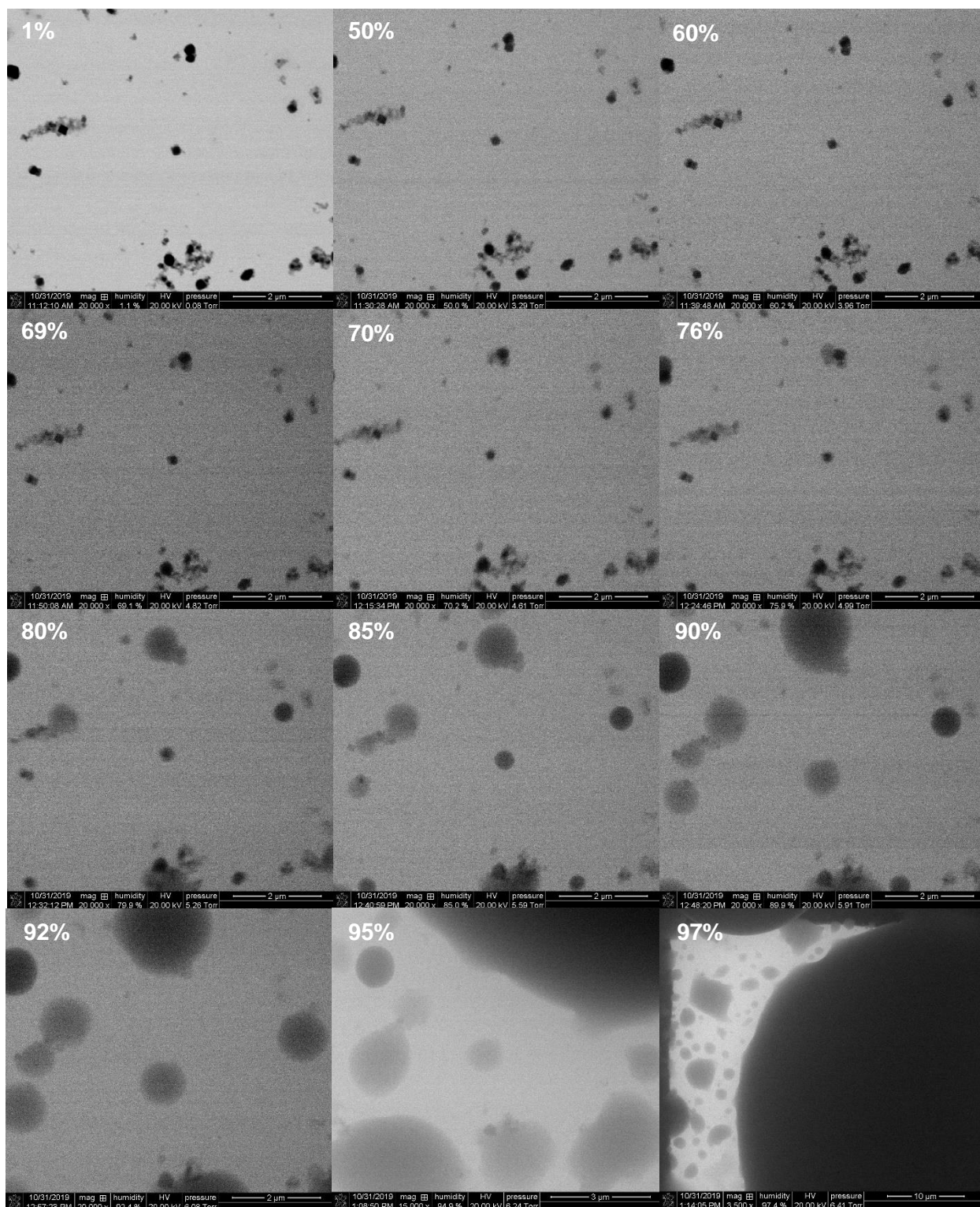
Figure 3-11. Additional environmental SEM images of black needlerush BBA as it is exposed to increasing RH levels – a third area of the grid.

3.5 Discussion

The $ClNO_2$ yields observed vary greatly amongst the different biomass fuels. The fuels with high chloride content should promote the production of more $ClNO_2$, but factors such as particle morphology and phase state may limit $ClNO_2$ production in all experiments. Saw palmetto has chloride content comparable to black needlerush (Table 3-1) but a much lower $\varphi(ClNO_2)$ of < 1% rather than ~50% determined for black needlerush (Table 3-2). The $ClNO_2$ yield likely depends on how accessible the chloride salts in each BBA system are. For example, if saw palmetto BBA is more likely to have viscous organic aerosol or tar balls coating and concealing its chloride salt phases, then this would inhibit the reaction of the aqueous nitrogenated intermediate $H_2ONO_2^+$ with chloride to form $ClNO_2$. TEM/EDX analysis of several other types of BBA revealed that soot and salts of some types of biomass fuels are coated in a stable organic coating (i.e. one that did not decompose during exposure to the electron beam or evaporate under vacuum), while others appeared to have more liquid-like organic coatings that partially evaporated under vacuum (Jahn et al., 2020). Additional microscopy of the specific fuels used in this work would be needed to determine if such morphology is playing a role in $\varphi(ClNO_2)$ differences here.

The relative humidity and phase state also likely pay a large role in determining $ClNO_2$ yields. KCl and NH_4Cl are two of the most common chloride salts emitted in BBA, and KCl phases do not deliquesce until 85% RH (Hu and Abbatt, 1997; Levin et al., 2010; Thornton et al., 2003). In internally mixed particles such as BBA, solid KCl may even be present up to 82% RH (Freney et al., 2009). Therefore, especially at the lowest RH experiments of up to 40% performed here, it is likely that particulate chloride was in a solid effloresced state, inaccessible for the aqueous chemistry that results in rapid N_2O_5 hydrolysis as well as promoting $ClNO_2$ production. Chlorine activation from solid chloride particles has been observed, but this is a slower process and may not occur to large extents in the two-minute residence time of the aerosol in the flow tube reactor (Behnke and Zetzsch, 1989; Finlayson-Pitts et al., 1989).

In our previous experiments that demonstrated N_2O_5 and $ClNO_2$ formation in authentic biomass-burning aerosol, higher concentrations of $ClNO_2$ correlated with the mass fraction of particulate chloride (Ahern et al., 2018). These experiments were conducted entirely in a smog chamber reactor, such that the BBA was exposed to water vapor for much longer than in the flow tube experiments presented here. While the long mixing time and chamber wall chemistry interferences did not allow for accurate calculations of the parameters $\gamma(N_2O_5)$ and $\varphi(ClNO_2)$, the only fuel type that had a measurable $ClNO_2$ yield in the prior chamber experiments was sawgrass (*Cladium jamaicense)*, which also has elevated particulate chloride levels (Ahern et al., 2018). $ClNO_2$ concentrations in those chamber experiments continued to rise even 1.5 hours after the initial formation of N_2O_5. This much longer time scale may account for the higher levels of $ClNO_2$ detected in the chamber experiments compared to the flow tube. Additionally, while the maximum average RH in the chamber experiments was only 60%, steam injection from one port was used such that localized areas of the chamber would be above 80% RH for several minutes. This would likely result in deliquesced chloride salts that do not effloresce until they are exposed to drier conditions below their efflorescence RH of < 56%, resulting in aqueous chloride phases being present that are capable of producing $ClNO_2$ (Freney et al., 2009).

As particulate chloride should directly increase $\gamma(N_2O_5)$ in aqueous inorganic particles, the lower uptake coefficients for high-chloride fuels may seem surprising (Bertram and Thornton, 2009). However, the complex composition of authentic BBA very likely affects N_2O_5 uptake. For example, particulate nitrate and organic aerosol both suppress $\gamma(N_2O_5)$ and are often present at high mass fractions in BBA (Anttila et al., 2006; Escorcia et al., 2010; Gaston et al., 2014; Levin et al., 2010; Mentel et al., 1999; Ryder et al., 2014; Wahner et al., 1998). These competing effects depend on the exact particle morphology, and single-particle experiments have shown that at oxidation states similar to the BBA here, the organic and aqueous phases can separate into a core-shell morphology with the organic phase forming a shell around the aqueous inorganic phase

(Gorkowski et al., 2020). Only high-chloride fuels exhibited a large increase in $\gamma(N_2O_5)$ when exposed to relative humidities above the DRH of chloride salts, suggesting that the solid phase state of chloride at low relative humidities limits reactive uptake of N_2O_5. In low-chloride fuels, $\gamma(N_2O_5)$ seems to be limited by other factors such as organic coatings that cover the aerosol surface. This would explain why the N_2O_5 reaction probability remains relatively the same for the low-chloride fuels when the RH was raised above the DRH of chloride salts.

3.6 Conclusions and atmospheric implications

This work is the first to report the N_2O_5 reactive uptake probability ($\gamma(N_2O_5)$) on authentic biomass-burning aerosol from entrained aerosol flow reactor experiments at different relative humidities. $\gamma(N_2O_5)$ varied from 0.002–0.006 at relative humidities < 75% and from 0.0034–0.016 at 86% RH, within the range of the somewhat comparable laboratory and ambient systems previously reported. Trends usually observed in aqueous inorganic aerosol where higher pCl increases $\gamma(N_2O_5)$ while increased pNO_3 decreases $\gamma(N_2O_5)$ were not observed here, while in most cases an increase in relative humidity did increase $\gamma(N_2O_5)$ as expected. Out of four types of BBA at relative humidities of ~35% and ~70%, only black needlerush at 76% RH resulted in a significant $ClNO_2$ yield ($\varphi(ClNO_2)$). Both of these observations are likely due to complex BBA composition, morphology, and water content that limit the reaction of N_2O_5 with particulate aqueous chloride.

Our higher N_2O_5 reaction probability results obtained at 86% RH suggest that N_2O_5 uptake and $ClNO_2$ production are limited at lower RH due to the solid phase state of chloride salts and the particle morphology via organic coatings that restrict heterogeneous reactions between N_2O_5 and chloride. We therefore encourage further study of N_2O_5 heterogeneous kinetics on the most realistic aerosol possible rather than simplified or proxy systems that cannot reproduce these important effects. Relative humidities higher than at least 80% are likely necessary to substantially increase $\gamma(N_2O_5)$ only in high-chloride fuels, and biomass chloride content may not affect $\gamma(N_2O_5)$

at lower relative humidities. $ClNO_2$ formation depends on both relative humidity and biomass chloride content, but reaction times greater than 30 minutes are likely necessary for substantial $ClNO_2$ production in BBA. This will require tracking the life cycle and RH history of BBA to know if the chloride salt phases are in the deliquesced or effloresced branches in order to properly include the kinetics and $ClNO_2$ yield into atmospheric chemical transport models.

3.7   Acknowledgements

3.8   References

Abbatt, J. P. D., Lee, A. K. Y. and Thornton, J. A.: Quantifying trace gas uptake to tropospheric aerosol: Recent advances and remaining challenges, Chem. Soc. Rev., 41(19), 6555–6581, doi:10.1039/c2cs35052a, 2012.

Ahern, A. T., Subramanian, R., Saliba, G., Lipsky, E. M., Donahue, N. M. and Sullivan, R. C.: Effect of secondary organic aerosol coating thickness on the real-time detection and characterization of biomass-burning soot by two particle mass spectrometers, Atmos. Meas. Tech, 9, 6117–6137, doi:10.5194/amt-9-6117-2016, 2016.

Ahern, A. T., Goldberger, L., Jahl, L., Thornton, J. and Sullivan, R. C.: Production of N2O5 and ClNO2 through Nocturnal Processing of Biomass-Burning Aerosol, , 52(2), 550–559, doi:10.1021/acs.est.7b04386, 2018.

Anttila, T., Kiendler-Scharr, A., Tillmann, R. and Mentel, T. F.: On the Reactive Uptake of Gaseous Compounds by Organic-Coated Aqueous Aerosols: Theoretical Analysis and Application to the Heterogeneous Hydrolysis of N2O5, J. Phys. Chem. A, 110(35), 10435–10443, doi:10.1021/jp062403c, 2006.

Badger, C. L., Griffiths, P. T., George, I., Abbatt, J. P. D. and Cox, R. A.: Reactive uptake of N2O5 by aerosol particles containing mixtures of humic acid and ammonium sulfate, J. Phys. Chem. A, 110(21), 6986–6994, doi:10.1021/jp0562678, 2006.

Bannan, T. J., Khan, M. A. H., Le Breton, M., Priestley, M., Worrall, S. D., Bacak, A., Marsden, N. A., Lowe, D., Pitt, J., Allen, G., Topping, D., Coe, H., McFiggans, G., Shallcross, D. E. and Percival, C. J.: A Large Source of Atomic Chlorine From ClNO2 Photolysis at a U.K. Landfill Site, Geophys. Res. Lett., 46(14), 2019GL083764, doi:10.1029/2019GL083764, 2019.

Behnke, W. and Zetzsch, C.: Heterogeneous formation of chlorine atoms from various aerosols in the presence of O3 and HCl, J. Aerosol Sci., 20(8), 1167–1170, doi:10.1016/0021-8502(89)90788-X, 1989.

Bertram, T. H. and Thornton, J. A.: Toward a general parameterization of N2O5 reactivity on aqueous particles: The competing effects of particle liquid water, nitrate and chloride, Atmos. Chem. Phys., 9(21), 8351–8363, doi:10.5194/acp-9-8351-2009, 2009.

Bertram, T. H., Thornton, J. A. and Riedel, T. P.: An experimental technique for the direct measurement of N2O5 reactivity on ambient particles, Atmos. Meas. Tech, 2, 231–242, 2009a.

Bertram, T. H., Thornton, J. A., Riedel, T. P., Middlebrook, A. M., Bahreini, R., Bates, T. S., Quinn, P. K. and Coffman, D. J.: Direct observations of N2O5 reactivity on ambient aerosol particles, Geophys. Res. Lett., 36(19), doi:10.1029/2009GL040248, 2009b.

Brown, S. S., Dubé, W. P., Fuchs, H., Ryerson, T. B., Wollny, A. G., Brock, C. A., Bahreini, R., Middlebrook, A. M., Neuman, T. A., Atlas, E., Roberts, J. M., Osthoff, H. D., Trainer, M., Fehsenfeld, F. C. and Ravishankara, A. R.: Reactive uptake coefficients for N2O5 determined from aircraft measurements during the Second Texas Air Quality Study: Comparison to current model parameterizations, J. Geophys. Res. Atmos., 114(11), doi:10.1029/2008JD011679, 2009.

Dentener, F. J. and Crutzen, P. J.: Reaction of N2O5 on tropospheric aerosols: impact on the global distributions of NOx, O3, and OH, J. Geophys. Res., 98(D4), 7149–7163, doi:10.1029/92JD02979, 1993.

Escorcia, E. N., Sjostedt, S. J. and Abbatt, J. P. D.: Kinetics of N2O5 hydrolysis on secondary organic aerosol and mixed ammonium bisulfate-secondary organic aerosol particles, J. Phys. Chem. A, 114(50), 13113–13121, doi:10.1021/jp107721v, 2010.

Finlayson-Pitts, B. J., Ezell, M. J. and Pitts, J. N.: Formation of chemically active chlorine compounds by reactions of atmospheric NaCl particles with gaseous N2O5 and ClONO2, Nature, 337(6204), 241–244, doi:10.1038/337241a0, 1989.

Freney, E. J., Martin, S. T. and Buseck, P. R.: Deliquescence and efflorescence of potassium salts relevant to biomass-burning aerosol particles, Aerosol Sci. Technol., 43(8), 799–807, doi:10.1080/02786820902946620, 2009.

Gaston, C. J., Thornton, J. A. and Ng, N. L.: Reactive uptake of N2O5 to internally mixed inorganic and organic particles: The role of organic carbon oxidation state and inferred organic phase separations, Atmos. Chem. Phys., 14(11), 5693–5707, doi:10.5194/acp-14-5693-2014, 2014.

Gorkowski, K., Donahue, N. M. and Sullivan, R. C.: Aerosol Optical Tweezers Constrain the Morphology Evolution of Liquid-Liquid Phase-Separated Atmospheric Particles, Chem, 6(1), 204–220, doi:10.1016/j.chempr.2019.10.018, 2020.

Haskins, J. D., Lee, B. H., Lopez-Hilifiker, F. D., Peng, Q., Jaeglé, L., Reeves, J. M., Schroder, J. C., Campuzano-Jost, P., Fibiger, D., McDuffie, E. E., Jiménez, J. L., Brown, S. S. and Thornton, J. A.: Observational Constraints on the Formation of Cl2 From the Reactive Uptake of ClNO2 on Aerosols in the Polluted Marine Boundary Layer, J. Geophys. Res. Atmos., 124(15), 2019JD030627, doi:10.1029/2019JD030627, 2019.

Hu, J. H. and Abbatt, J. P. D.: Reaction Probabilities for N2O5 Hydrolysis on Sulfuric Acid and Ammonium Sulfate Aerosols at Room Temperature, J. Phys. Chem. A, 101(5), 871–878, doi:10.1021/jp9627436, 1997.

Imre, D. G., Xu, J., Tang, I. N. and Mcgraw, R.: Ammonium Bisulfate/Water Equilibrium and Metastability Phase Diagrams., 1997.

Jahn, L., Jahl, L. G., Bowers, B. and Sullivan, R. C.: Organic coatings on biomass-burning particles and their role in reactive gas uptake, Environ. Sci. Process. Impacts, To Be Submitted, 2020.

Karagulian, F., Santschi, C. and Rossi, M. J.: The heterogeneous chemical kinetics of N2O5 on CaCO3 and other atmospheric mineral dust surrogates, Atmos. Chem. Phys., 6(5), 1373–1388, doi:10.5194/acp-6-1373-2006, 2006.

Knopf, D. A., Forrester, S. M. and Slade, J. H.: Heterogeneous oxidation kinetics of organic biomass burning aerosol surrogates by O3, NO2, N2O5, and NO3, Phys. Chem. Chem. Phys., 13(47), doi:10.1039/c1cp22478f, 2011.

Lee, B. H., Lopez-Hilfiker, F. D., Mohr, C., Kurtén, T., Worsnop, D. R. and Thornton, J. A.: An iodide-adduct high-resolution time-of-flight chemical-ionization mass spectrometer: Application to atmospheric inorganic and organic compounds, Environ. Sci. Technol., 48(11), 6309–6317, doi:10.1021/es500362a, 2014.

Lee, B. H., Lopez-Hilfiker, F. D., Schroder, J. C., Campuzano-Jost, P., Jimenez, J. L., McDuffie, E. E., Fibiger, D. L., Veres, P. R., Brown, S. S., Campos, T. L., Weinheimer, A. J., Flocke, F. F., Norris, G., O'Mara, K., Green, J. R., Fiddler, M. N., Bililign, S., Shah, V., Jaeglé, L. and Thornton, J. A.: Airborne Observations of Reactive Inorganic Chlorine and Bromine Species in the Exhaust of Coal-Fired Power Plants, J. Geophys. Res. Atmos., doi:10.1029/2018JD029284, 2018.

Levin, E. J. T. T., McMeeking, G. R., Carrico, C. M., Mack, L. E., Kreidenweis, S. M., Wold, C. E., Moosmüller, H., Arnott, W. P., Hao, W. M., Collett, J. L. and Malm, W. C.: Biomass burning smoke aerosol properties measured during Fire Laboratory at Missoula Experiments (FLAME), , 115, D18210, doi:10.1029/2009JD013601, 2010.

Li, J., Pósfai, M., Hobbs, P. V. and Buseck, P. R.: Individual aerosol particles from biomass burning in southern Africa: 2, Compositions and aging of inorganic particles, J. Geophys. Res. Atmos., 108(D13), n/a-n/a, doi:10.1029/2002JD002310, 2003.

Li, X., Gupta, D., Eom, H.-J. J., Kim, H. K. and Ro, C.-U. U.: Deliquescence and efflorescence behavior of individual NaCl and KCl mixture aerosol particles, Atmos. Environ., 82, 36–43, doi:10.1016/j.atmosenv.2013.10.011, 2014.

Lobert, J. M., Keene, W. C., Logan, J. A. and Yevich, R.: Global chlorine emissions from biomass burning: Reactive Chlorine Emissions Inventory, , 104(D7), 8373–8389, doi:10.1029/1998JD100077, 1999.

McMeeking, G. R., Kreidenweis, S. M., Baker, S., Carrico, C. M., Chow, J. C., Collett, J. L., Hao, W. M., Holden, A. S., Kirchstetter, T. W., Malm, W. C., Moosmüller, H., Sullivan, A. P. and Cyle E., W.: Emissions of trace gases and aerosols during the open combustion of biomass in the laboratory, J. Geophys. Res. Atmos., 114(19), doi:10.1029/2009JD011836, 2009.

McNamara, S. M., Raso, A. R. W., Wang, S., Thanekar, S., Boone, E. J., Kolesar, K. R., Peterson, P. K., Simpson, W. R., Fuentes, J. D., Shepson, P. B. and Pratt, K. A.: Springtime nitrogen oxide-influenced chlorine chemistry in the coastal arctic, Environ. Sci. Technol., 53(14), 8057–8067,

doi:10.1021/acs.est.9b01797, 2019.

McNeill, V. F., Patterson, J., Wolfe, G. M. and Thornton, J. A.: The Effect of Varying Levels of Surfactant on the Reactive Uptake of N2O5 to Aqueous Aerosol, Atmos. Chem. Phys., 6(6), 1635–1644, doi:10.5194/acp-6-1635-2006, 2006.

Mentel, T. F., Sohn, M. and Wahner, A.: Nitrate effect in the heterogeneous hydrolysis of dinitrogen pentoxide on aqueous aerosols, Phys. Chem. Chem. Phys., 1(24), 5451–5457, doi:10.1039/a905338g, 1999.

Mielke, L. H., Furgeson, A. and Osthoff, H. D.: Observation of ClNO2 in a mid-continental urban environment, Environ. Sci. Technol., 45(20), 8889–8896, doi:10.1021/es201955u, 2011.

Pósfai, M., Simonics, R., Li, J., Hobbs, P. V. and Buseck, P. R.: Individual aerosol particles from biomass burning in southern Africa: 1. Compositions and size distributions of carbonaceous particles, J. Geophys. Res. Atmos., 108(D13), n/a-n/a, doi:10.1029/2002JD002291, 2003.

Reid, J. S., Koppmann, R., Eck, T. F. and Eleuterio, D. P.: A review of biomass burning emissions part II: Intensive physical properties of biomass burning particles, Atmos. Chem. Phys., 5(3), 799–825, doi:10.5194/acp-5-799-2005, 2005.

Riedel, T. P., Bertram, T. H., Ryder, O. S., Liu, S., Day, D. A., Russell, L. M., Gaston, C. J., Prather, K. A. and Thornton, J. A.: Direct N2O5 reactivity measurements at a polluted coastal site, Atmos. Chem. Phys., 12(6), 2959–2968, doi:10.5194/acp-12-2959-2012, 2012.

Riedel, T. P., Wagner, N. L., Dubé, W. P., Middlebrook, A. M., Young, C. J., Öztürk, F., Bahreini, R., VandenBoer, T. C., Wolfe, D. E., Williams, E. J., Roberts, J. M., Brown, S. S. and Thornton, J. A.: Chlorine activation within urban or power plant plumes: Vertically resolved ClNO2 and Cl2 measurements from a tall tower in a polluted continental setting, J. Geophys. Res. Atmos., 118(15), 8702–8715, doi:10.1002/jgrd.50637, 2013.

Riedel, T. P., Wolfe, G. M., Danas, K. T., Gilman, J. B., Kuster, W. C., Bon, D. M., Vlasenko, A., Williams, E. J., Lerner, B. M., Veres, P. R., Roberts, J. M., Holloway, J. S., Lefer, B., Brown, S. S. and Thornton, J. A.: An MCM modeling study of nitryl chloride (ClNO2) impacts on oxidation, ozone production and nitrogen oxide partitioning in polluted continental outflow, Atmos. Chem. Phys., 14(8), 3789–3800, doi:10.5194/acp-14-3789-2014, 2014.

Roberts, J. M., Osthoff, H. D., Brown, S. S., Ravishankara, A. R., Coffman, D., Quinn, P. and Bates, T.: Laboratory studies of products of N2O5 uptake on Cl- containing substrates, Geophys. Res. Lett., doi:10.1029/2009GL040448, 2009.

Ryder, O. S., Ault, A. P., Cahill, J. F., Guasco, T. L., Riedel, T. P., Cuadra-Rodriguez, L. A., Gaston, C. J., Fitzgerald, E., Lee, C., Prather, K. A. and Bertram, T. H.: On the role of particle inorganic mixing state in the reactive uptake of N2O5 to ambient aerosol particles, Environ. Sci. Technol., 48(3), 1618–1627, doi:10.1021/es4042622, 2014.

Ryder, O. S., Campbell, N. R., Morris, H., Forestieri, S., Ruppel, M. J., Cappa, C., Tivanski, A., Prather, K. and Bertram, T. H.: Role of Organic Coatings in Regulating N2O5 Reactive Uptake to Sea Spray Aerosol, J. Phys. Chem. A, 119(48), 11683–11692, doi:10.1021/acs.jpca.5b08892, 2015.

Sarwar, G., Simon, H., Xing, J. and Mathur, R.: Importance of tropospheric ClNO2 chemistry across the Northern Hemisphere, Geophys. Res. Lett., 41(11), 4050–4058, doi:10.1002/2014GL059962, 2014.

Seinfeld, J. H. and Pandis, S. N.: Atmospheric Chemistry and Physics: From Air Pollution to

Climate Change, Wiley., 1998.

Tereszchuk, K. A., González Abad, G., Clerbaux, C., Hurtmans, D., Coheur, P.-F. and Bernath, P. F.: ACE-FTS measurements of trace species in the characterization of biomass burning plumes, Atmos. Chem. Phys. Atmos. Chem. Phys., 11, 12169–12179, doi:10.5194/acp-11-12169-2011, 2011.

Tham, Y. J., Wang, Z., Li, Q., Yun, H., Wang, W., Wang, X., Xue, L., Lu, K., Ma, N., Bohn, B., Li, X., Kecorius, S., Größ, J., Shao, M., Wiedensohler, A., Zhang, Y. and Wang, T.: Significant concentrations of nitryl chloride sustained in the morning: investigations of the causes and impacts on ozone production in a polluted region of northern China, Atmos. Chem. Phys, 16, 14959–14977, doi:10.5194/acp-16-14959-2016, 2016.

Tham, Y. J., Wang, Z., Li, Q., Wang, W., Wang, X., Lu, K., Ma, N., Yan, C., Kecorius, S., Wiedensohler, A., Zhang, Y. and Wang, T.: Heterogeneous N2O5 uptake coefficient and production yield of ClNO2 in polluted northern China: roles of aerosol water content and chemical composition, Atmos. Chem. Phys., 18(17), 13155–13171, doi:10.5194/acp-18-13155-2018, 2018.

Thornton, J. A. and Abbatt, J. P. D.: N2O5 reaction on submicron sea salt aerosol: Kinetics, products, and the effect of surface active organics, J. Phys. Chem. A, 109(44), 10004–10012, doi:10.1021/jp054183t, 2005.

Thornton, J. A., Braban, C. F. and Abbatt, J. P. D.: N2O5 hydrolysis on sub-micron organic aerosols: The effect of relative humidity, particle phase, and particle size, Phys. Chem. Chem. Phys., 5(20), 4593–4603, doi:10.1039/b307498f, 2003.

Thornton, J. A., Kercher, J. P., Riedel, T. P., Wagner, N. L., Cozic, J., Holloway, J. S., Dubé, W. P., Wolfe, G. M., Quinn, P. K., Middlebrook, A. M., Alexander, B., Brown, S. S., Dub́, W. P., Wolfe, G. M., Quinn, P. K., Middlebrook, A. M., Alexander, B. and Brown, S. S.: A large atomic chlorine source inferred from mid-continental reactive nitrogen chemistry, Nature, 464(7286), 271–274, doi:10.1038/nature08905, 2010.

Wahner, A., Mentel, T. F., Sohn, M. and Stier, J.: Heterogeneous reaction of N2O5 on sodium nitrate aerosol, J. Geophys. Res. Atmos., 103(D23), 31103–31112, doi:10.1029/1998JD100022, 1998.

4 Chemical Composition and Mixing State of Ambient Aerosol in the Southern Great Plains Determined Using Mass Spectrometry

4.1 Abstract

As part of the Aerosol-Ice Formation Closure Pilot Study, mass spectrometry measurements of the ambient aerosol were collected throughout October 2019 at the DOE Atmospheric Radiation Measurement program's Southern Great Plains facility by a high-resolution aerosol mass spectrometer (AMS) and a laser ablation aerosol particle time-of-flight mass spectrometer (LAAPTOF). These measurements can be incorporated into ice nucleation parameterizations to see whether the addition of particle chemical composition improves the closure between modeled predictions and measured ice nucleating particle concentrations. Submicron particulate matter analyzed by the AMS was largely organic aerosol for the duration of the campaign and had some indications of biomass burning influence. The mean chemical composition by mass consisted of organic aerosol (69%), sulfate (18%), nitrate (6%), ammonium (6%), and chloride (< 1%), and composition-based aerosol size distributions revealed that the particles were well-mixed in general. Comparisons to the facility's aerosol chemical speciation monitor revealed differences in organic aerosol up to 40% and differences in inorganic species up to 100%. Single-particle analysis using the LAAPTOF classified most particles as mineral-organic or mineral-organic-inorganic mixtures, with smaller number concentrations of mineral-inorganic mixtures, pure inorganic particles, and very small concentrations of mostly organic particles. Overall, this continental background site had low concentrations of particulate matter that was mostly well-mixed.

4.2 Introduction

Atmospheric particulate matter (PM) has deleterious effects on our climate and on human health (Apte et al., 2018; Fuzzi et al., 2015; Pope et al., 2009). Knowing aerosol particle properties

such as size, composition, and their ability to form cloud droplets or nucleate ice allows scientists and policymakers to more fully understand the impacts of aerosols on the atmospheric and climate systems, and how to mitigate these deleterious effects. Studying regions that experience significant air pollution, such as high-density cities or wildfire events, is clearly important as these sources emit vast quantities of particulate matter and pollutant gases into our atmosphere. However, studying aerosol particles in areas without large point sources of pollution that represent the continental background atmosphere is also important for learning about aerosol transport and transformation and for estimating how important properties of the atmosphere have changed with increasing anthropogenic influences.

The United States Department of Energy's Atmospheric Radiation Measurement (ARM) Southern Great Plains (SGP) atmospheric observatory is located in one such rural background region. SGP is located near Lamont, Oklahoma in the south-central United States and is the largest permanent climate measurement facility in the United States and a well-known continental background site with a long continuous measurement record. A main driving force behind the creation of the ARM program was to better understand the influence of clouds on radiative forcing and the Earth's energy budget, which remains an important area of research with significant uncertainties and knowledge gaps to this day (IPCC, 2014; Stokes and Schwartz, 1994). Long-term measurements from a wide variety of radar sensors and other instrumentation at SGP allows for a more comprehensive understanding of aerosol properties, cloud microphysics, and meteorology and how these change across time (Marinescu et al., 2019; Parworth et al., 2015; Zhang et al., 2020). The SGP site also supports visiting scientists who bring their own additional instrumentation for more in-depth research campaigns on specific topics and questions (e.g. Fast et al., 2019; Hodshire et al., 2016). There is a lack of research-grade ground-based particle mass spectrometer measurements conducted at SGP. Permanent instrumentation does include an aerosol chemical speciation monitor (ACSM)—similar to a high-resolution time-of-flight aerosol

mass spectrometer (HR-ToF-AMS, abbreviated as AMS) but with lower ion resolution—that has offered valuable long-term aerosol chemical composition measurements at SGP (Ng et al., 2011a; Parworth et al., 2015). In this work, we obtained less common high-resolution data using a HR-ToF-AMS and a single-particle mass spectrometer, the laser ablation aerosol particle time-of-flight mass spectrometer (LAAPTOF).

The data presented here were collected during the Aerosol-Ice Formation Closure Pilot Study, which took place at SGP in October 2019. The goal of this campaign was to measure the concentration and ice-nucleating activity of ambient ice nucleating particles (INPs) while measuring the particle size distributions and chemical composition of the ambient aerosol. These aerosol properties can then be input into several different ice nucleation parameterizations to predict INP concentrations, and the outputs of these models can be compared to the INP concentrations measured by several groups using different techniques throughout the campaign. This type of closure study has been conducted for other important aerosol properties such as cloud condensation nuclei activity and optical properties, but no closure studies have been conducted for ice nucleating particles that include aerosol composition and mixing state as a model input (Broekhuizen et al., 2006; Lance et al., 2009; Martin et al., 2011). The Aerosol-Ice Formation Closure Pilot Study sought to use this closure exercise to identify the most accurate ice nucleation parameterizations to include in cloud and climate models, which will improve the ability of these models to simulate the Earth's energy balance (DeMott et al., 2010; Hoose et al., 2010; Seinfeld et al., 2016). This exercise also tests our more fundamental understanding of heterogeneous ice nucleation and what particle properties drive ice-nucleating activity. The mass spectrometers used here provided much of the aerosol chemical composition data needed to inform the INP predictions. They also provide even more detailed information, discussed here, about ambient aerosol at a continental background site that has previously been obtained at the SGP measurement facility.

4.3 Experimental methods

4.3.1 Sampling location

All data presented were collected at the DOE ARM Southern Great Plains central facility in north central Oklahoma (latitude of 36.6054, longitude of -97.4857). The surrounding area is very rural and largely agricultural, with both open pastureland and cropland growing winter wheat, soybeans, cotton, corn, sorghum, and hay. The only cities nearby with populations exceeding 400,000 are Wichita, Kansas (~120 km north), Tulsa, Oklahoma (~140 km southeast), and Oklahoma City (~130 km south) (Figure 4-1). Other nearby sources of anthropogenic pollution include a coal-fired power plant (40 km southeast) and an oil refinery (40 km east).

Figure 4-1. Satellite image of Southern Great Plains Facility (blue marker), surrounding cities (yellow markers), and other sources of anthropogenic pollution (red markers).

4.3.2 Instrumentation & data collection

Meteorological measurements and ACSM data were obtained from the Atmospheric Radiation Management data archives at the Southern Great Plains Lamont, OK location (Kulkarni, 2019; Kyrouac and Holdridge, 2019). This location was chosen as it is the closest possible location (within a few hundred meters) to where the mass spectrometers used here sampled ambient aerosol that had all desired meteorology data available throughout the sampling period.

Aerosol chemical composition was measured during the daytime for the majority of October 2019 using a high-resolution time-of-flight aerosol mass spectrometer (AMS, Aerodyne Research Inc.) and a laser ablation aerosol particle time-of-flight mass spectrometer (LAAPTOF, AeroMegt GmbH), described below. The AMS measured non-refractory, submicron aerosol using 600 °C thermal vaporization followed by 70 eV electron ionization with a time-of-flight mass analyzer in V-mode (DeCarlo et al., 2006; Liu et al., 2007). Data were averaged every 4 minutes and analyzed using Igor software packages SQUIRREL (version 1.62A) and PIKA (version 1.22A) with ionization efficiencies and sizing parameters based on calibrations using atomized, dried, and size-selected ammonium nitrate particles. Detection limits were calculated as 3 times the standard deviation of filtered air sampled throughout the campaign (DeCarlo et al., 2006) and were as follows: organic aerosol: 0.11 µg/m^3; ammonium: 0.012 µg/m^3; nitrate: 0.011 µg/m^3; sulfate: 0.0030 µg/m^3; chloride: 0.0029 µg/m^3. Composition dependent collection efficiencies were applied as discussed in Middlebrook et al. (2012). Elemental ratios were calculated using the improved ambient method, as this method is more accurate for the complex mixtures of organic aerosol present in ambient air (Canagaratna et al., 2015).

The LAAPTOF uses UV laser ablation for simultaneous desorption and ionization of all particle compositions followed by a bipolar time-of-flight mass analyzer. Particle sizes between 200 nm and 2.5 µm have good detection efficiencies and a higher-pressure aerodynamic lens inlet was used that more efficiently focuses larger supermicron particles. Unlike the AMS, the

LAAPTOF can detect refractory particle constituents such as mineral dusts. For some days of analysis, particle sizing was available by measuring the particle time-of-flight by light scattering between two 405 nm continuous-wave lasers; particle velocities were calibrated versus size using polystyrene latex spheres of known diameters. Both mass spectrometers sampled from separate lines about four meters above ground level to avoid locally generated aerosol from activity near the building. The LAAPTOF sampled from an aerosol concentrator that was placed outdoors on a platform above the building and an extra bypass flow was pulled close to the instrument inlet to reduce the residence time given the small LAAPTOF aerosol flow rate of 0.1 lpm. LAAPTOF data were converted to stick spectra using AeroMegt's Igor-based data analysis software version 0.1.7, then processed in Matlab (version 2019a) using built-in and custom functions. Clustering of single-particle mass spectra was conducted with Matlab's built-in Ward-based hierarchical clustering algorithm.

Back trajectories of air masses reaching the SGP site were calculated using the HYbrid Single-Particle Lagrangian Integrated Tracker (HYSPLIT) model developed by the National Oceanic and Atmospheric Administration (Stein et al., 2015). Meteorological data used in the model was 1° gridded from the Global Data Assimilation System (GDAS) and the back trajectories were calculated at an arrival height of 250 m and location of 36.6054 N, 97.4857 W. Data on active fire locations were obtained from the Fire Information for Resource Management System (FIRMS) operated by NASA's Earth Science Data and Information System (ESDIS). Fires are detected by the Moderate Resolution Imaging Spectroradiometer (MODIS) from the Terra and Aqua satellite platforms, and the data used here were from the Collection 6 standard product.

4.4 Results & discussion

4.4.1 Meteorological conditions

Throughout the campaign, the ambient temperature ranged from 1.4–27.2 °C with an average (± 1σ) of 13.4 ± 6.5 °C, the relative humidity ranged from 14.5–100% with an average (±

1σ) of 61 ± 23 %, the windspeed ranged from 0–15.4 m/s with an average (± 1σ) of 5.8 ± 2.9 m/s, and the wind direction was both from the north and south. These averages are fairly consistent with previous years. The only significant precipitation occurred on October 24–25 and a noticeable cold front passage occurred on October 15. Wind speed and direction are shown in Figure 4-2A and temperature and relative humidity are shown in Figure 4-2B.

4.4.2   Aerosol particle chemical characterization from AMS

Submicron nonrefractory aerosol chemical composition as measured by the AMS is shown as a fraction of the total aerosol mass measured in Figure 4-2C and as aerosol mass concentrations in Figure 4-2D. Organic aerosol (OA) was the dominant component, making up over half of the mass concentration on most days. On average, the aerosol consisted of 69% OA, 18% sulfate, 6% nitrate, 6% ammonium, and 0.6% chloride, which roughly matches the composition of aerosol measured in October 2011 by the SGP ACSM (Parworth et al., 2015). The total mass concentration (Fig. 4-2D right axis) varied from 0.35 – 6.0 μg/m^3 with an average (± 1σ) of 2.0 ± 1.3 μg/m^3. Nearly all measured concentrations were above detection limits. Table 4-1 displays bulk aerosol chemical composition ranges and averages.

Table 4-1. Aerosol composition as measured by the AMS. Compositional average mass concentrations, mass ranges, as well as fractional aerosol component averages and ranges for each aerosol constituent as well as the total mass. BDL indicates a measurement below the detection limit.

Aerosol Component	Average Mass ± 1σ (μg/m^3)	Mass Range (μg/m^3)	Average Fraction ± 1σ	Fraction Range
Organics	1.47 ± 1.09	0.17 – 4.50	0.69 ± 0.13	0.34 – 0.85
Sulfate	0.32 ± 0.17	0.06 – 1.08	0.18 ± 0.07	0.06 – 0.49
Nitrate	0.11 ± 0 .11	0.01 – 0.70	0.06 ± 0.06	0.01 – 0.39
Ammonium	0.10 ± 0.07	BDL – 0.36	0.06 ± 0.03	0.003 – 0.14
Chloride	0.008 ± 0.002	0.004 – 0.031	0.006 ± 0.004	0 – 0.02
Total	2.0 ± 1.3	0.35 – 6.0	-	-
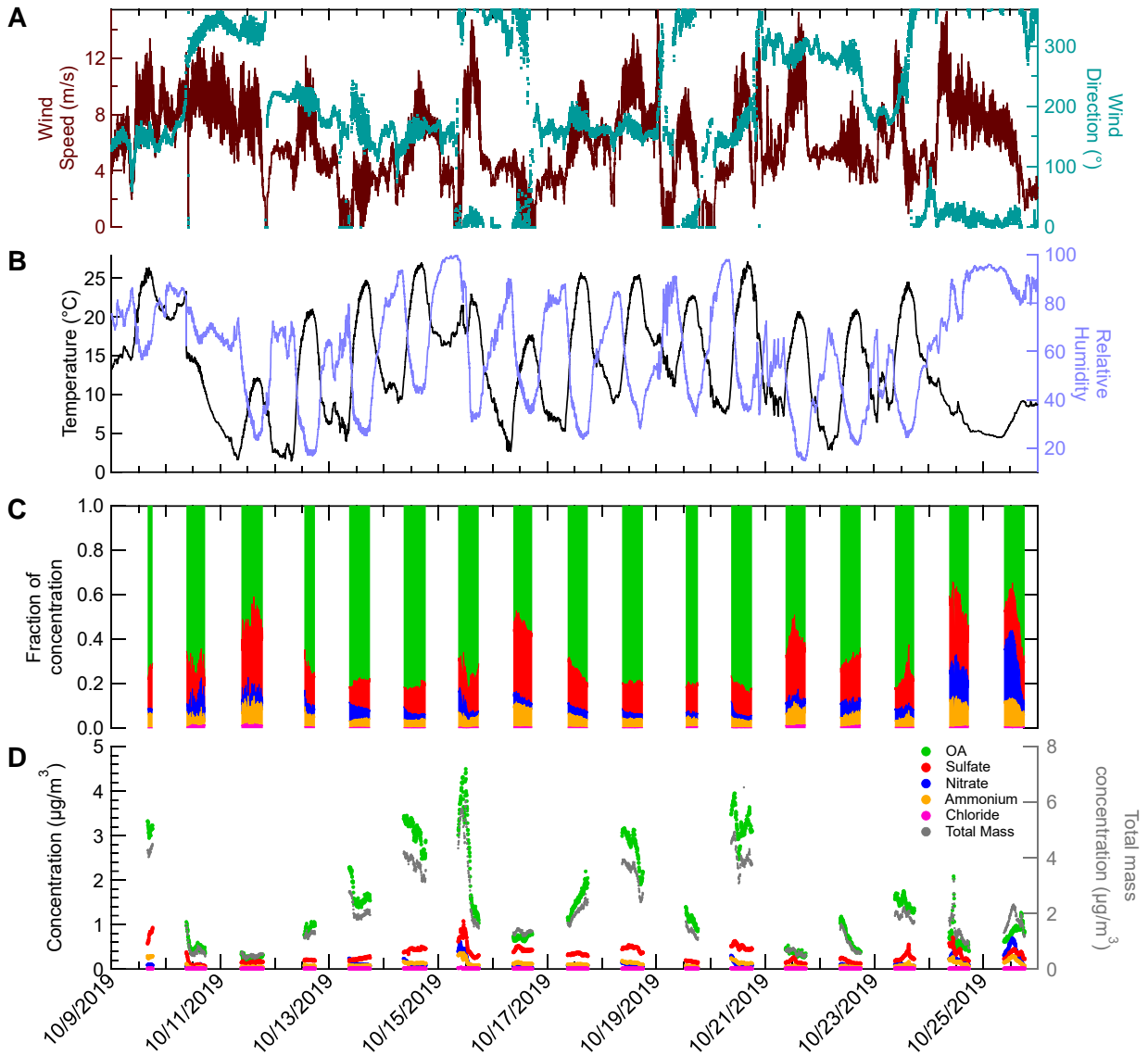
Figure 4-2. Meteorology data and aerosol chemical composition determined by the AMS. Panels **A** and **B** show meteorology data collected by ARM at the station collocated with mass spectrometry measurements. Panel **C** shows the fraction of the total mass concentration that is organic aerosol, sulfate, nitrate, ammonium, and chloride from the AMS. Panel **D** shows the absolute mass concentration of each of these aerosol components, along with the total mass concentration plotted on the right-axis. Gaps in AMS data are overnight when the instrument was not sampling.

4.4.2.1 Markers and evolution of oxidized organic aerosol

Figure 4-3 shows typical AMS triangle plots introduced by Cubison et al. (2011) and Ng et al. (2010). Fig. 4-3A shows f_{44}, the fraction of OA at m/z 44 (mostly CO_2^+ from thermal decomposition of carboxylic acids), vs. f_{43}, the fraction of OA at m/z 43 (mostly from non-acid oxygenates); higher values of f_{44} represent more oxidized organic aerosol while f_{43} represents less oxidized, fresher hydrocarbon-like organic aerosol (Ng et al., 2010). The two dashed lines form a triangular region which tends to encompass most ambient oxidized organic aerosol (OOA). Hydrocarbon-like OA (HOA), which is a good surrogate for primary OA, tends to have f_{44} values less than 0.05, and semi-volatile oxidized organic aerosol (SV-OOA) tends to fall in the bottom of the f_{44} vs. f_{43} triangle plot (Ng et al., 2011b). The f_{44} values observed in this campaign therefore indicate the organic aerosol was more oxidized and of lower volatility – low volatility OOA (LV-OOA) (Ng et al., 2011b). Data from this campaign fell within or above the triangle region, and on days when f_{44} vs f_{43} varied more, these values were more likely to lie outside the triangle region. On these days (e.g. Oct. 12 in blue, Oct. 16 in lime, Oct. 22 in yellow, Oct. 24 in red), notable changes in bulk chemical composition, wind speed, and/or wind direction occurred, which is likely why aerosol of different levels of oxidation were observed across the day. Compared to long-term measurements at this site, the f_{44} and f_{60} (a marker for biomass-burning aerosol, discussed below) values lie within the same ranges, while the f_{43} here extends to higher values (Parworth et al., 2015). The slopes of these triangle plots do not match the commonly observed slopes (outlined in the triangular regions in Fig. 4-3). This could be because the aerosol is a mixture of both oxidized OA (which would have a high f_{44} value) and fresh OA (which would have a high f_{43} value). Or, the higher values for each fraction may be an instrumental artifact due to the very clean environment and therefore very low instrument signal in rural Oklahoma; this warrants further analysis.

For some insight into whether or not the measured aerosol was influenced by organic aerosol from biomass burning, a plot of f44 vs. f60, the fraction of OA at m/z 60, can be examined (Fig. 4-3B). Levoglucosan is an anhydrous sugar formed from the combustion of cellulose and is known to fragment within the AMS to m/z 60 along with other similar sugars. Higher values of f60 greater than the dotted vertical line at f60 = 3 x 103 indicate that these samples may be influenced by organic aerosol from biomass burning (Cubison et al., 2011). However, f60 is not a flawless tracer for biomass-burning organic aerosol (BBOA) as other molecules can produce the same fragments, and f60 is known to decrease as BBOA ages (Cubison et al., 2011; Hennigan et al., 2010). Here, nearly all f60 data fall above the background air value. The data points are not within the triangle shown as this outlined region envelopes the aerosol observed within biomass-burning plumes as they age and biomass burning is not common in this area during October (Parworth et al., 2015). Days with high f60 include October 10, 22, 24, and 25 but these values may be less reliable may be due to inaccuracies from very low organic aerosol mass loadings on those days. Days with higher f60 and organic aerosol include October 12, 16, and 19. These data match observations about nearby fires; see section 4.4.4 for further discussion.
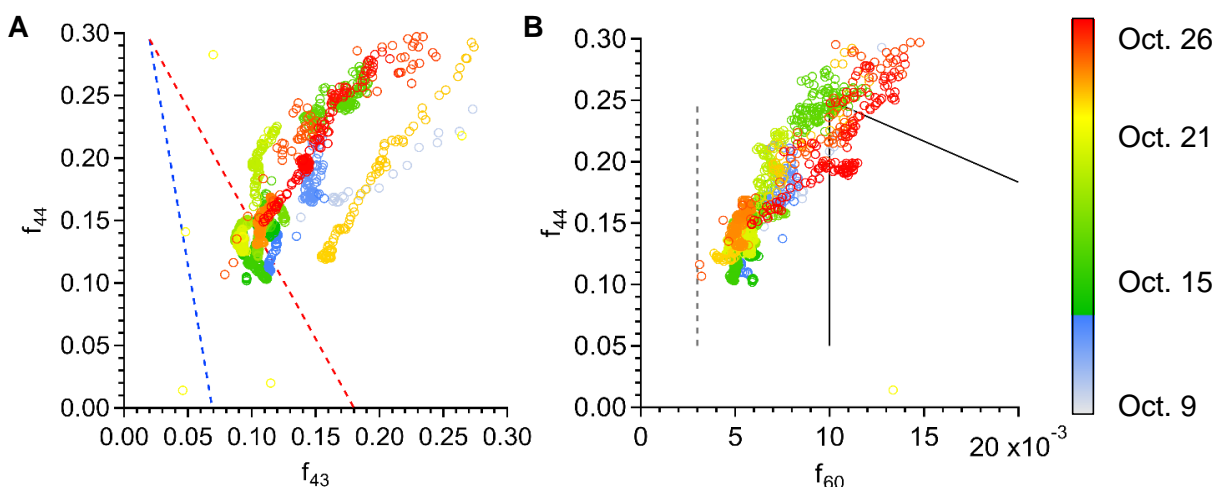
Figure 4-3. AMS plots of organic aerosol f_{44} vs f_{43} and f_{44} vs f_{60}. f_{44} is the fraction of organic aerosol at m/z 44, and likewise for f_{43} and f_{60}. Data is shown from entire campaign and is colored according to time. Noise was reduced by applying a moving average smoothing algorithm across a 28-minute time period.

Another way of representing organic aerosol composition is in a Van Krevelen diagram, which was originally created to describe changes in elemental composition throughout coal formation (van Krevelen, 1950). More recently, this representation has been used on data collected by high-resolution aerosol mass spectrometers, as the higher resolution allows for calculating elemental ratios (Hayes et al., 2013; Heald et al., 2010; Ng et al., 2011b). By plotting the atomic hydrogen-to-carbon ratio (H:C) vs. oxygen-to-carbon ratio (O:C), inferences can be made about changes to the chemical composition of the organic aerosol as it is transported throughout the atmosphere. The dashed gray lines in Figure 4-4 show these changes as the addition of different functional groups. For example, addition of a carboxylic acid group corresponds with a slope = –1, while a slope = –0.5 could be due to the addition of a carboxylic acid group after carbon backbone fragmentation, or other additions without fragmentation such as three alcohol groups and one carbonyl group (Ng et al., 2011b). The data shown here across the entire campaign have an average slope of –0.56, but the slope varies on different days ranging from –0.42 to –1.3, suggesting different aging mechanisms and degrees of oxidative aging are predominant on different days. Of course, different combinations of atmospheric aging through dilution, evaporation, fragmentation, oxidation, and secondary organic aerosol (SOA) formation occur for all aerosol populations, but it is interesting to see how the slope of the Van Krevelen diagram varies day to day and how it compares to other studies of ambient aerosol. The data shown here from Oklahoma are in accordance (both for the H:C and O:C values as well as the Van Krevelen diagram slopes) with other studies of ambient aerosol in California, rural China, and the Amazon that tend to have trendlines with slopes between –0.5 and –1, H:C between 1.2 and 2, and O:C between 0.2 to 0.8 (Hayes et al., 2013; Heald et al., 2010; Huang et al., 2011; Ng et al., 2011b). The H:C and O:C in our dataset suggest that the aerosol is fairly oxidized and can be classified as semi-volatile oxidized organic aerosol, which is more volatile than our f_{44} values suggested (Ng et al., 2011b).
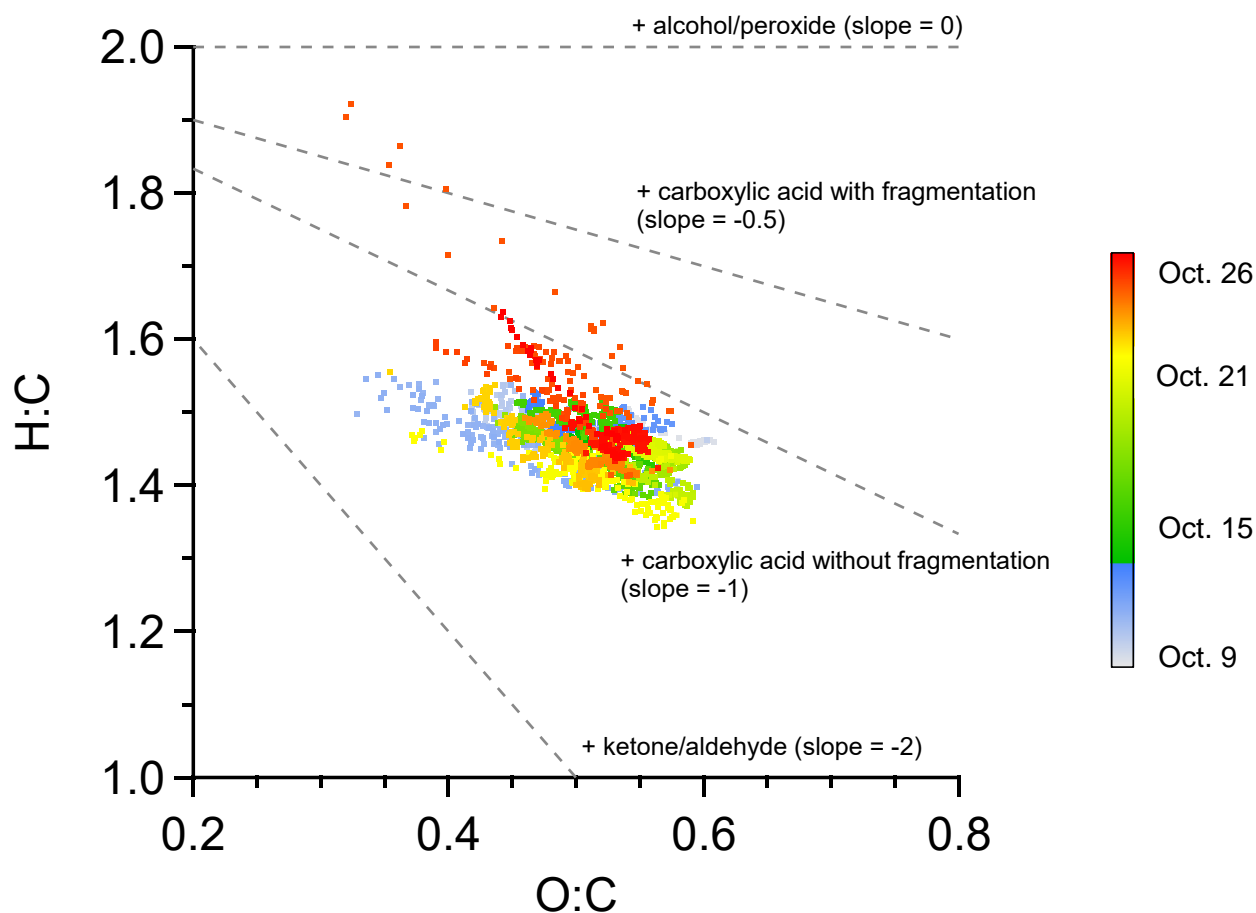
Figure 4-4. Representation of organic aerosol in a Van Krevelen diagram. High-resolution AMS data plotted as atomic H:C vs O:C. Data is shown from the entire campaign and is colored according to time. Noise was reduced by applying a moving average smoothing algorithm across a 28-minute time period.

4.4.2.2 Organonitrates estimated from AMS data

Part of the nitrate signal measured by the AMS may be organonitrates (ON), $RONO_2$, rather than inorganic nitrate (Farmer et al., 2010). Reactions of volatile organic compounds (VOCs) with the hydroxyl radical during the daytime or nitrate radical during the nighttime as well as the reactions between peroxy radicals and nitrogen oxides form ONs, which condense onto particles once they are low enough in volatility (Farmer et al., 2010; Lee Ng et al., 2017; Schervish and Donahue, 2020). As the addition of one nitrate functional group to an organic molecule can

decrease its volatility by about 2.5 orders of magnitude in saturated vapor pressure, quantifying ONs is important for understanding SOA production (Chuang and Donahue, 2016). ONs are difficult to quantify but can be directly measured by Fourier transform infrared spectroscopy (FTIR) with low sensitivity and low time resolution, and particulate ON upper bounds can be estimated using thermal dissociation-laser induced fluorescence (Farmer et al., 2010). Estimation of ONs is possible with the AMS, as the electron ionization fragments ONs into NO^+ and NO_2^+ which are distinguishable from other fragments in high-resolution versions of the AMS such as the one used in this campaign (Farmer et al., 2010). Many studies have shown that the ratio of these two fragments (NO_x^+ ratio = NO^+/NO_2^+) varies depending on whether the nitrate was present as inorganic nitrates (low ratios, < ~2.5) or organonitrates (higher ratios, ~3–15) (Farmer et al., 2010). Ammonium nitrate calibrations during this campaign resulted in an average NO_x^+ ratio of 1.8 while during ambient measurements the NO_x^+ ratio varied between 2–7, suggesting the presence of considerable ONs in the ambient aerosol.

Farmer et al. (2010) present a method based off of this ratio for estimating the fraction of nitrate reported by the AMS that may be due to ON rather than inorganic nitrate. Significant caveats apply, including that the NO_x^+ ratios from ON standards were not directly measured by the AMS used here and may not be representative of ambient ON, that low ON concentrations may cause inaccurate results, and that inorganic nitrates like $NaNO_3$ and $Ca(NO_3)_2$ may skew NO_x^+ ratios high (thus overestimating ON) (Farmer et al., 2010). After eliminating data points when nitrate concentrations were extremely low (< 0.05 µg/m^3), the fraction of nitrate signal that can be attributed to ON varied from 0.05 to 0.8. However, a more conservative fraction can be estimated by only considering times when nitrate concentrations were > 0.2 µg/m^3, resulting in the fraction of nitrate attributed to ON varying from 0.05 to 0.6 with total mass concentrations from 0.011 to 0.17 µg/m^3. Measuring organosulfates in the AMS is even more challenging, but very low concentrations (< 1 x 10^3 µg/m^3) of the $CH_3SO_2^+$ fragment suggest that these did not greatly

contribute to the sulfate signal measured during this campaign (Farmer et al., 2010; Huang et al., 2015).

4.4.2.3 Comparison between AMS and ACSM datasets

Mass concentrations from the HR-AMS here can be compared with those from the ACSM that continually operates at SGP. Differences were observed across the five aerosol components measured by the AMS, which may be attributable to 1) different sampling setups in slightly different locations on the SGP site; 2) differences in sample relative humidity, although no trend was observed between RH and whether our measurements were biased high or low compared to the ACSM; 3) inaccurate ionization efficiency calibrations in either instrument; 4) inaccurate relative ionization efficiency values in either instrument; 5) inaccurate or differing collection efficiencies in either instrument; 6) which ions were selected in the high-resolution analysis of our AMS data; 7) slight differences in the vaporizer temperature between the two instruments, among other documented problems (Pieber et al., 2016). The differences between ACSM data, HR-AMS data but at unit mass resolution, and fully high-resolution HR-AMS data varied throughout the campaign, suggesting that there was not a single error or measurement bias consistently causing the discrepancies (Figure 4-5). On most days, the HR-AMS OA was the highest, which has been observed in other comparison studies (Ng et al., 2011a). Sulfate and nitrate values were more likely to be consistent between the three measurement types. On some days (e.g. October 17), the AMS and ACSM OA data matched quite well, while on other days (e.g. October 21) the HR-AMS and ACSM OA data were more consistent with one another. While these differences can be significant at times (up to ~40% difference in OA and ~100% in inorganic species), the overall daily trends in each species closely track each other among all measurement types. Still, the discrepancies suggest that while the ACSM is more robust and easy to operate in remote locations for longer periods of time, it may not reproduce HR-AMS data. Intercomparison studies between the ACSM and AMS have demonstrated that the two instruments can produce more

similar data, suggesting that some of the inconsistencies here may be because the instruments were not simultaneously calibrated and operated by the same users or because of problems specific to the SGP site (Crenn et al., 2015). When possible, each measurement site should undergo thorough comparisons between similar instruments for at least an understanding of the discrepancies and magnitudes of error and at best for a robust way to correct data to the most accurate values possible.
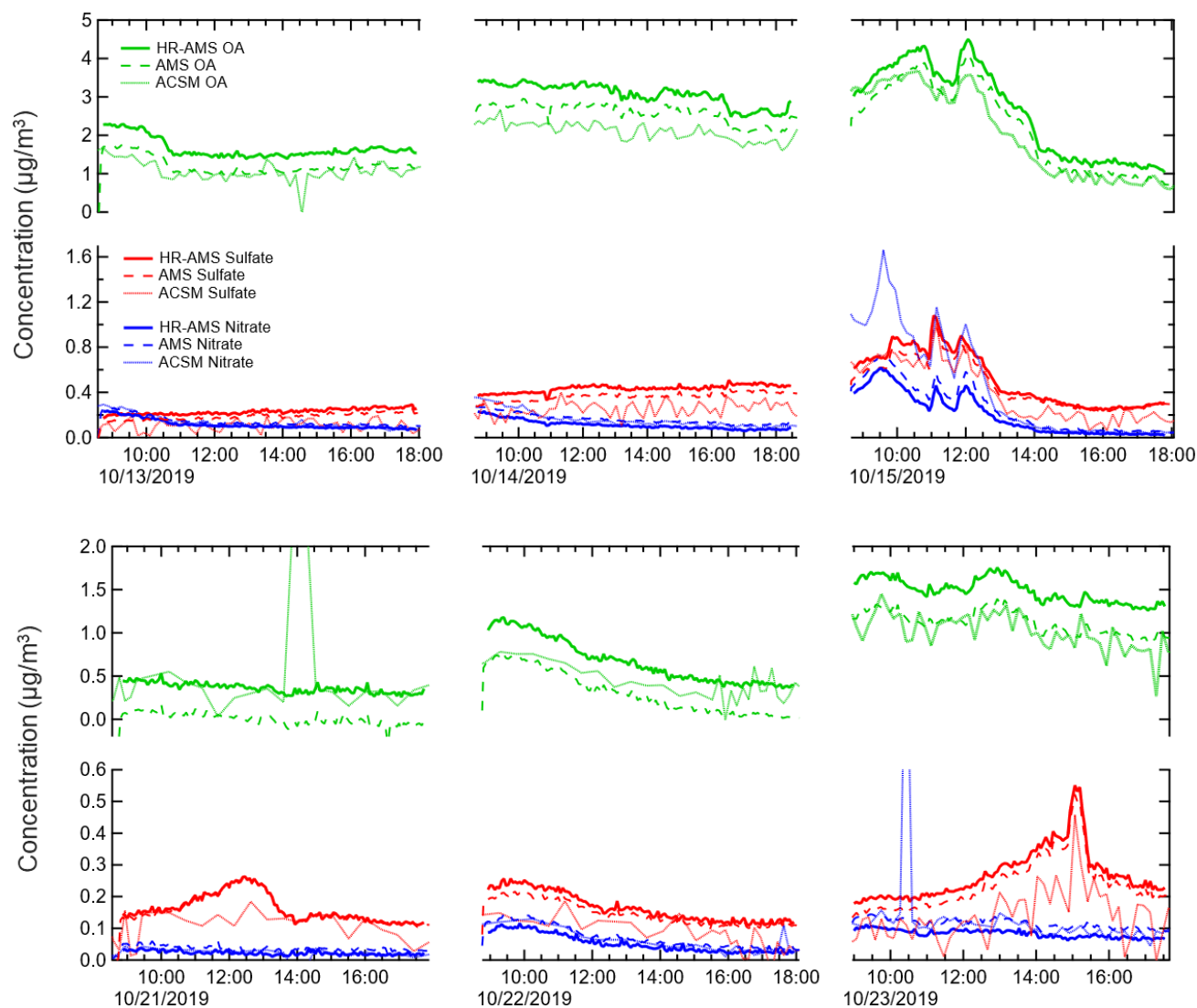
Figure 4-5. Mass concentrations for organic aerosol, sulfate, and nitrate from HR-AMS (solid lines), HR-AMS without high-resolution analysis (dashed lines), and SGP's ACSM (dotted lines).

4.4.3 Single-particle chemical characterization using the LAAPTOF

Individual particles detected by the LAAPTOF were assigned to five clusters, or categories, based on similarities in their mass spectra using a hierarchical classification algorithm based on Ward's method (Rebotier and Prather, 2007). The only cluster that was composed of a single overall class was the inorganic particle class (mostly nitrate, sulfate, and ammonium), which was only present in high proportions for three days (Figure 4-6). Other clusters all contained particle members that were each mixtures of multiple components: inorganic-organic (mainly inorganic with smaller amounts of organic), organic-inorganic (mainly organic with smaller amounts of inorganic), mineral-organic, or mineral-organic-inorganic. On most days, the particles measured were mostly from the mineral-organic-inorganic and mineral-organic clusters, as shown in Fig. 4-6. The organic-inorganic cluster was only present at number fractions above 0.05 on October 17, 18, and 23, all of which had organic aerosol mass fractions in submicron aerosol above 0.7, as measured by the AMS. In general, the mixing state of particles as determined by the LAAPTOF – that most particles were mixtures of multiple components – is in accordance with the well-mixed speciated particle size distributions from the AMS, discussed in section 4.4.4.

Figure 4-6. The fraction of total particle numbers detected in the LAAPTOF assigned to each of the five main clusters using a hierarchical clustering algorithm.

116

4.4.4 Aerosol sources and size distributions

The DOE SGP site is located in inland United States, in the middle of farmland, far from any major cities. We therefore did not to expect to measure any large sources of primary organic aerosol. Indeed, the AMS revealed oxidized organic aerosol and particle size distributions obtained from particle time-of-flight (pToF) mode of each species were similar, indicating that the aerosol was well-mixed (Figure 4-7). Weekly back trajectory frequency plots were created for the month of October from the NOAA HYSPLIT model to determine where the air masses (and thus the aerosol particles) that reached SGP originated from; these are shown in Figure A4-1. Most air masses originated within Oklahoma, with some transport from Texas (south) and Kansas (north) and long-range transport originated from the northwest. In this section, we look beyond back trajectories to examine periods of interest as identified by the mass spectrometer datasets.
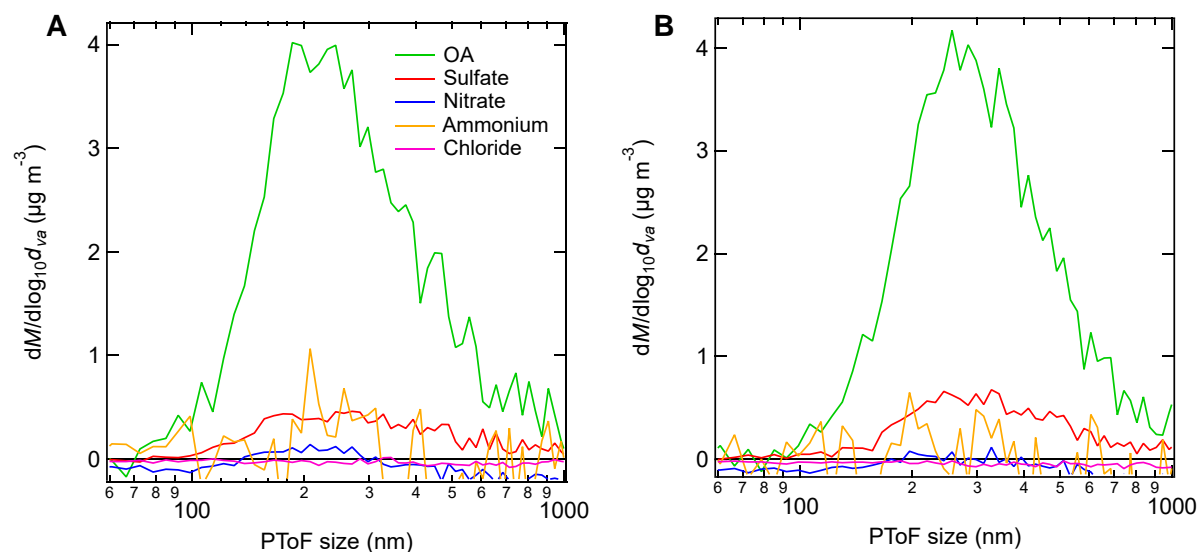
Figure 4-7. Average size distribution of AMS PM$_1$ for October 14 **(A)** and October 20 **(B)**. Concentrations of most species are too low for reliable distributions and these two days had some of the highest total mass concentrations.

The signal fraction at m/z 60 from the AMS was used to identify possible periods of biomass-burning aerosol. While most biomass burning in this region occurs during the spring months, there are still some local fires throughout the year (Parworth et al., 2015). Fires can be

identified by satellites based on the emission of mid-infrared radiation from fires, and these data are readily available from NASA's Fire Information for Resource Management System (FIRMS). One day with high biomass-burning markers observed in the AMS data was October 16. Indeed, many more fires were identified by satellite on October 16 within a 350 km x 350 km area centered at the SGP site compared to any other day in the campaign (depicted in Figure A4-2). LAAPTOF particle clustering also revealed that the vast majority of particles on October 16 were mineral-organic-inorganic and mineral-organic mixtures (Figure 4-8). Biomass-burning aerosol is known to be composed of complex mixtures of minerals, inorganics, organic aerosol, and soot (Jahn et al., 2020; Li et al., 2003; Vassilev et al., 2012).
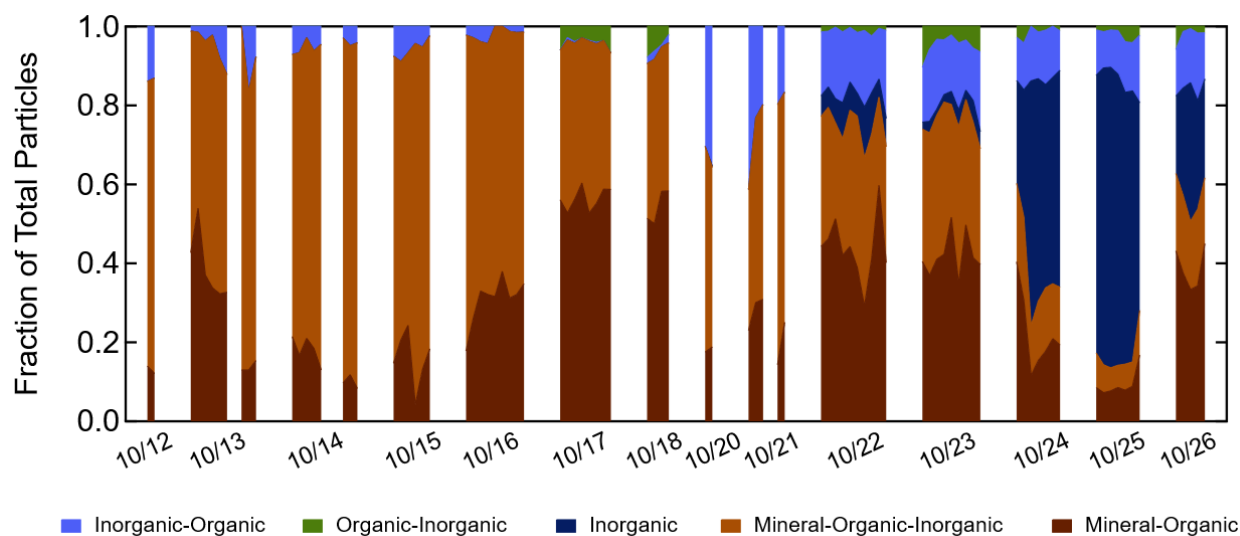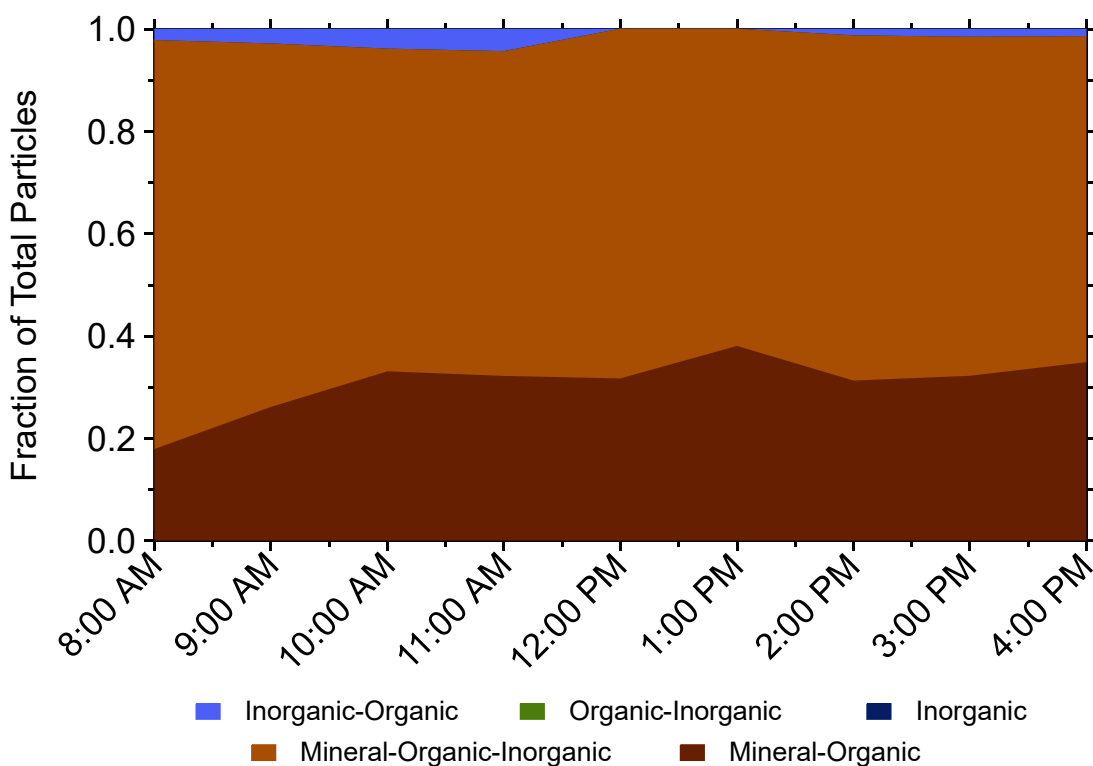

Figure 4-8. The fraction of total particle numbers detected in the LAAPTOF assigned to each of the five clusters on October 16.

4.5   Conclusion

In this work, we analyzed the chemical composition of ambient aerosol at the Southern Great Plains ARM continental background site using two mass spectrometers. High-resolution aerosol mass spectrometry revealed that the majority of submicron particulate matter was oxidized organic aerosol with speciated size distributions demonstrating that the organic aerosol was well-mixed with inorganic components. Some evidence of biomass-burning aerosol was observed and matched regional fire identification data as well as the single-particle clustering from the LAAPTOF. Up to 0.2 $\mu g/m^3$ of organonitrates were measured which suggests that not all of the nitrate signal from the aerosol chemical speciation monitor (that measures aerosol composition continually at SGP) is truly inorganic. Further comparison revealed that there are differences between high-resolution AMS and ACSM data that vary day-to-day and therefore are dependent on a multitude of factors which should be further investigated. Single-particle data from the LAAPTOF also revealed that particles tended to be mixtures of multiple components, besides a few days when particles were primarily inorganic. The abundance of mixed particles and oxidized organic aerosol suggests that most aerosol came from long-range transport, with perhaps some local emissions classified as a single-component inorganic cluster in the LAAPTOF.

Ground-based high-resolution and single-particle mass spectrometry data are not often available from the SGP site. Therefore, these data can be combined with the meteorological, radiative, and optical aerosol properties regularly measured at SGP to improve our understanding and modeling of aerosol properties in a United States continental background site. Specifically, the compositional data provided here will be incorporated into current ice nucleation parameterizations to hopefully improve the closure between measured and modeled ice nucleating particle concentrations. Understanding the direct and indirect radiative effects of clouds

remains a research topic with large uncertainty, and developing better parameterizations of ice nucleation and cloud glaciation will help to reduce this critical uncertainty.

4.6   Acknowledgments

4.7   References

Apte, J. S., Brauer, M., Cohen, A. J., Ezzati, M. and Pope, C. A.: Ambient PM2.5 Reduces Global and Regional Life Expectancy, Environ. Sci. Technol. Lett., 5(9), 546–551, doi:10.1021/acs.estlett.8b00360, 2018.

Broekhuizen, K., Chang, R. Y. W., Leaitch, W. R., Li, S. M. and Abbatt, J. P. D.: Closure between measured and modeled cloud condensation nuclei (CCN) using size-resolved aerosol compositions in downtown Toronto, Atmos. Chem. Phys., 6(9), 2513–2524, doi:10.5194/acp-6-2513-2006, 2006.

Canagaratna, M. R., Jimenez, J. L., Kroll, J. H., Chen, Q., Kessler, S. H., Massoli, P., Hildebrandt Ruiz, L., Fortner, E., Williams, L. R., Wilson, K. R., Surratt, J. D., Donahue, N. M., Jayne, J. T. and Worsnop, D. R.: Elemental ratio measurements of organic compounds using aerosol mass spectrometry: Characterization, improved calibration, and implications, Atmos. Chem. Phys., 15(1), 253–272, doi:10.5194/acp-15-253-2015, 2015.

Chuang, W. K. and Donahue, N. M.: A two-dimensional volatility basis set-Part 3: Prognostic modeling and NOx dependence, Atmos. Chem. Phys., 16(1), 123–134, doi:10.5194/acp-16-123-2016, 2016.

Crenn, V., Sciare, J., Croteau, P. L., Verlhac, S., Fröhlich, R., Belis, C. A., Aas, W., Äijälä, M., Alastuey, A., Artiñano, B., Baisnée, D., Bonnaire, N., Bressi, M., Canagaratna, M., Canonaco, F., Carbone, C., Cavalli, F., Coz, E., Cubison, M. J., Esser-Gietl, J. K., Green, D. C., Gros, V., Heikkinen, L., Herrmann, H., Lunder, C., Minguillón, M. C., Močnik, G., O'dowd, C. D., Ovadnevaite, J., Petit, J.-E., Petralia, E., Poulain, L., Priestman, M., Riffault, V., Ripoll, A., Sarda-Estève, R., Slowik, J. G., Setyan, A., Wiedensohler, A., Baltensperger, U., Prévôt, A. S. H., Jayne, J. T. and Favez, O.: ACTRIS ACSM intercomparison-Part 1: Reproducibility of concentration and fragment results from 13 individual Quadrupole Aerosol Chemical Speciation Monitors (Q-ACSM) and consistency with co-located instruments, Atmos. Meas. Tech, 8, 5063–5087,

doi:10.5194/amt-8-5063-2015, 2015.

Cubison, M. J., Ortega, A. M., Hayes, P. L., Farmer, D. K., Day, D. A., Lechner, M. J., Brune, W. H., Apel, E., Diskin, G., Fisher, J. A., Fuelberg, H. E., Hecobian, A., Knapp, D. J., Mikoviny, T., Riemer, D., Sachse, G. W., Sessions, W., Weber, R. J., Weinheimer, A. J., Wisthaler, A. and Jimenez, J. L.: Effects of aging on organic aerosol from open biomass burning smoke in aircraft and laboratory studies, Atmos. Chem. Phys. Atmos. Chem. Phys., 11, 12049–12064, doi:10.5194/acp-11-12049-2011, 2011.

DeCarlo, P. F., Kimmel, J. R., Trimborn, A., Northway, M. J., Jayne, J. T., Aiken, A. C., Gonin, M., Fuhrer, K., Horvath, T., Docherty, K. S., Worsnop, D. R. and Jimenez, J. L.: Field-deployable, high-resolution, time-of-flight aerosol mass spectrometer, Anal. Chem., 78(24), 8281–8289, doi:10.1021/ac061249n, 2006.

DeMott, P. J., Prenni, A. J., Liu, X., Kreidenweis, S. M., Petters, M. D., Twohy, C. H., Richardson, M. S., Eidhammer, T. and Rogers, D. C.: Predicting global atmospheric ice nuclei distributions and their impacts on climate, Proc. Natl. Acad. Sci., 107(25), 11217–11222, doi:10.1073/pnas.0910818107, 2010.

Farmer, D. K., Matsunaga, a, Docherty, K. S., Surratt, J. D., Seinfeld, J. H., Ziemann, P. J. and Jimenez, J. L.: Response of an aerosol mass spectrometer to organonitrates and organosulfates and implications for atmospheric chemistry., Proc. Natl. Acad. Sci. U. S. A., 107, 6670–6675, doi:10.1073/pnas.0912340107, 2010.

Fast, J. D., Berg, L. K., Alexander, L., Bell, D., D'Ambro, E., Hubbe, J., Kuang, C., Liu, J., Long, C., Matthews, A., Mei, F., Newsom, R., Pekour, M., Pinterich, T., Schmid, B., Schobesberger, S., Shilling, J., Smith, J. N., Springston, S., Suski, K., Thornton, J. A., Tomlinson, J., Wang, J., Xiao, H. and Zelenyuk, A.: Overview of the HI-SCALE Field Campaign: A New Perspective on Shallow Convective Clouds, Bull. Am. Meteorol. Soc., 100(5), 821–840, doi:10.1175/BAMS-D-18-0030.1, 2019.

Fuzzi, S., Baltensperger, U., Carslaw, K., Decesari, S., Denier Van Der Gon, H., Facchini, M. C., Fowler, D., Koren, I., Langford, B., Lohmann, U., Nemitz, E., Pandis, S. N., Riipinen, I., Rudich, Y., Schaap, M., Slowik, J. G., Spracklen, D. V., Vignati, E., Wild, M., Williams, M. and Gilardoni, S.: Particulate matter, air quality and climate: Lessons learned and future needs, Atmos. Chem. Phys., doi:10.5194/acp-15-8217-2015, 2015.

Hayes, P. L., Ortega, A. M., Cubison, M. J., Froyd, K. D., Zhao, Y., Cliff, S. S., Hu, W. W., Toohey, D. W., Flynn, J. H., Lefer, B. L., Grossberg, N., Alvarez, S., Rappenglück, B., Taylor, J. W., Allan, J. D., Holloway, J. S., Gilman, J. B., Kuster, W. C., De Gouw, J. A., Massoli, P., Zhang, X., Liu, J., Weber, R. J., Corrigan, A. L., Russell, L. M., Isaacman, G., Worton, D. R., Kreisberg, N. M., Goldstein, A. H., Thalman, R., Waxman, E. M., Volkamer, R., Lin, Y. H., Surratt, J. D., Kleindienst, T. E., Offenberg, J. H., Dusanter, S., Griffith, S., Stevens, P. S., Brioude, J., Angevine, W. M. and Jimenez, J. L.: Organic aerosol composition and sources in Pasadena, California, during the 2010 CalNex campaign, J. Geophys. Res. Atmos., 118(16), 9233–9257, doi:10.1002/jgrd.50530, 2013.

Heald, C. L., Kroll, J. H., Jimenez, J. L., Docherty, K. S., Decarlo, P. F., Aiken, A. C., Chen, Q., Martin, S. T., Farmer, D. K. and Artaxo, P.: A simplified description of the evolution of organic aerosol composition in the atmosphere, Geophys. Res. Lett., 37(8), doi:10.1029/2010GL042737, 2010.

Hennigan, C. J., Sullivan, A. P., Collett, J. L. and Robinson, A. L.: Levoglucosan stability in biomass burning particles exposed to hydroxyl radicals, Geophys. Res. Lett., 37(9), n/a-n/a, doi:10.1029/2010GL043088, 2010.

Hodshire, A. L., Lawler, M. J., Zhao, J., Ortega, J., Jen, C., Yli-Juuti, T., Brewer, J. F., Kodros, J. K., Barsanti, K. C., Hanson, D. R., Mcmurry, P. H., Smith, J. N. and Pierce, J. R.: Multiple new-particle growth pathways observed at the US DOE Southern Great Plains field site, Atmos. Chem. Phys, 16, 9321–9348, doi:10.5194/acp-16-9321-2016, 2016.

Hoose, C., Kristjánsson, J. E., Chen, J. P. and Hazra, A.: A classical-theory-based parameterization of heterogeneous ice nucleation by mineral dust, soot, and biological particles in a global climate model, J. Atmos. Sci., 67(8), 2483–2503, doi:10.1175/2010JAS3425.1, 2010.

Huang, D. D., Li, Y. J., Lee, B. P. and Chan, C. K.: Analysis of organic sulfur compounds in atmospheric aerosols at the HKUST supersite in Hong Kong using HR-ToF-AMS, Environ. Sci. Technol., 49(6), 3672–3679, doi:10.1021/es5056269, 2015.

Huang, X.-F., He, L.-Y., Hu, M., Canagaratna, M. R., Kroll, J. H., Ng, N. L., Zhang, Y.-H., Lin, Y., Xue, L., Sun, T.-L., Liu, X.-G., Shao, M., Jayne, J. T. and Worsnop, D. R.: Characterization of submicron aerosols at a rural site in Pearl River Delta of China using an Aerodyne High-Resolution Aerosol Mass Spectrometer, Atmos. Chem. Phys, 11, 1865–1877, doi:10.5194/acp-11-1865-2011, 2011.

IPCC: Climate Change 2014: Synthesis Report. Contribution of Working Groups I, II and III to the Fifth Assessment Report of the Intergovernmental Panel on Climate Change, Geneva, Switzerland., 2014.

Jahn, L. G., Polen, M. J., Jahl, L. G., Brubaker, T. A., Somers, J. and Sullivan, R. C.: Biomass combustion produces ice-active minerals in biomass-burning aerosol and bottom ash, Proc. Natl. Acad. Sci., 201922128, doi:10.1073/pnas.1922128117, 2020.

van Krevelen, D. W.: Graphical-statistical method for the study of structure and reaction processes of coal, Fuel, 29, 269–284, 1950.

Kulkarni, G.: Atmospheric Radiation Measurement (ARM) user facility, Southern Great Plains (SGP) Lamont, OK., 2019.

Kyrouac, J. and Holdridge, D.: Atmospheric Radiation Measurement (ARM) user facility, 2019-10-01 to 2019-10-31, Southern Great Plains (SGP) Lamont, OK (Extended), 2019.

Lance, S., Nenes, A., Mazzoleni, C., Dubey, M. K., Gates, H., Varutbangkul, V., Rissman, T. A., Murphy, S. M., Sorooshian, A., Flagan, R. C., Seinfeld, J. H., Feingold, G. and Jonsson, H. H.: Cloud condensation nuclei activity, closure, and droplet growth kinetics of Houston aerosol during the Gulf of Mexico Atmospheric Composition and Climate Study (GoMACCS), J. Geophys. Res., 114(D7), doi:10.1029/2008jd011699, 2009.

Lee Ng, N., Brown, S. S., Archibald, A. T., Atlas, E., Cohen, R. C., Crowley, J. N., Day, D. A., Donahue, N. M., Fry, J. L., Fuchs, H., Griffin, R. J., Guzman, M. I., Herrmann, H., Hodzic, A., Iinuma, Y., Kiendler-Scharr, A., Lee, B. H., Luecken, D. J., Mao, J., McLaren, R., Mutzel, A., Osthoff, H. D., Ouyang, B., Picquet-Varrault, B., Platt, U., Pye, H. O. T., Rudich, Y., Schwantes, R. H., Shiraiwa, M., Stutz, J., Thornton, J. A., Tilgner, A., Williams, B. J. and Zaveri, R. A.: Nitrate radicals and biogenic volatile organic compounds: Oxidation, mechanisms, and organic aerosol, in Atmospheric Chemistry and Physics, vol. 17, pp. 2103–2162., 2017.

Li, J., Pósfai, M., Hobbs, P. V. and Buseck, P. R.: Individual aerosol particles from biomass burning in southern Africa: 2, Compositions and aging of inorganic particles, J. Geophys. Res. Atmos., 108(D13), n/a-n/a, doi:10.1029/2002JD002310, 2003.

Liu, P. S. K., Deng, R., Smith, K. a., Williams, L. R., Jayne, J. T., Canagaratna, M. R., Moore, K.,

Onasch, T. B., Worsnop, D. R. and Deshler, T.: Transmission Efficiency of an Aerodynamic Focusing Lens System: Comparison of Model Calculations and Laboratory Measurements for the Aerodyne Aerosol Mass Spectrometer, Aerosol Sci. Technol., 41(8), 721–733, doi:10.1080/02786820701422278, 2007.

Marinescu, P. J., Levin, E. J. T., Collins, D., Kreidenweis, S. M. and Van Den Heever, S. C.: Quantifying aerosol size distributions and their temporal variability in the Southern Great Plains, USA, Atmos. Chem. Phys, 19, 11985–12006, doi:10.5194/acp-19-11985-2019, 2019.

Martin, M., Chang, Y.-W., Sierau, B., Sjogren, S., Swietlicki, E., Abbatt, J. P. D., Leck, C. and Lohmann, U.: Atmospheric Chemistry and Physics Cloud condensation nuclei closure study on summer arctic aerosol, Atmos. Chem. Phys, 11, 11335–11350, doi:10.5194/acp-11-11335-2011, 2011.

Middlebrook, A. M., Bahreini, R., Jimenez, J. L. and Canagaratna, M. R.: Evaluation of Composition-Dependent Collection Efficiencies for the Aerodyne Aerosol Mass Spectrometer using Field Data, Aerosol Sci. Technol., 46(3), 258–271, doi:10.1080/02786826.2011.620041, 2012.

Ng, N. L., Canagaratna, M. R., Zhang, Q., Jimenez, J. L., Tian, J., Ulbrich, I. M., Kroll, J., Docherty, K. S., Chhabra, P. S., Bahreini, R., Murphy, S. M., Seinfeld, J. H., Hildebrandt, L., Donahue, N. M., DeCarlo, P. F., Lanz, V. A., Prévôt, A. S. H., Dinar, E., Rudich, Y. and Worsnop, D. R.: Organic aerosol components observed in Northern Hemispheric datasets from Aerosol Mass Spectrometry, Atmos. Chem. Phys. Atmos. Chem. Phys., 10, 4625–4641, doi:10.5194/acp-10-4625-2010, 2010.

Ng, N. L., Herndon, S. C., Trimborn, A., Canagaratna, M. R., Croteau, P. L., Onasch, T. B., Sueper, D., Worsnop, D. R., Zhang, Q., Sun, Y. L. and Jayne, J. T.: An Aerosol Chemical Speciation Monitor (ACSM) for Routine Monitoring of the Composition and Mass Concentrations of Ambient Aerosol, Aerosol Sci. Technol., 45(7), 780–794, doi:10.1080/02786826.2011.560211, 2011a.

Ng, N. L., Canagaratna, M. R., Jimenez, J. L., Chhabra, P. S., Seinfeld, J. H. and Worsnop, D. R.: Changes in organic aerosol composition with aging inferred from aerosol mass spectra, Atmos. Chem. Phys., 11(13), 6465–6474, doi:10.5194/acp-11-6465-2011, 2011b.

Parworth, C., Fast, J., Mei, F., Shippert, T., Sivaraman, C., Tilp, A., Watson, T. and Zhang, Q.: Long-term measurements of submicrometer aerosol chemistry at the Southern Great Plains (SGP) using an Aerosol Chemical Speciation Monitor (ACSM), Atmos. Environ., 106, 43–55, doi:10.1016/j.atmosenv.2015.01.060, 2015.

Pieber, S. M., El Haddad, I., Slowik, J. G., Canagaratna, M. R., Jayne, J. T., Platt, S. M., Bozzetti, C., Daellenbach, K. R., Fröhlich, R., Vlachou, A., Klein, F., Dommen, J., Miljevic, B., Jiménez, J. L., Worsnop, D. R., Baltensperger, U. and Prévôt, A. S. H.: Inorganic Salt Interference on CO2+ in Aerodyne AMS and ACSM Organic Aerosol Composition Studies, Environ. Sci. Technol., 50(19), 10494–10503, doi:10.1021/acs.est.6b01035, 2016.

Pope, C. A., Ezzati, M. and Dockery, D. W.: Fine-particulate air pollution and life expectancy in the United States., N. Engl. J. Med., 360(4), 376–386, doi:10.1056/NEJMsa0805646, 2009.

Rebotier, T. P. and Prather, K. A.: Aerosol time-of-flight mass spectrometry data analysis: A benchmark of clustering algorithms, Anal. Chim. Acta, 585(1), 38–54, doi:10.1016/j.aca.2006.12.009, 2007.

Schervish, M. and Donahue, N. M.: Peroxy radical chemistry and the volatility basis set, Atmos.

Chem. Phys, 20, 1183–1199, doi:10.5194/acp-20-1183-2020, 2020.

Seinfeld, J. H., Bretherton, C., Carslaw, K. S., Coe, H., DeMott, P. J., Dunlea, E. J., Feingold, G., Ghan, S., Guenther, A. B., Kahn, R., Kraucunas, I., Kreidenweis, S. M., Molina, M. J., Nenes, A., Penner, J. E., Prather, K. A., Ramanathan, V., Ramaswamy, V., Rasch, P. J., Ravishankara, A. R., Rosenfeld, D., Stephens, G. and Wood, R.: Improving our fundamental understanding of the role of aerosol-cloud interactions in the climate system, Proc. Natl. Acad. Sci. U. S. A., 113(21), 5781–5790, doi:10.1073/pnas.1514043113, 2016.

Stein, A. F., Draxler, R. R., Rolph, G. D., Stunder, B. J. B., Cohen, M. D. and Ngan, F.: Noaa's hysplit atmospheric transport and dispersion modeling system, Bull. Am. Meteorol. Soc., 96(12), 2059–2077, doi:10.1175/BAMS-D-14-00110.1, 2015.

Stokes, G. M. and Schwartz, S. E.: The Atmospheric Radiation Measurement (ARM) Program: Programmatic Background and Design of the Cloud and Radiation Test Bed, Bull. Am. Meteorol. Soc., 75(7), 1201–1221, 1994.

Vassilev, S. V., Baxter, D., Andersen, L. K., Vassileva, C. G. and Morgan, T. J.: An overview of the organic and inorganic phase composition of biomass, Fuel, 94, 1–33, doi:10.1016/j.fuel.2011.09.030, 2012.

Zhang, J., Zheng, Y., Li, Z., Xia, X. and Chen, H.: A 17-year climatology of temperature inversions above clouds over the ARM SGP site: The roles of cloud radiative effects, Atmos. Res., 237, doi:10.1016/j.atmosres.2019.104810, 2020.

4.8 Appendix
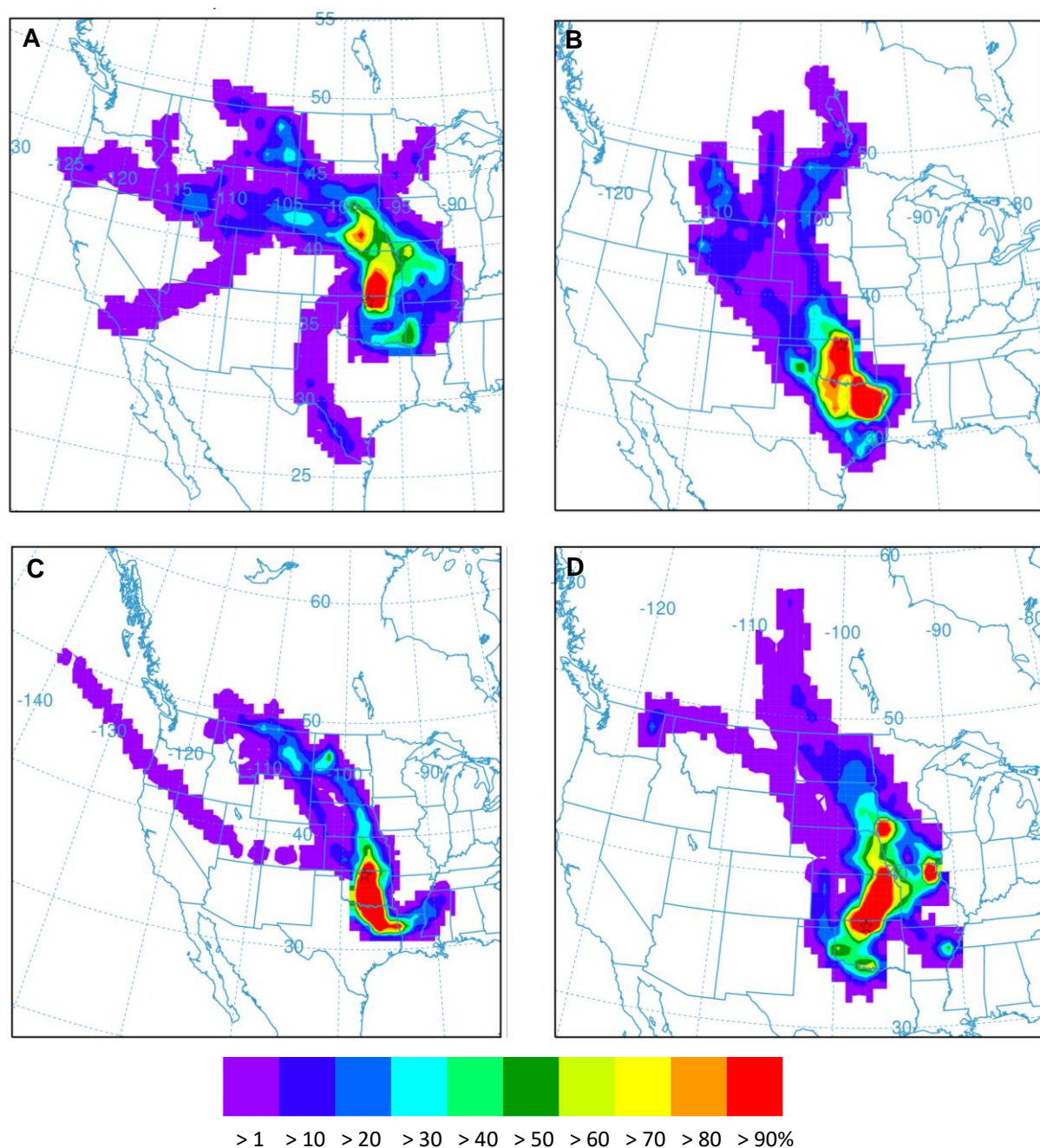
Figure A4-1. Weekly HYSPLIT back-trajectory frequency plots for October. 48 hour back-trajectories were calculated on a weekly basis (**A-D** for the first through fourth weeks of October) with SGP site as the point of origin (starred on each map). Color bar shows the percentage of time that an air parcel arriving at the point of origin originated at a location on the map, represented as the number of endpoints per grid square divided by the number of trajectories during that time period. Local transport was observed across all four weeks, with long-range transport usually arriving from the northwest.
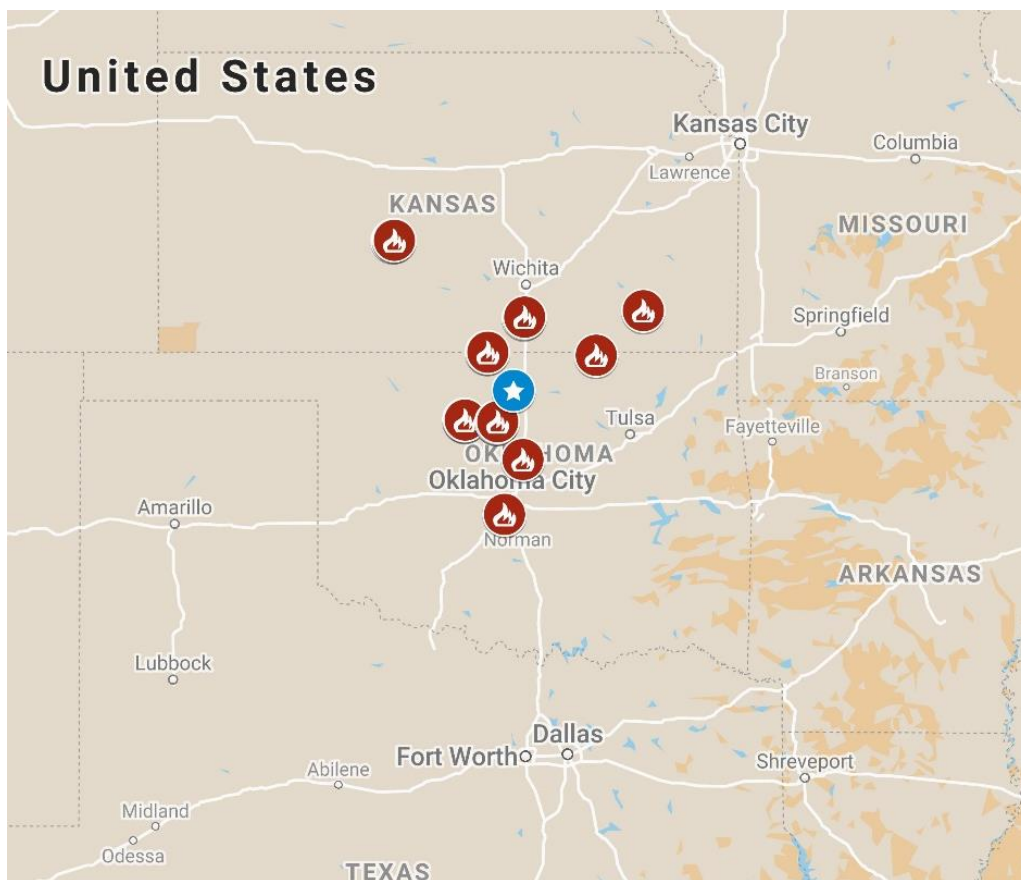
Figure A4-2. Fire locations on October 16. Red fire symbols depict locations of all fires identified by the ESDIS Fire Information for Resource Management System within a 350 km x 350 km area, centered at the SGP site (blue star symbol).

5 Conclusion

5.1 Summary

In chapter 2, I presented a new understanding regarding how the atmospheric aging of authentic biomass-burning aerosol (BBA) in a smog chamber influences the ice-nucleating ability of several types of BBA. We found that the dilution and evaporation that the BBA undergoes over several hours leads to the exposure of existing mineral-based ice-active sites. Additional aging by the hydroxyl radical also oxidizes the organic carbon aerosol components, causing them to become more water soluble. This promotes the dissolution of primary aerosol components covering ice-active sites within water droplets, and this can lead to an increase in the ice-nucleation activity of the BBA. Conversely, the formation of secondary organic aerosol, can conceal existing ice-active sites and potentially decrease the ice-nucleation activity of some BBA. Overall, our results demonstrated that under realistic scenarios where biomass-burning plumes spread over vast areas of the atmosphere and are diluted and aged, there will be an increase in the concentration of ice nucleating particles of greater than an order of magnitude even at warm mixed-phase cloud temperatures above –25 °C, and an increase in the onset freezing temperature of up to 8 °C. We estimate that this would lead to ice nucleating particle concentrations above background levels across an area of 10^5 square kilometers by 5 km in biomass-burning plume height from just a single square meter of burned grassland.

In chapter 3, I presented results from heterogeneous kinetics experiments using a entrained aerosol flow tube reactor system to determine the reactive uptake coefficient (reaction probability) of dinitrogen pentoxide, $\gamma(N_2O_5)$, and yield of nitryl chloride, $\varphi(ClNO_2)$ for authentic biomass-burning aerosol. Determining these values is important as these gaseous reactants affect ozone concentrations, the lifetime of nitrogen oxides, and the cycling of atmospheric oxidants. Our initial collaborative experiments with the University of Washington showed that

$\gamma(N_2O_5)$ was relatively similar at low and high relative humidities (~30-70%) and across four different biomass fuels that had varied BBA chemical compositions. Only one of these fuels produced measurable concentrations of $ClNO_2$. We hypothesized that the solid phase state of chloride in these experiments was limiting $\gamma(N_2O_5)$ and $\phi(ClNO_2)$, and I designed and built a new flow tube system in the CMU Air Quality Lab to conduct similar experiments but above the deliquescence relative humidity of 80% for chloride salts common in BBA. I discovered a 100-300% increase in N_2O_5 reaction probability in high-chloride BBA and no increase in the low-chloride fuels, confirming our hypothesis that the phase of the chloride salts can limit particles' reactions with N_2O_5. Environmental microscopy conducted on high-chloride BBA revealed that the aerosol did not take up water until it was exposed to > 80% relative humidity. These results demonstrate that access to aqueous chloride in the BBA is the main limiting factor to N_2O_5 reactive uptake.

In chapter 4 I presented the chemical composition of aerosol particles I determined at a renowned continental background measurement site – the DOE's Atmospheric Radiation Management Southern Great Plains (SGP) facility. Our data will specifically be used as a part of the Aerosol-Ice Formation Closure Pilot Study to improve and evaluate ice nucleation parameterizations and models. An in-depth analysis of high-resolution aerosol mass spectrometer (AMS) data revealed a predominance of mixed aerosol particles consisting mainly of oxidized organic matter with mass spectral markers specific to the AMS having similar trends to other studies of ambient aerosol as well as some indications of nearby biomass burning. Comparison of this high-resolution data to the facility's low-resolution aerosol chemical speciation monitor showed up to 100% differences in aerosol component concentrations, which is an important consideration for users of this long-term continuous dataset. Analysis from the single-particle laser ablation aerosol time-of-flight mass spectrometer (LAAPTOF) during the same campaign by a group member revealed individual particles that were mostly mineral/organic and

mineral/inorganic mixtures. These data provide further understanding of the aerosol sources, variability, and chemical composition at SGP. This information can then be combined with the DOE's extensive set of full-time aerosol instrumentation and radiation measurements at the facility to achieve a better understanding of the interactions between meteorology, cloud microphysics, and the aerosol radiative effects at this continental background site.

5.2   Future directions

Most existing literature on ice nucleating particles (INPs) in BBA has focused on studying biomass fuels that commonly burn throughout the United States, but fuels native to areas prone to fires such as Australia and the Amazon should be studied as well (Levin et al., 2016; Petters et al., 2009). Here tall grass fuels were found to produce more active ice nucleants compared to wood fuels and this was found to be caused by the enrichment of mineral-forming elements present in these grass fuels. Our work was the first to identify newly-formed minerals as the components within biomass-burning aerosol primarily responsible for ice nucleation, and as others have correlated the ice nucleating activity (INA) of BBA with high combustion efficiency, it would be interesting to revisit their data to see if it can be reinterpreted as mineral formation driving ice activity (Petters et al., 2009). One paper had investigated the effects of atmospheric aging on the INA of a single low INP fuel and found no changes with aging, which is in agreement with our results – the fresh emissions from a combusted fuel must already have INPs that can then be uncovered or concealed in order to change the measured ice activity (Chou et al., 2013). However, our work was the first to extensively study multiple aging regimes for several fuel types that included tall grasses. Thus, further expansion with more instrumentation, such as in a Fire Lab at Missoula Experiments (FLAME) campaign would be beneficial to independently confirm our results. One experimental technique to further probe our results would be to conduct our time aging experiments as usual by collecting filters for INP analysis from the fresh aerosol, from the aerosol that has resided in the chamber for several hours, and then also from aerosol

that is subsequently injected and diluted into a separate chamber to drive additional evaporation and dilution. I expect that this would cause even more ice-active sites to be revealed, resulting in a further increase in the ice-active site density. This would help to determine the maximum possible ice activity in various types of BBA when the ice-active sites are fully available, as might occur following extensive atmospheric transport and dilution. Lastly, the INA of both fresh and aged BBA needs to be incorporated into cloud and climate models to improve their accurate and complete representations of the effects of BBA on cloud microphysics and radiative forcing calculations and predictions. Many models do not even consider ice nucleation as a relevant cloud process due to the complexities and uncertainties in describing mixed-phase cloud microphysics. Those models that do include mixed-phase processes typically do not consider biomass-burning aerosol as a source of INPs, only consider fresh BBA and not the effects of aging, or use fossil fuel combustion soot surrogates rather than measurements from actual biomass-burning aerosol and experiments (DeMott et al., 2010; IPCC, 2014; Ullrich et al., 2019).

We were also the first to study heterogeneous chemistry involving N_2O_5 and $ClNO_2$ in authentic biomass-burning aerosol, so replication of and expansion upon our experimental work is warranted. N_2O_5 reactive uptake and $ClNO_2$ formation were observed to differ even in our two high-chloride fuels that had similar bulk BBA composition, so other fuels should be studied to examine any additional variation and to determine the underlying causes of these differences. The aerosol optical tweezers (AOT) system in the Sullivan group would also be an excellent method for studying N_2O_5 uptake in individual aerosol droplets with different compositions and morphologies. Individual biomass-burning aerosol particles could be trapped in the AOT and exposed to N_2O_5, with the growth of a nitrate ion peak in the Raman spectrum indicative of N_2O_5 uptake kinetics. A chemical ionization mass spectrometer may be able to sample from the AOT chamber as well to measure gas-phase N_2O_5, $ClNO_2$, and HNO_3. The trapped droplet could also be exposed to different vapors and oxidants to create secondary organic aerosol and the droplet's

resulting morphology (e.g. core-shell, partially engulfed, or homogeneously mixed) can be determined by examining the whispering gallery modes in the Raman spectra (Gorkowski et al., 2016, 2020). N_2O_5 uptake on this droplet could be then compared to the unaltered droplet to determine how particle morphology affects uptake. This work has been completed before on bulk aerosol, and we expect that any organic aerosol coatings on the droplet would limit N_2O_5 uptake (Gaston et al., 2014; Ryder et al., 2015). With the AOT, additional information such as the droplet diameter to nanometer accuracy, the droplet pH to two decimal places, and changes in chemical composition from the Raman spectrum could add insight to the governing principles of gaseous uptake into aerosol particles not possible in aerosol ensemble measurement systems like the entrained aerosol flow tube reactors used here (Boyer et al., 2020; Gorkowski et al., 2016, 2020).

Ice nucleation parameterizations are often quite simplified, only taking into account the aerosol size distribution rather than aerosol composition. The mass spectrometry data that determined the aerosol sources, composition, and mixing state of individual particles that the Sullivan Group collected at SGP should be incorporated into ice nucleation models to improve their accuracy and evaluate the major ice nucleating particle parameterizations in use in models. If the inclusion of these data improves such parameterizations or identifies key gaps in our understanding, then additional field campaigns and laboratory experiments could further explore how aerosol composition may predict ice-nucleating activity. We also hope to continue an in-depth analysis of the LAAPTOF and AMS data and work with additional data collected from the various instrumentation at SGP to learn more about various aerosol properties.

5.3   Final remarks

All of the research discussed in this dissertation focused on studying realistic aerosol particles – either ambient aerosol or biomass-burning aerosol created by combusting biomass fuels that commonly are burned in the United States. While studying complex, realistic aerosol systems presents additional experimental challenges, there are fewer underlying assumptions

and extrapolations to be accounted for, which should produce more accurate results. Furthermore, climate change is exacerbating the devastating effects of wildfires, and the increase in the size, frequency, and duration of fires across the globe makes studying their emissions and environmental impacts even more important. Significant atmospheric chemistry research discoveries require the full understanding of complex chemistry and interactions in atmospheric aerosol systems, which is why my work here focused on aerosol chemical composition, the properties of ice nucleating particles, and the kinetics of specific molecules that influence several atmospheric processes. My work has significantly contributed to our fundamental understanding of several realistic aerosol systems, advancing our knowledge of how human activities are altering atmospheric chemistry, air quality, clouds, and the climate.

5.4   References

Boyer, H. C., Gorkowski, K. and Sullivan, R. C.: In Situ pH Measurements of Individual Levitated Microdroplets Using Aerosol Optical Tweezers, , 15, 47, doi:10.1021/acs.analchem.9b04152, 2020.

Chou, C., Kanji, Z. A., Stetzer, O., Tritscher, T., Chirico, R., Heringa, M. F., Weingartner, E., Prévôt, A. S. H., Baltensperger, U. and Lohmann, U.: Effect of photochemical ageing on the ice nucleation properties of diesel and wood burning particles, Atmos. Chem. Phys., 13(2), 761–772, doi:10.5194/acp-13-761-2013, 2013.

DeMott, P. J., Prenni, A. J., Liu, X., Kreidenweis, S. M., Petters, M. D., Twohy, C. H., Richardson, M. S., Eidhammer, T. and Rogers, D. C.: Predicting global atmospheric ice nuclei distributions and their impacts on climate, Proc. Natl. Acad. Sci., 107(25), 11217–11222, doi:10.1073/pnas.0910818107, 2010.

Gaston, C. J., Thornton, J. A. and Ng, N. L.: Reactive uptake of N2O5 to internally mixed inorganic and organic particles: The role of organic carbon oxidation state and inferred organic phase separations, Atmos. Chem. Phys., 14(11), 5693–5707, doi:10.5194/acp-14-5693-2014, 2014.

Gorkowski, K., Beydoun, H., Aboff, M., Walker, J. S., Reid, J. P. and Sullivan, R. C.: Advanced aerosol optical tweezers chamber design to facilitate phase-separation and equilibration timescale experiments on complex droplets, Aerosol Sci. Technol., 50(12), 1327–1341, doi:10.1080/02786826.2016.1224317, 2016.

Gorkowski, K., Donahue, N. M. and Sullivan, R. C.: Aerosol Optical Tweezers Constrain the Morphology Evolution of Liquid-Liquid Phase-Separated Atmospheric Particles, Chem, 6(1), 204–220, doi:10.1016/j.chempr.2019.10.018, 2020.

IPCC: Climate Change 2014: Synthesis Report. Contribution of Working Groups I, II and III to the Fifth Assessment Report of the Intergovernmental Panel on Climate Change, Geneva, Switzerland., 2014.

Levin, E. J. T., McMeeking, G. R., DeMott, P. J., McCluskey, C. S., Carrico, C. M., Nakao, S., Jayarathne, T., Stone, E. A., Stockwell, C. E., Yokelson, R. J. and Kreidenweis, S. M.: Ice-nucleating particle emissions from biomass combustion and the potential importance of soot aerosol, J. Geophys. Res. Atmos., 121(10), 5888–5903, doi:10.1002/2016JD024879, 2016.

Petters, M. D., Parsons, M. T., Prenni, A. J., DeMott, P. J., Kreidenweis, S. M., Carrico, C. M., Sullivan, A. P., McMeeking, G. R., Levin, E. J. T., Wold, C. E., Collett, J. L. and Moosmüller, H.: Ice nuclei emissions from biomass burning, J. Geophys. Res., 114(D7), D07209, doi:10.1029/2008JD011532, 2009.

Ryder, O. S., Campbell, N. R., Morris, H. S., Forestieri, S., Ruppel, M. J., Cappa, C. D., Tivanski, A. V, Prather, K. A. and Bertram, T. H.: On the Role of Organic Coatings in Regulating N2O5 Reactive Uptake to Sea Spray Aerosol, J. Phys. Chem. A, acs.jpca.5b08892, doi:10.1021/acs.jpca.5b08892, 2015.

Ullrich, R., Hoose, C., Cziczo, D. J., Froyd, K. D., Schwarz, J. P., Perring, A. E., Bui, T. V, Schmitt, C. G., Vogel, B., Rieger, D., Leisner, T. and Möhler, O.: Comparison of modeled and measured ice nucleating particle composition in a cirrus cloud, J. Atmos. Sci., 76(4), 1015–1029, doi:10.1175/JAS-D-18-0034.1, 2019.